Karlsruhe Institute of Technology

# Development of a Position-Sensitive Muon Detector with Readout by a Compact SiPM-Array: MIP-Cube

## Entwicklung eines positionssensitiven Myon-Detektors mit Auslesung durch ein kompaktes SiPM-Array: MIP-Cube

Master's Thesis of

Philippe Bruder

At the KIT Faculty of Physics
Institut of Experimental Particle Physics (ETP)
Institut for Astroparticle Physics (IAP)

| | |
|---|---|
| First examiner: | Prof. Dr. Ralph Engel |
| Second examiner: | Prof. Dr. Frank Simon |
| First advisor: | Dr. Andreas Haungs |
| Second advisor: | Dr. Thomas Huber |

02. March 2023 – 01. March 2024

Karlsruher Institut für Technologie
Fakultät für Physik
Wolfgang-Gaede-Str. 1
76131 Karlsruhe

---

I declare that I have developed and written the enclosed thesis completely by myself. I have not used any other than the aids that I have mentioned. I have marked all parts of the thesis that I have included from referenced literature, either in their original wording or paraphrasing their contents. I have followed the by-laws to implement scientific integrity at KIT.

**PLACE, DATE**

. . . . . . . . . . . . . . . . . . . . . . . . . . . . . . . . . . . . . .
(Philippe Bruder)

# Development of a Position-Sensitive Myon Detector with Readout by a Compact SiPM-Array: MIP-Cube

The interaction between cosmic rays and the Earth's atmosphere leads to the formation of extensive air showers, generating high-energy muons that can propagate to the Earth's surface and even into deep, low-noise facilities such as underground research laboratories, where they contribute to the noise level of experiments, for example direct dark matter research. To effectively study systematic background effects, precise measurements of the flux and spatial distribution of these muons is crucial. This thesis introduces a novel monitoring system based on a network of crossed plastic scintillator bars to conduct such measurements. Each bar is 25 cm long and 5 cm wide, read out by a Hamamatsu 64-channel silicon photomultiplier (SiPM) arrays. The employed Fermilab scintillator bars and Kuraray fibers are based on detectors developed for the surface of the IceCube Neutrino Observatory and the AugerPrime scintillator-based surface detector (SSD).

The system features a mobile design that provides adequate power supply and signal processing, with a focus on a plug-and-play setup for variable measurement locations. The DT5202 unit from CAEN Co. Ltd was selected as the Front-End unit for SiPM array readout and trigger electronics. Combined with a specifically developed Python software, this unit functions as a data acquisition system (DAQ), capable of reconstructing the direction of an incoming muon and generating a heatmap of individual pixels. This allows for a detailed analysis of the muon direct distribution and rates.

The results of this work demonstrate that the developed system, "MIP-Cube" is capable of measuring the muon flux and its spatial distribution. This capability opens new avenues for investigating the systematic effects induced by cosmic radiation in sensitive experimental setups. Furthermore, the findings suggest that the system could be adapted for a range of applications, including but not limited to aiding in the calibration of detector systems in particle physics and astrophysics.

Overall, this master's thesis significantly contributes to the development of monitoring systems designed for the precise measurement of high-energy muon fluxes. By combining advanced detector technologies with innovative data acquisition and analysis methods, it provides valuable insights and tools for the research community to better understand and address the challenges associated with cosmic radiation and its impact on scientific experiments.

# Entwicklung eines positionssensitiven Myon-Detektors mit Auslesung durch ein kompaktes SiPM-Array: MIP-Cube

Die Interaktion zwischen kosmischen Strahlen und der Erdatmosphäre führt zur Bildung von ausgedehnten Luftschauern, die hochenergetische Myonen erzeugen, die bis zur Erdoberfläche und sogar in tiefe, geräuscharme Einrichtungen wie unterirdische Forschungslabore vordringen können, wo sie zum Untergrund von Experimenten beitragen. Für die effektive Untersuchung systematischer Hintergrundeinflüsse ist eine präzise Messung des Flusses und der räumlichen Verteilung dieser Myonen entscheidend. Diese Arbeit stellt ein neuartiges Überwachungssystem vor, das auf einem Netzwerk von gekreuzten Plastikszintillator-Stäben basiert, um diese Messungen durchzuführen. Jeder Stab ist 25 cm lang und 5 cm breit, ausgelesen durch ein Hamamatsu 64-Kanal SiPM-Array. Die verwendeten Fermilab-Szintillatorstäbe und Kuraray-Fasern basieren auf Detektoren, die für die Oberfläche des IceCube Neutrino Observatoriums und den AugerPrime szintillatorbasierten Oberflächendetektor (SSD) entwickelt wurden.

Das System zeichnet sich durch ein mobiles Design aus, das eine angemessene Stromversorgung und Signalverarbeitung bietet, mit einem Schwerpunkt auf einem Plug-and-Play-Setup für variable Messorte. Die DT5202-Einheit von CAEN Co. Ltd wurde als Front-End-Einheit für die SiPM-Array-Auslesung und die Trigger-Elektronik ausgewählt. In Kombination mit einer speziell entwickelten Python-Software funktioniert diese Einheit als ein DAQ, das in der Lage ist, die Richtung eines ankommenden Myons zu rekonstruieren und eine Heatmap einzelner Pixel zu erzeugen. Dies ermöglicht eine detaillierte Analyse der Myonenverteilung, was von großer Bedeutung für die Untersuchung von Untergrundereignissen in präzisen physikalischen Experimenten ist.

Die Ergebnisse dieser Arbeit demonstrieren, dass das entwickelte Überwachungssystem in der Lage ist, den Myonenfluss und seine räumliche Verteilung zu messen. Diese Fähigkeit eröffnet neue Wege zur Untersuchung der systematischen Effekte, die durch kosmische Strahlung in empfindlichen experimentellen Aufbauten induziert werden. Darüber hinaus legen die Ergebnisse nahe, dass das System für eine Reihe von Anwendungen angepasst werden könnte, einschließlich, aber nicht beschränkt, auf die Hilfe bei der Kalibrierung von Detektorsystemen in der Teilchenphysik und Astrophysik.

Insgesamt leistet diese Masterarbeit einen signifikanten Beitrag zur Entwicklung von Überwachungssystemen, die für die präzise Messung von hochenergetischen Myonenflüssen konzipiert sind. Durch die Kombination fortschrittlicher Detektortechnologien mit

innovativen Methoden der Datenerfassung und -analyse bietet sie wertvolle Einblicke und Werkzeuge für die Forschungsgemeinschaft, um die Herausforderungen, die mit kosmischer Strahlung und deren Auswirkungen auf wissenschaftliche Experimente verbunden sind, besser zu verstehen und anzugehen.

# Contents

# 1. Introduction

Cosmic[1] rays, the universe's most energetic particles, possess energies exceeding $10^{18}$ eV, dwarfing the highest particle energies of $13.6 \cdot 10^{12}$ eV achieved by the Large Hadron Collider (LHC) post its 2022 upgrade [1]. The origins and acceleration mechanisms of these Ultra-High Energy Cosmic Rays (UHECRs) remain largely enigmatic, yet they offer invaluable insights into the cosmos's most formidable objects, believed to be their extragalactic sources. Furthermore, UHECRs serve as probes into the structure of galactic magnetic fields and facilitate tests of fundamental physics principles, including quantum gravity, special relativity, and the potential for Lorentz invariance violation [2, 3, 4, 5].

Upon interacting with the Earth's atmosphere, UHECRs generate air showers, i.e. a plethora of secondary particles, such as muons and neutrinos. It is the muonic component that underpins Muon Tomography, a nascent yet transformative imaging technique poised to redefine our capability to visualize and analyze otherwise inaccessible structures. Leveraging the natural muon flux, this method offers unprecedented insights into the internal composition of diverse objects, from geological features and archaeological treasures to essential infrastructural elements [6].

Muons also play a pivotal role in low-background experiments, particularly in the realm of direct dark matter detection. Their presence as an irreducible background necessitates their measurement, extending beyond the primary experimental objectives [7]. Integrating direct dark matter research within the framework of Muon Tomography could enhance current muon veto capabilities by providing directional information, which current systems lack. "MIP-Cube" embodies this integration, serving as a proof-of-concept experiment and an educational tool for a broad audience.

The "MIP-Cube", with dimensions of 50 cm x 50 cm x 50 cm, incorporates an internal frame designed to house objects for study, constructed from aluminum profiles secured and connected by 3D-printed components. This frame supports several layers of scintillator bars, arranged to include a coincidence layer and two orthogonal pixel layers for muon detection. The intricacies of connecting scintillators and SiPMs with Kuraray Y11 fibers, considering the fibers' minimum bending radius, necessitate elaborate specific routing solutions. The commercial CAEN CAEN DT5202 device (DT5202) system manages data acquisition with its functionalities and applications further explored within this thesis. Alongside a custom Python program, it facilitates the analysis of muon flux and directional reconstruction in the "SPOCK" laboratory, a controlled, light-proof environment at KIT

---

[1] The language and formulations of this thesis are partly improved with the help of OpenAI's ChatGPT 4. The results of the AI are also cross-checked carefully.

[8]. Each bar connects to a 64-channel SiPM array, with the system's design limited to five cube sides to accommodate the available number of SiPM channels.

The present thesis, however, provides a full functional prototype of "MIP-Cube" ready for further optimisations and first applications in muon-tracking, muon flux determination and in outreach-projects.

# 2. Cosmic rays

At the begin of the twentith century cosmic rays were discoverd by Victor Hess. He made a baloon experiment, where he measured the ionization of the atmosphere. The common opinion was, the radiation and so the ionization decrease with the distance to surface of the earth. He discovered a decrease of the ionization, as expected but at a height above 1000 m the ionization increases. So at a height of 5000 m it reaches earth surface level [9]. Pierre Auger and Bruno Rossi discovered in the 1930's evidences for air showers by observing coincidental cosmic rays in Geiger counters [10][11]. Cosmic ray experiments at sea level with a multiple detector array were first carried out in 1954 by the Rossi Cosmic Ray Group at Massachusetts Institute of Technology (MIT). The group used eleven scintillation detectors deployed by the Harvard College Observatory [12]. The current experiments for high-energy cosmic rays are for example the Pierre Auger Observatory in Argentinia with a detector array area of $3000\,\mathrm{km}^2$ to detect cosmic rays above $10^{17}$ eV [13]. These rays consists of different components up to an energy of $10^{12}$ eV.

## 2.1. Cosmic-ray air showers

The highest energy of charged cosmic rays contain particles up to energies of $10^{20}$ eV. Both the origin and the acceleration mechanism of such particles are currently unknown [15]. Due to the Greisen - Zatsepin - Kuzmin effect (GZK) protons interact with the photons of the cosmic microwave background (CMB) and they build a delta baryon $\Delta^+$ decaying to protons and a pion [16].

$$p + \gamma \longrightarrow \Delta^+ \longrightarrow p + \pi^0, n + \pi^+ \tag{2.1}$$

Table 2.1.: Components of the primary cosmic-ray particles at an ernergy of $10^{12}$ eV [14]

| | |
|---|---|
| Protons | 85 % |
| Helium nuclei | 12 % |
| Nuclei of Z >= 3 | 1-2 % |
| Electrons and positrons | 1-2 % |
| Photons | 0.1 % |

Particles at these high energies can be measured at an average distance of 100 Mpc and are not significantly affected by galactic magnetic fields. This allows a direction reconstruction, which points to the origin of the particle [17]. Such particles are ionized atomic nuclei, thus they interact with the atmosphere of earth. The decay products of this interaction are measurable on the surface of earth with several air-shower experiments. The reconstruction of the direction is possible due conservation of momentum. The decay products maintain the direction of the primery particle, preserving the overall momentum of the system. Such high energetic events are rare, these are detected less than one particle per square kilometer per century, while particles at energy of $10^{15}$ eV appear once per square meter per year [16]. The flux of these particles follow an energy spectrum with a knee at $10^{16}$ eV and an ankle at $10^{18}$ eV [18]. The knee signifies a shift of the accelerationed nuclei from hydrogen to iron. The ankle, on the other hand, denotes the change of the acceleration mechanism from a galaxy internal mechanism to an extra galactic mechanism [16].

The interaction of the cosmic rays with the Earth's atmosphere cause a cascade of particles known as air shower. Air showers comprises three distinct components: hadronic, muonic and electromagnetic. These are illustrated in Figure 2.1. The primary particle undergoes inelastic scattering with air molecules predominantly producing pions, kaons, neutrons, and protons as part of the hadronic component. These particles retain enough energy to induce further inelastic scattering, and cause the other two components. The decay of charged pions is the source of the muons and neutrinos possess a small interaction cross-section, therefore the muonic component has a high penetration depth. The electromagnetic component originates in the decay of neutral pions into photons. Through pair-production, these photons produce electron-positron pairs, which, in turn, produce new photons via bremsstrahlung [19].

To reconstruct the energy of the primary particle $E_0$, the Heitler model is used for the electromagnetic component. This model posits that a particle generates two additional particles while interacting with the atmosphere after traversing the mean free path $\lambda_{em}$. Each new particle carries half the energy of its predecessor.

The number of particles at penetration depth $X$ is expressed as:

$$N(X) = 2^{X/\lambda_{em}}. \tag{2.2}$$

The maximum number of particles occurs when the energy of the particle falls below the critical energy $E_c$, where absorption becomes a higher probability. The maximum number of particles $N_{max}$ is calculated by:

$$N_{max} = \frac{E_0}{E_c} \propto E_0 \tag{2.3}$$

The depth of the shower maximum $X_{max}$ is at

$$X_{max} = \lambda_{em} \cdot \ln \frac{E_0}{E_c} \propto \ln E_0. \tag{2.4}$$

The reconstruction of direction of an air-shower is achievable through the relative arrival time of the air shower at surface detectors in air shower experiments, such as IceTop [20].

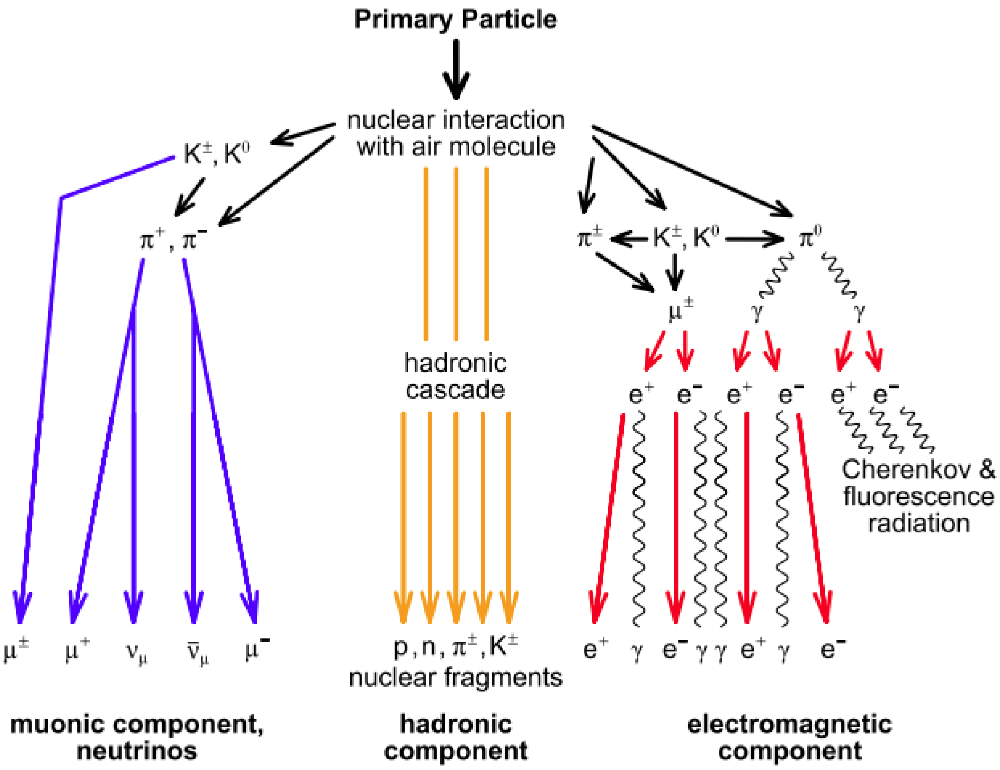

Figure 2.1.: Schematic representation of an air shower segregated into the muonic, hadronic, and electromagnetic components [8].

## 2.2. IceCube Neutrino Oberservatory and IceTop

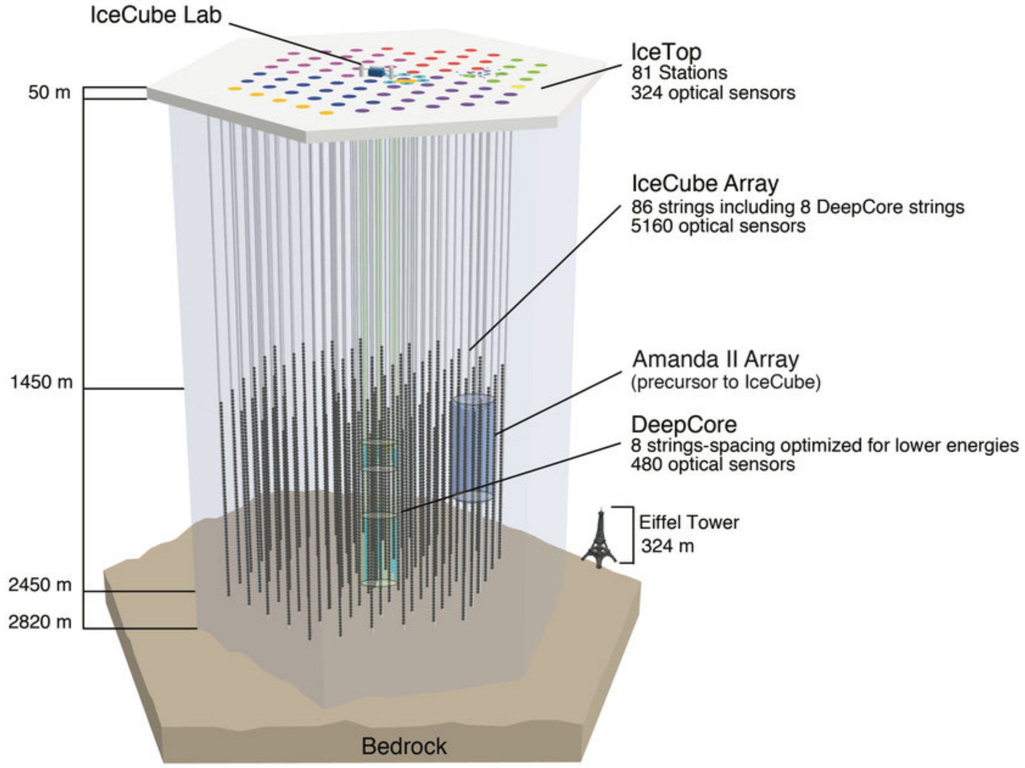

Figure 2.2.: Model view of IceCube with over 5000 digital optical module (DOM) 1450 m under the ice shield surface. Each string contains 60 DOMs. Each string were melted into the ice. On top IceTop is placed. It functions as veto and calibration detector [21].

The IceCube Neutrino Observatory, illustrated in Figure 2.2, is located at the geographic South Pole. Its core detector is embedded within a cubic kilometer of ice, situated 1450 meters beneath the surface of the Antarctic ice sheet. This sophisticated setup is engineered for capturing neutrinos, elusive particles that are key to understanding high-energy cosmic phenomena [22]. Neutrino detection hinges on the interaction via W-boson exchange, leading to the transformation of a neutrino into its corresponding charged lepton (electron, muon, or tau), depending on its flavor. These charged particles, moving faster than light can in ice, emit Cherenkov radiation, detectable in the near ultraviolet spectrum [23]. The distinct patterns of Cherenkov light emitted allow for the differentiation of neutrino flavors. Over 5000 DOM are employed to detect this light, with each string in the ice hosting 60 DOMs, as shown in Figure 2.3 [24].

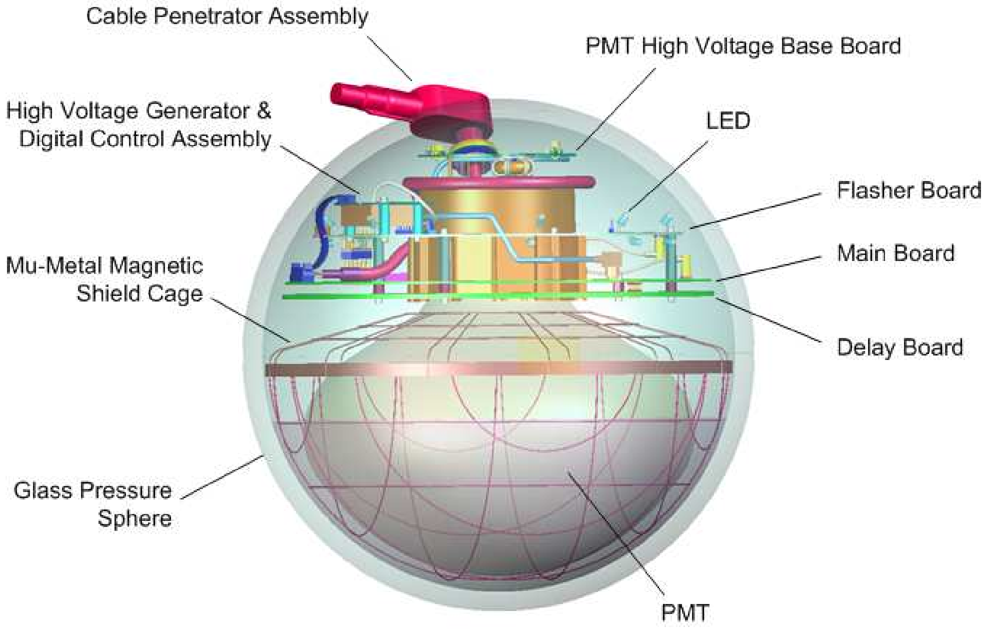

Figure 2.3.: Schematic construction of an IceCube DOM. A glas sphere is choosen to cover a photon multiplier tube (PMT) and its DAQ [18]

### IceTop

For effective neutrino detection, maintaining a low background noise level is crucial. The chosen location minimizes noise from human activities, contributing to the observatory's sensitivity. However, cosmic rays and the resultant atmospheric air showers present a significant source of noise. These air showers produce a considerable flux of muons, detectable by the IceCube Neutrino Observatory. Given the high penetration depth of muons, shielding them is not feasible. Therefore, implementing an active muon veto system is essential. This system accurately measures the muons, enabling their exclusion from the raw IceCube data, thus enhancing the clarity and reliability of neutrino detection efforts [22].

The surface detectors are placed near a string of DOMs. They are ice filled Chrenkov tanks with two DOMs on different gain to increase the dynamic range. IceTop is able to detect air showers from $10^{15}$ eV to $10^{18}$ eV. It is used to calibrate the in-ice detector and to study air showers.

After the upgrade of the surface array in December 2017, it now includes stations with plastic scintillator detectors featuring SiPM-based readouts. The array is structured into stations, and each station is equipped with seven scintillator panels [25]. Scintillators are further elaborated upon in chapter 3.1. One notable advantage of this detector type is its lower charge threshold compared to the ice-filled tanks. This lower threshold allows the panels to reconstruct air showers using fewer detectors and a smaller detection area [26].

## 2.3. Muon Tomography

Muon tomography represents a novel and advanced imaging technique that harnesses the natural flux of cosmic ray muons to generate three-dimensional images of high-density objects and structures. Originating from interactions of cosmic rays with the Earth's atmosphere, muons are highly penetrative elementary particles that can traverse through thick layers of materials, including rock and metal, with significantly less absorption than traditional radiography methods using X-rays or gamma rays [27]. This unique capability makes muon tomography particularly advantageous for applications in geophysical explorations, archaeology, and the inspection of critical infrastructure and nuclear safety [28, 29, 30].

### Principles of Muon Tomography

The fundamental principle of muon tomography lies in the measurement of the attenuation and scattering of muons as they pass through matter. When muons encounter materials of different densities and atomic numbers, they undergo scattering, with the extent of this scattering being contingent upon the material properties. By detecting and analyzing the trajectories of muons before and after passing through an object or structure, it is possible to reconstruct a detailed image of the internal features based on the density distribution. This process leverages sophisticated algorithms and detector technologies to achieve high-resolution imaging [27].

### Techniques and Technologies

Muon tomography utilizes various detector technologies, including scintillators, drift chambers, and gas-filled detectors, to capture the trajectories of muons with high precision. The selection of detector type is influenced by the specific requirements of the application, such as spatial resolution, imaging volume, and operational environment. The data collected from these detectors are processed using computational algorithms that employ techniques like the Point of Closest Approach (PoCA) method and statistical reconstruction methods to infer the density distribution within the scanned volume [27].

### Applications of Muon Tomography

The versatility of muon tomography has facilitated its application across a broad spectrum of fields. In geophysics, it has been employed to image the interior of volcanoes [28]. In the field of archaeology, muon tomography has enabled the non-invasive exploration of ancient structures, such as the Great Pyramid of Giza [29]. Furthermore, its application in the inspection of nuclear reactors and the detection of contraband in cargo containers highlights its potential for enhancing security and safety measures [30].

# 3. Hardware

## 3.1. Scintillator

A scintillator is a material that possesses the ability to emit light flashes, or scintillations, when exposed to ionizing radiation. These light flashes are a result of converting the energy from incoming radiation into visible photons. Scintillators are crucial in detecting and measuring radiation, particularly in high-energy physics and astrophysics [31].

The operation of a scintillator is based on the luminescence process. When an ionizing particle, such as a photon or cosmic ray, enters the scintillator material, it transfers energy to the atoms or molecules of the material. These excited atoms or molecules then return to their ground state by emitting photons of lower energy, typically in the visible spectrum. These photons are then captured by photodetectors such as photomultiplier tubes (PMTs) or avalanche photodiodes, and converted into electrical signals that can be quantified and analyzed [32].

Scintillators are widely used in astro- and particle physics to detect high-energy particles and radiation. Scintillators play also a vital role in detecting and studying cosmic rays. By capturing the light produced when cosmic rays interact with the scintillator material, scientists can analyze the properties and origins of these primary or secondary high-energy particles from outer space [33].

Scintillators are thus an indispensable tool in modern astrophysics. They enable the detection and analysis of radiations and particles that would otherwise be invisible, contributing significantly to our understanding of the universe and its phenomena.

### Plastic Scintillator

Plastic scintillators, known for their versatility and cost-effectiveness, stand as a contrast to crystal scintillators in several key aspects. These scintillators, made from organic polymers, offer significant benefits in terms of manufacturing flexibility. This flexibility allows them to be easily shaped and sized for a variety of applications, a property that is particularly useful in the diverse field of astrophysics [34]. Moreover, their cost-effectiveness is an essential factor, especially when large-area detectors are required, making them a more economical choice compared to the typically more expensive crystal scintillators [31].

In addition to these advantages, plastic scintillators are valued for their robustness. Their mechanical strength makes them less prone to breakage, an important consideration for applications in the harsh environments of space or ground-based observatories [35]. Another notable benefit is their fast response time. Plastic scintillators respond quicker than many crystal scintillators, a critical attribute for resolving events that occur in very short time frames, such as those common in cosmic ray studies [33].

However, these advantages come with certain trade-offs. One of the key disadvantages of plastic scintillators is their lower density compared to crystal scintillators. This lower density can result in reduced efficiency in detecting high-energy photons by conresion into particles before or inside the scintillator or particles [32]. Additionally, plastic scintillators generally offer lower energy resolution than their crystal counterparts. This limitation can be significant in certain types of spectroscopic analysis where precise energy measurement is crucial [31].

Another concern with plastic scintillators is their susceptibility to aging, especially when exposed to radiation from sunlight, e.g. or extreme environmental conditions over long periods. This aging can lead to a decrease in their efficiency and reliability [35].

In conclusion, the choice between plastic and crystal scintillators in astrophysics depends on a careful consideration of these factors. While plastic scintillators offer manufacturing ease, cost savings, robustness, and fast response times, they may fall short in terms of detection efficiency and energy resolution compared to crystal scintillators. Thus, the decision largely hinges on the specific requirements of the astrophysical application or experiment being conducted.

In this project, extruded plastic scintillators from fermilab are utilized. These scintillators possess dimensions of 50 mm x 10 mm and feature a variable length. A detailed depiction of their cross-section is presented in Figure 4.2. Such scintillators are used in astrophysical experiments, including IceTop and the Pierre-Auger-Observatory [20] [13]. A key advantage of the Fermilab scintillators is their cost-effectiveness compared to custom-made alternatives. Their emission wavelength is characteristic and documented in Figure 3.1. The Peak wavelength is observed at $\lambda_{Scint} < 425$ nm. The number of photo-electrons (p.e.) a minimum ionizing particle (MIP) generates is above 40-50 p.e. per em [36].

## 3.2. Silicon Photomultiplier

A SiPM is a sophisticated optical device designed for detecting very low levels of light with exceptional sensitivity and precision. Each SiPM comprises an array of Avalanche Photodiodes (APD), which function in Geiger mode. This mode is significant for triggering an electron multiplication process upon the detection of a photon [37].

SiPMs are distinguished by their silicon substrate, which supports the APDs. These APDs are structured as microcells, each acting as an individual photon detector. This microcell configuration enables SiPMs to detect multiple photons simultaneously, providing high spatial resolution. The cumulative signal from these microcells correlates with the total number of photons detected [37].

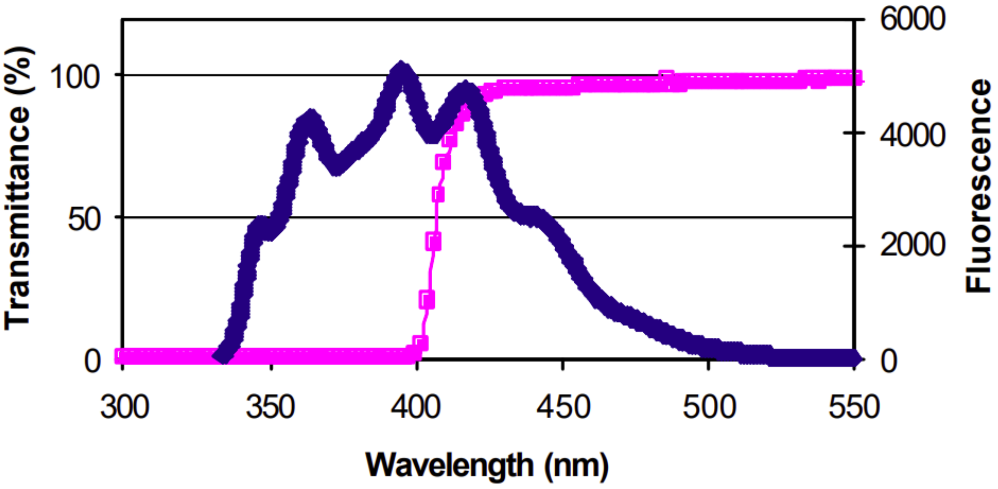

Figure 3.1.: Transmittance (pink) and fluorescence (blue) of an extruded Fermilab Scintillator. The transmittance gives the output wavelength of the scintillator [36].

A notable advantage of SiPMs is their high quantum efficiency. This characteristic, coupled with their ability to operate under low light conditions, makes them suitable for a variety of applications, including biomedicine, astrophysics, and high-energy physics. Compared to traditional PMT, SiPMs are more compact, robust, and immune to magnetic fields. They also require lower operating voltage, enhancing their safety and usability [37].

Furthermore, the advancements in silicon photodetector technology have shifted the preference from vacuum-based PMTs to solid-state silicon photodetectors. This shift is attributed to the cost efficiency of silicon device microfabrication, scalability of wafer processing, and several technological advantages based on the physical properties of silicon photodetectors [37].

Moreover, SiPMs have been established as the device of choice for various applications like time of flight positron emission tomography (TOF-PET), lifetime fluorescence spectroscopy, and high-energy physics due to their sensitivity to single photon detection and fast timing properties [38].

A SiPM has a peak of sensitivity for the Hamamatsu SiPMs at a temperature of $T = 25^\circ$ C is of a wavelength of $\lambda_{SiPM} \approx 450\,\mathrm{nm}$, with an efficiency of 40% [39]. As described in chapter 3.1 the used scintillators transmit light with a peak at a wavelength of $\lambda_{Scint} = 400\,\mathrm{nm}$. The course of the efficiency curve is shown in Figure 3.2. To ensure a maximum efficiency the connection between a scintillator and its SiPM should also shift the wavelength to the SiPM maximum. Therefore the wavelength shifting fibers from Kuraray are used and described in chapter 3.3.

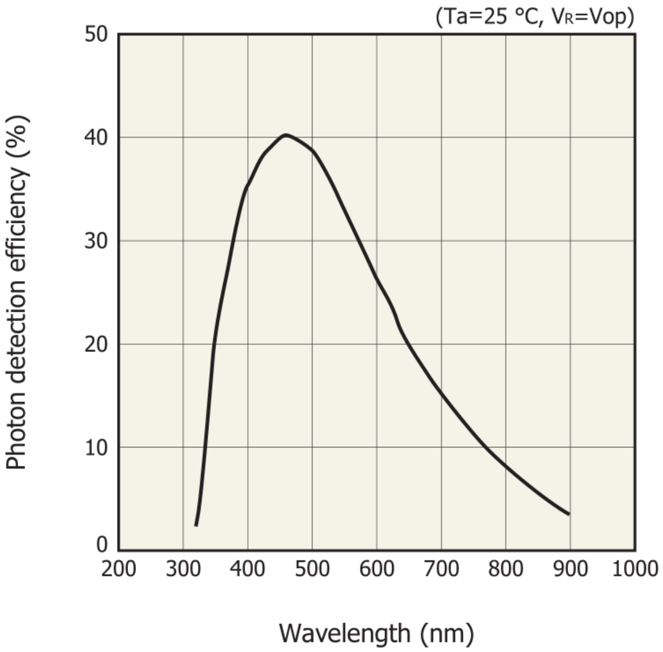

Figure 3.2.: Efficiency curve of a SiPM with the peak efficiency at $\lambda \approx 450\,\mathrm{nm}$ [39].

### Silicon Photomultiplier Array

The SiPM array S13361-3050AE-08 from Hamamatsu Photonics is a state-of-the-art sensor designed for precision measurement applications. This SiPM array is part of the S13361 series and is distinguished by its reduced crosstalk and dark count, and low afterpulse characteristics, which enhance its measurement accuracy and reliability [40, 39].

The S13361-3050AE-08 array is configured as an 8x8 channel grid, comprising 64 channels in total. Each channel's effective photosensitive area measures 3 x 3 mm, and it contains 3584 pixels, each 50 µm in size. This high pixel density allows for detailed and high-resolution photon detection. The array covers a spectral response range from 320 to 900 nm, with peak sensitivity around 450 nm, suitable for a wide range of photonic applications [40].

A notable feature of this SiPM array is the use of through-silicon via technology. This advancement reduces non-sensitive areas around the photosensitive regions, thereby optimizing the sensor's overall efficiency and detection capabilities. The 4-side buttable structure of the array allows for close packing of multiple elements, facilitating the creation of larger, scalable sensor arrays for complex photonic detection systems [39].

The device reports a typical dark count rate of 500 kcps per channel and a terminal capacitance of 320 pF per channel, with a typical gain of about $1.7 \cdot 10^6$. These specifications indicate the array's sensitivity and effectiveness in low-light conditions. It operates at a recommended voltage of 56 V at an ambient temperature of 25 °C, ensuring stable performance across a range of environmental conditions [40].

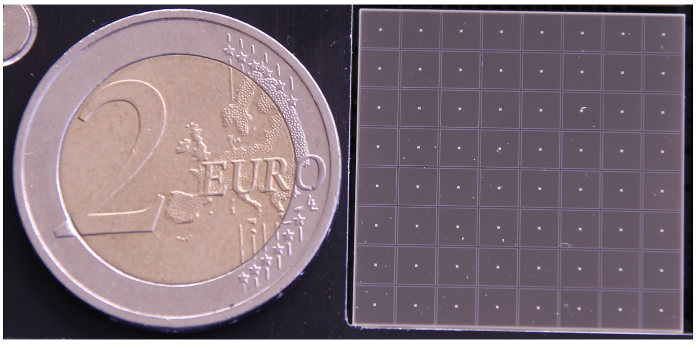

Figure 3.3.: Detailed view of an 8x8 SiPM array juxtaposed with a 2 Euro coin for scale

The Hamamatsu S13361-3050AE-08 is instrumental in various advanced fields like medical imaging, high-energy physics, and photonics research. Its precision measurement capabilities, coupled with technological advancements such as reduced crosstalk, low afterpulse, and TSV technology, make it a prime choice for applications requiring high sensitivity and accuracy. The array's design also supports integration into larger, more complex photonic detection and imaging systems [40, 39].

## 3.3. Optical Fiber

The used optical fibers have wavelength shifting characteristics so they are called Wavelength shifting (WLS) fiber. They are crucial in astrophysical research and particle physics for their ability to adapt the wavelength of light to the optimal detection range of photo detectors like PMTs or SiPMs.

The primary use of WLS fibers is to shift the wavelength of light emitted from a scintillator to a range where PMTs or SiPMs are more efficient. Scintillators often emit light in the ultraviolet spectrum, which is not efficiently detected by these photo detectors. WLS fibers absorb this ultraviolet light and re-emit it at a longer wavelength, typically in the visible spectrum, where PMTs and SiPMs have higher sensitivity and efficiency.

WLS fibers contain a dopant that absorbs photons at one wavelength and re-emits them at a longer wavelength. This conversion is key in applications requiring the detection of specific wavelengths that are otherwise challenging due to the limitations of detector sensitivity.

The performance of WLS fibers is influenced by their composition, conversion efficiency, and the spectral overlap between the fiber's emission and the photo detector's sensitivity. Proper integration with photo detectors is crucial for maximizing the efficiency and accuracy of the detection system.

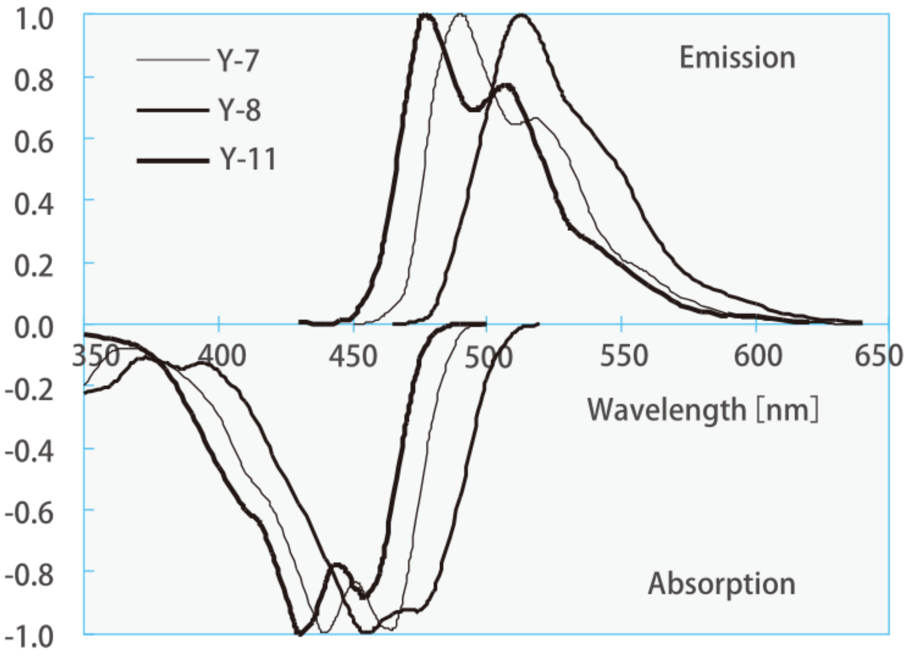

Figure 3.4.: Absorption and emission curve for the Kuraray Y-7, Y-8 and Y-11 fiber. Ensure a wavelength shift from a wavelength of 430 nm to 476 nm [41].

### Kuraray Fiber Y-11

The chosen fiber is the Y-11 from Kuraray. As in Figure 3.4 shown, the wavelength shifting characteristic fits to the emission of the chosen scintillator (Figure 3.1) and efficiency curve of the SiPM-Array in Figure 3.2 [41].

The fiber in question exhibits supplementary properties that necessitate careful consideration in the design phase. Despite incorporating a double sheathing to minimize light loss, the Y-11 fiber with a thickness of 1 mm maintains a minimal bending radius of $r_{min} = 10$ cm. This constraint imposes additional spatial requirements for the fiber's accommodation [41].

An additional critical parameter is the fiber's length. To effectively shift the wavelength towards the efficiency peak of the SiPM, a minimum length of $l > 50$ cm from the end of the scintillator to the SiPM is essential. While it is feasible to employ a shorter fiber, this would result in a compromise regarding the SiPM's efficiency, because of the reduced sensitivity of a SiPM to blue light [41].

The Y-11 also have scintillating characteristics [41]. Therefore a passing particle through the fiber generates a signal, which can be interpreted as a scintillator signal. In the later "MIP-Cube" device the spatial resolution is important, so an additional signal could give less accurate data. For this reason a lead shielding for the main part of the routing could be necessary.

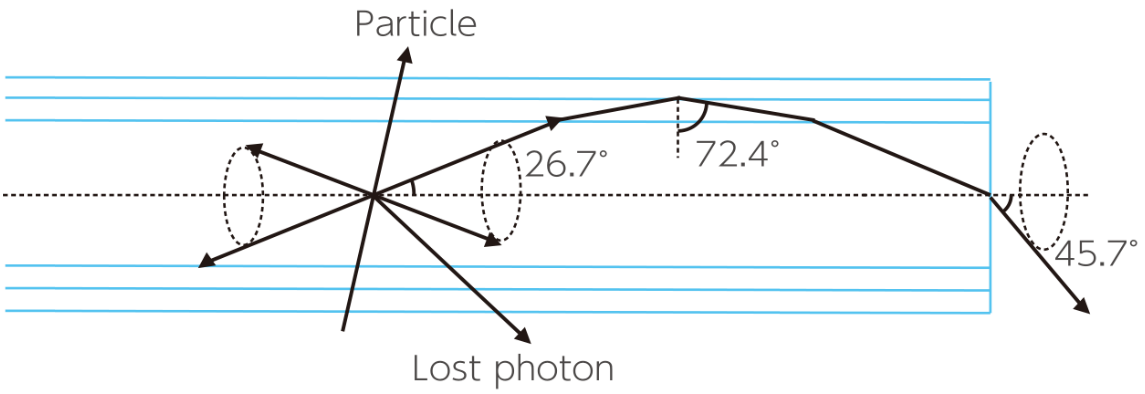

Figure 3.5.: Double sheathing of the Y-11 fiber to ensure less loss of light [41].

(a)

(b)

Figure 3.6.: Left: Picture of the DT5202 device from CAEN [42]. Right: Adapter for a Hamamatsu 8x8 SiPM-array [43].

## 3.4. CAEN DT5202

The DT5202 module, an advanced multi-channel readout system optimized for SiPM readout, plays a pivotal role in various high-tech and scientific fields. Its versatility and precision make it a key component in environments where accurate data acquisition is critical.

In high-energy physics, the DT5202 is used in particle detection and analysis. Its ability to manage up to 64 data channels simultaneously is invaluable in experiments involving multiple detectors.

In the realm of medical imaging, examplifies in Positron Emission Tomography (PET), the DT5202's precision in signal detection and processing is vital. PET scans require accurate detection of gamma rays emitted by radiotracers in the human body. The module's sensitivity and accuracy in signal processing lead to clear, detailed images, crucial for precise diagnoses [44].

Furthermore, the DT5202 finds extensive use in various research and development sectors, where its reliability and precision are of paramount importance. In fields like material science, nuclear physics, and astro-particle physics, it facilitates cutting-edge research by enabling accurate and reliable data collection. Its robust design and flexibility in handling different types of detectors make it a versatile tool for various experimental setups.

Additionally, the setup includes an adapter board designed for the Hamamatsu 8x8 SiPM-array, a component also offered in CAEN's product lineup. This adapter, showcased in Figure 3.6b, is engineered to attach directly to the electrical connections of the DT5202. It facilitates a mechanical conversion from the input edge card connector to Samtec connectors, ensuring compatibility and ease of integration. Moreover, the adapter is outfitted with a TMP37 temperature sensor, providing critical temperature monitoring capabilities [43].

Overall, the DT5202 module stands out as a critical component in several scientific and technological domains. Its advanced features and capabilities enable it to meet the demands of diverse applications, ranging from fundamental physics research to critical environmental monitoring. Additionally, with the capability of the *Janus*-Software up to eight DT5202 devices, it is possible enlarge experiments, which work with this device [45].

One challenge with the DT5202 involves the SiPMs heating up to approximately 33°C, which results in a lower noise to signal ratio in SiPMs. Therefore, a cooling system is recommended by CAEN, for the use of this device in closed environments.

### Technical Details

The DT5202 module, a cornerstone in advanced detector technology, exemplifies a blend of cutting-edge engineering and functional versatility. At its core lies the Field Programmable Gate Array (FPGA), a customizable processor that adapts to various data acquisition needs.

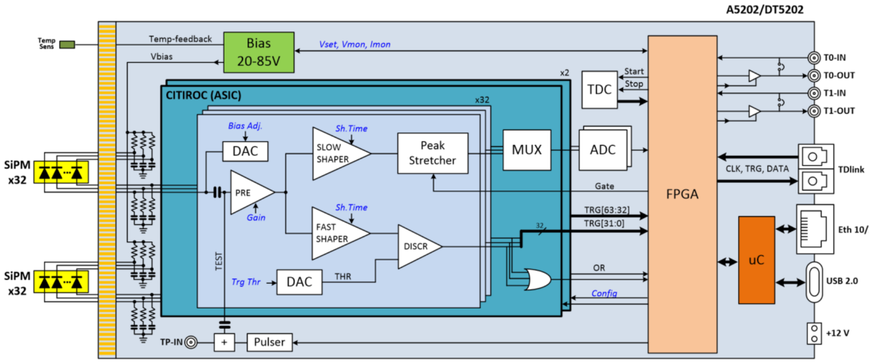

Figure 3.7.: Block diagram of the DT5202 [45].

This FPGA is the linchpin for the module's data processing capabilities, enabling it to manage and process inputs from a 64 channel array of detectors efficiently [45].

Two Citiroc processors are needed to manage the 64 SiPMs It is a crucial component of the DT5202's architecture. This preamplifier and discriminator Application-Specific Integrated Circuit (ASIC) is specifically designed for SiPM readout, offering optimized performance for these detectors. The Citiroc enables precise photon counting and timing, making it ideal for applications requiring high accuracy and sensitivity. Integrating the Citiroc with the DT5202's FPGA as pictured in Figure 3.7. It communicates with other components as an Analog to Digital Converter (ADC) enhances the module's capability to handle complex data acquisition tasks, especially in high-precision environments like particle physics and medical imaging [45].

Another characteristic are the two different gains the module can save. There is the Low Gain (LG) and the High Gain (HG) which can be set individually, while HG is ten times the gain of the LG. Also a trigger threshold can be set in natural numbers from zero to a maximum of 1024 [45].

Surrounding this central processors are multiple input and output channels, facilitating the module's communication with external devices. These channels are designed to handle data rates of up to 100 kHz, ensuring swift and accurate data transfer, which is essential in high-speed data acquisition scenarios like particle physics experiments [45].

The module's operational modes, including spectroscopy, counting, and timing, leverage the FPGA's adaptability. In spectroscopy mode, making it invaluable in fields like nuclear physics. The counting mode is crucial for applications that require precise event quantification, such as environmental monitoring. Meanwhile, the timing mode's precision makes it indispensable for experiments demanding high temporal resolution [45].

Moreover, the DT5202's interface and connectivity options underscore its role in modern scientific setups. It is able to connect to the user interface *Janus*. The interface allows to change the mode, gives a fist imaging of the data and several important settings can be done. The same functions also available over a shell. The DT5202 is connectable with Linux and Windows [46].

## Modi

In each mode, the module reads data after a predefined interval. This interval, termed the "Periodic Trigger Period" in *Janus* terminology, varies between 16 ns and 32 s. It determines when the built-in multiplexer retrieves data from the ADC [46]. Each mode saves its data in a distinct format. The data can be saved either as a text file or as a binary file. The text file is human-readable, whereas the binary file requires decoding using the instructions provided in the *Janus* manual.

In spectroscopy mode, the DT5202 is capable of performing spectrum analysis. It records peak heights in up to 8000 ADC channels but usual 4000 are used, saving these values at predetermined intervals for each of the 64 channels [46]. This mode generates substantial data traffic. For instance, a five-minute measurement with a trigger period of 500 $\mu$s across all 64 channels can result in a file size of approximately 2 GB.

The counting mode of the DT5202 module compiles a list indicating how many signals exceed the preset threshold for each channel [46].

In timing mode, the module captures additional information. When a signal exceeding the threshold is detected by a sensor, both the Time of Arrival (ToA) and Time over Threshold (ToT) for the active sensor are recorded [46]. This mode generates less data traffic. For example, a five-minute measurement with a trigger period of 500 $\mu$s and 55 active sensors out of 64 can produce a file size of about 2 MB.

## Settings

The readout software *Janus* gives several different setting options. In this chapter the ones with most influence in the framework of the measurements at this thesis are described. Each of the following setting can be set for each sensor channel individually.

### High Voltage

The High Voltage (HV) allows for varying the applied voltage at a SiPM, which is the primary adjustable parameter. This voltage should correspond to the bias voltage of the specific SiPM. In this case, the bias voltage is approximately $V_{bias} = 55 - 60$ V. This value directly influences the maximum current strength. The maximum current strength can also be configured in *Janus*. If the actual current strength exceeds the predefined maximum, the DT5202 will shut down [45].

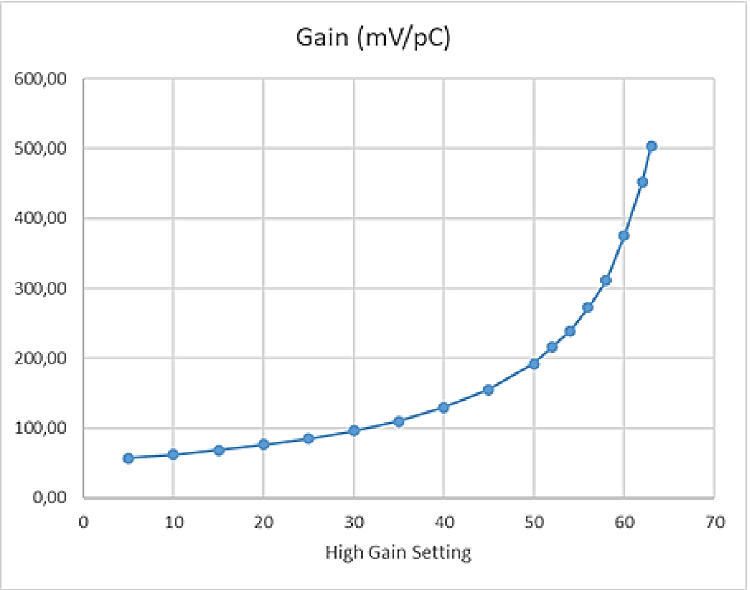

Figure 3.8.: Diagram illustrating the relationship between the set gain value and the current gain, as referenced in [45].

### Gain

The device features two distinct types of gain: the HG and the LG. Each can be independently set with a value ranging from 0 to 63. As illustrated in Figure 3.8, these integer values correspond to specific current gains. The primary difference between HG and LG is a gain factor of ten [45].

### Threshold

Varying the threshold is an important tool. This adjustment can significantly increase or decrease the counting rate of triggers. The threshold can be set to any natural number. At lower values, a higher number of counts, often caused by noise, is recorded in the data file. Conversely, at higher values, particularly in a cosmic ray experiment scenario, only a multiple of high-energy particles can generate a light pulse intense enough to surpass a high threshold. Consequently, only these particles are measured. The set value can be independently adjusted for each of the 64 channels. Before conducting the first measurement, a threshold scan should be performed with no active detector material or another light source connected. Subsequently, the gain for each channel should be adjusted so that the counts per second for all channels fall to zero at the same threshold value as pictured in Figure 3.9 for one channel.

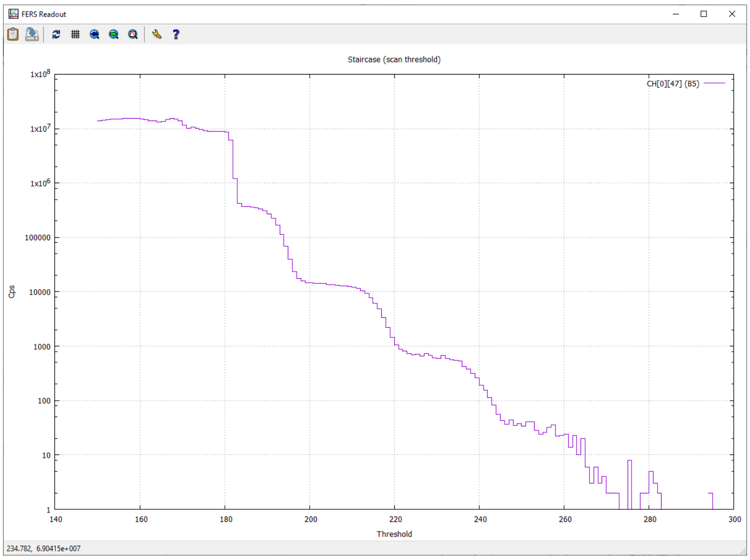

Figure 3.9.: Threshold Scan for a Single Channel: The diagram illustrates a threshold scan for a single channel, with “cps” indicating the measurement unit of counts per second, representing the event detection rate. While the “Threshold” is in units of a 10-Bit ADC. The diagram is taken directly out of the manual [45].

### Time Reference

Another general setting option is the time interval between two readout processes. This interval can be adjusted from 16 ns to 32 s. The optimal duration depends on the dead time of the connected sensor and the minimal readout time of the internal multiplexer, which is 200 ns for all 64 channels. In *Janus*, this setting is referred to as ”time referenced“.

# 4. Hardware Conception

The main goals of this master thesis are to design a device capable of measuring the incoming muon rate as well as reconstructing the individual muon directions. To achieve this, a three-dimensional structure is required. A straightforward solution is a device shaped like a cube. Each side of this cube should be equipped to measure incoming muons, providing information about the passing rate. For directional reconstruction, a timestamp for arriving muons is essential. To enhance accuracy, it is optimal not only to determine which sides the muon passed through but also to have spatial resolution for each side. Additionally, there should be a cavity between the sides to place an object inside. This allows for later analysis to determine how many muons passed through the object, and by this to get some density information of the object.

To build such a device several components are required. To measure the muon at first place scintillators are used. From each scintillator an optical fiber leads to an array of 64 SiPMs. The array is mounted to the DT5202 as DAQ, using an adapter also from CAEN. This device stores the data which can be retrieved by the CAEN software *Janus*. It provides an event list with timestamps and triggered SiPM-Number. A more detailed hardware description is available in chapter 3. The event list can processed by an Python script, which generates a heatmap of each side of the cube and reconstructs the azimuth and altitude angles of arriving muons or, more general, MIP. A flow chart of this process is shown in Figure 4.1.

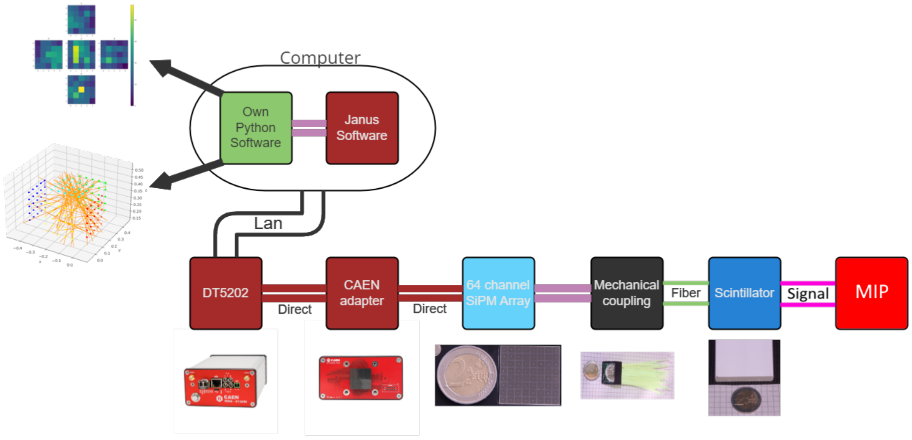

Figure 4.1.: Flowchart of the process from measure an arriving muon at the sintillators (right part) to generate a heat map an directional reconstruction.

## 4.1. Scintillator Configuration

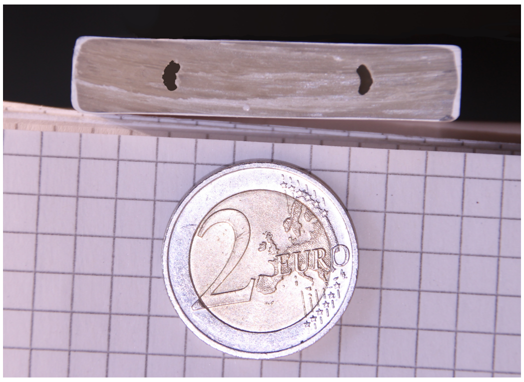

Figure 4.2.: Cross-section of a Fermilab scintillator, in comparison to a 2-Euro-piece, has dimensions of 50 mm x 10 mm and variable length. Also shown the two holes intended for two optical fibers to connect to a SiPM [36]

Multiple Fermilab plastic scintillator bars are utilized for the muon detection. Each bar has a dimension of 50 mm x 10 mm and a variable length. Two holes are intended for optical fibers to connect the scintillator with a SiPM, as shown in fig 4.2. To garantee a spatial resolution on each side, the chosen solution for this thesis involves arranging two layers, one horizontal layer and one vertical layer. This configuration gives a grid of "scintillator pixels". With the width of one bar of 50 mm it gives the width and length of the grid as a multiple of 50 mm. A decision has been made to include an additional layer, the "coincidence layer". In this initial concept, the coincidence layer aids to independently calibrate each side. This layer covers the length and width of the scintillator pixel area, consisting of multiple Fermilab bars. This first concept has some limiting factors. One limit is the use of Hamamatsu 64-channel-SiPM-array [39]. Therefore, the maximal number of scintillators can be placed on the cube is 64. Each scintillator in each layer is connected to one SiPM of the SiPM-Array. Except the scintillators in one coincidence layer, all scintillators of one coincidence layer on one side of the cube are connected to one SiPM. The number of scintillators on one side $n_{max}$, the number of scintillators per pixel layer $n$ is given by:

$$n_{max} = 2 \cdot n + 1. \tag{4.1}$$

Considering six sides and the limit of 64 SiPMs, this results in four scintillator bars per side, with 9 SiPMs not being used. Also it makes a surface area of only 200 mm x 200 mm. Both factors led to the decision not place scintillators at the bottom of the cube. This results in several advantages including having five scintillators per side and one less unused SiPM. Additionally, the absence of scintillators at the bottom gives the cube a more stable stand. At a later stage of the "MIP-Cube" project, it is possible to eliminate the coincidence layers and put the scintillators at the bottom to get a detector with a six-sided configuration.

## 4.2. Frame

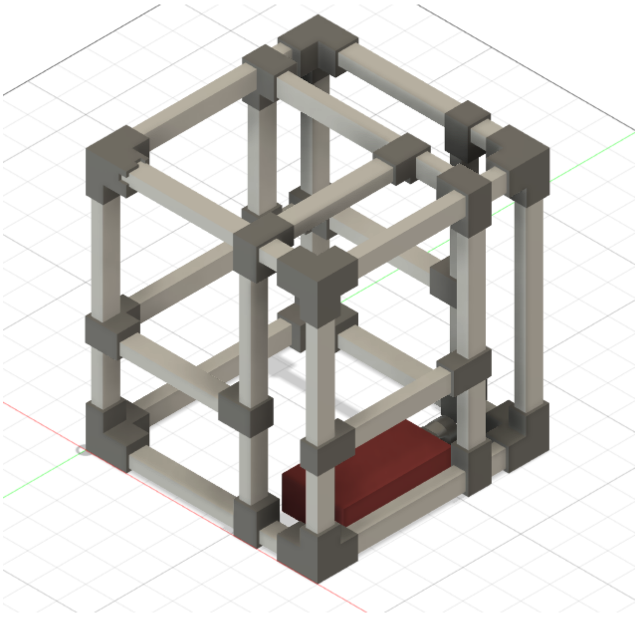

Figure 4.3.: Isometric view of the frame of the "MIP-Cube" device model without scintillators, their holder, optical fibers and their routing. At each corner a 3D print model is placed (black). The silver bars connecting the 3D prints represent aluminum profiles. At the bottom, a model of DT5202 is shown.

To ensure the stability of a device with a cavity, a frame is essential. The frame must be larger than the scintillator-covered area to accommodate the minimal bending diameter of 10 cm of the optical fibers. The main structure is constructed from aluminum profiles with a rectangular cross-section, measuring 20 mm x 30 mm and featuring a material thickness of 2 mm. There are 21 different tiles with different attached screws for the sccintillators or their holders. All their construction draws are illustrated in the appendix in the Figures A.6 to A.11. The appendix contains detailed construction drawings for the 21 distinct profiles, each with varying screws attached for securing the scintillators or their holders. These drawings are systematically illustrated across Figures A.6 through to A.11.

For the eight corners and the connectors of the cross brace, 3D-printed parts are employed. An example is shown in the appendix in Figure A.1. Due to symmetry considerations, there are two different corner models. Additionaly, there are deviations among the corners, as the scintillators are placed in a confined place. Therefore, the holders for the scintillators at some points are placed where the 3D-print parts would be, leading to some corners being shortened. While assembling the frame, it is essential to maintain an overview; therefore, the letters *A* to *G* are printed into each corner. The round holes in the 3D-model are designed for roll pins with a diameter of 5 mm to stable the frame construction. An isometric view on the 3D model of entire frame is represented in Figure 4.3.

The isometric view of the cube in Figure 4.4 provides a comprehensive overview of its various components. In the 3D model shown in Figure 4.4b, the connectors (depicted in black) are highlighted, demonstrating their role in securing the aluminum profiles. This arrangement ensures the precise positioning of the scintillator layers, which are represented in beige, yellow, and purple. Additionally, the holders, shown in blue and light gray, are indicated in their specific locations. The path for wiring or optical fibers is also illustrated in gray for clarity.

In the actual cube, as seen in Figure 4.4a, the authentic colors of the different components are discernible. This image reveals the optical fibers in a vibrant green, providing a contrast that highlights their placement and routing within the cube's structure. This visual representation aids in understanding the cube's intricate design and the functional integration of its parts, emphasizing the careful consideration given to the assembly and arrangement for optimal performance.

The 15 different connectors are depicted in the appendix in the Figures A.3, A.4 and A.5. They reduce the area of the cube's surface to hold the scintillators and ensure there is enough space for the optical fibers and their minimal bending diameter of $d_{min} = 10\,\mathrm{cm}$. Similar to the corners, the connectors are also marked with the letters $A$ to $O$.

The necessity for a high variety of different profiles and 3D-printed components arises from the profiles' non-square, rectangular cross-sectional shape. This geometric characteristic of the profiles dictates the need for customized fittings and connectors to accommodate the unique dimensions and ensure a secure, precise assembly. The rectangular cross-section, while offering structural advantages, introduces complexity in design and assembly, requiring a broader array of specialized parts to achieve the desired fit and stability within the system.

The holders are printed in two parts and they are designed to hold all three layers of scintillators in horizontal and vertical direction. An image is shown in the appendix in Figure A.2. The 3D prints are connected with the aluminum frame with screws of a diameter of 5 mm. The screws fit in placed threaded bushings, which are pressed in predrilled holes.

The aluminum profiles are equipped with predrilled holes for mounting the scintillator holders. Owing to this feature, along with the variety in lengths, there are 18 distinct profiles. The vertical profiles are 50 cm taller than the horizontal ones to accommodate storage space at the bottom for the required length of Kuraray fiber. Additionally, a lead layer can be positioned over the fiber storage area to attenuate the scintillation properties of the fibers.

Figure 4.5 presents the front view of the "MIP-Cube", with Side $A$ facing the viewer and no visible routing for the optical fibers, with the same color code as Figure 4.4b. An illustration that delineates which side of the cube corresponds to each letter is depicted in Figure 4.16b. This visual aid provides a clear reference for understanding the spatial orientation and labeling convention used throughout the "MIP-Cube" project, facilitating a more intuitive grasp of the cube's design and the specific locations of its components. In this perspective, it is noticeable that the scintillators do not cover the entire side, leaving gaps. These gaps are strategically designed to accommodate the routing of the fibers, which require a minimum bending diameter of 10 cm to avoid damage and maintain signal integrity.

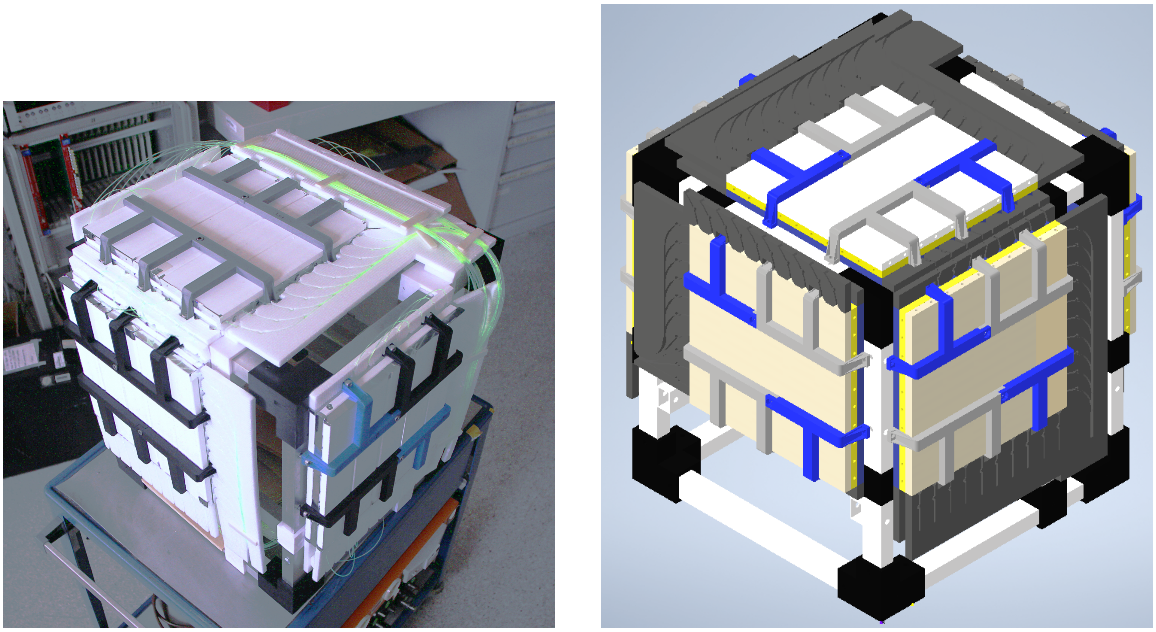

(a) (b)

Figure 4.4.: Figure 4.4a - A picture of the built up “MIP-Cube” without installed lead shield. The scintillator holders, scintillators, routings and fibers are mounted. Figure 4.4b - A 3D model of the frame with mounted scintillators, scintillator holders and the routing for the optical fibers.

Consequently, two fibers are led from each scintillator to a single SiPM, necessitating a gap on one side of the scintillators for this purpose.

Additionally, space at the bottom of the cube is allocated for the storage of fibers, ensuring they have equal lengths, which is crucial for consistent signal transmission across all channels. This requirement for space around the scintillators introduces several gaps on all sides of the cube, affecting its ability to detect particles from certain angles. Specifically, the detection of particles moving from side *E* to sides *B* and *C* is less efficient compared to those moving to sides *A* and *D*. This discrepancy is attributed to the expected steep trajectory of muons and the larger gaps between sides *B*, *C*, and *E*, which can hinder the cube’s detection capabilities in these directions.

Figure 4.6 presents a view of Side *D*, facing the viewer, with the routing components yet to be installed. The color coding remains consistent with that established in Figure 4.4b. In this depiction, the aluminum profiles (orange), reserved for a potential lead shielding, are visible, showing their cross-sectional faces. There is a notable overlap with the routing designed for the coincidence layer, indicating that when placing the lead shield, care must be taken to avoid damaging the optical fibers. This detail underscores the importance of precision in assembling the shielding components to ensure the integrity of the fiber routing while enhancing the cube’s ability to shield against unwanted interference.

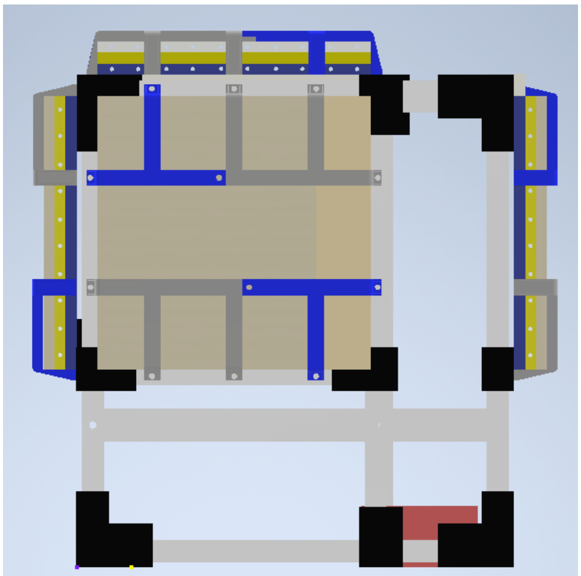

Figure 4.5.: Front view on the cube with mounted scintillators and their holders, without the routing for the fibers. In the right bottom corner the red box represents the DT5202.

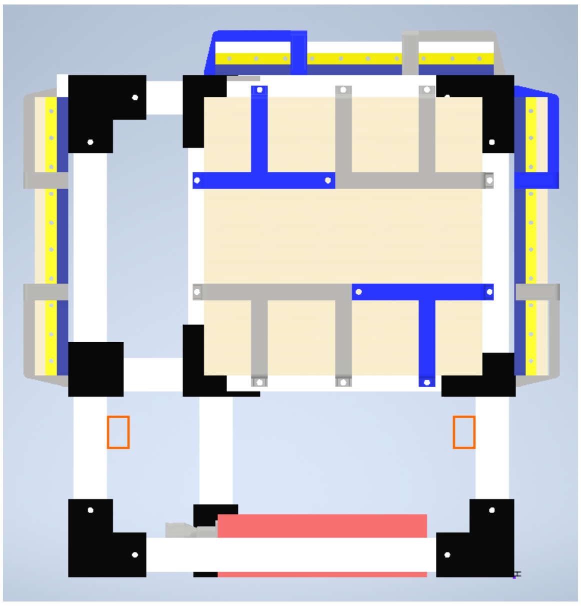

Figure 4.6.: Side view on the cube with mounted scintillators and their holders, without the routing for the fibers. At red box at the bottom represents the DT5202. Also viewable are the cross-sections of the aluminium profiles (orange), which are reserved as lead shield holder

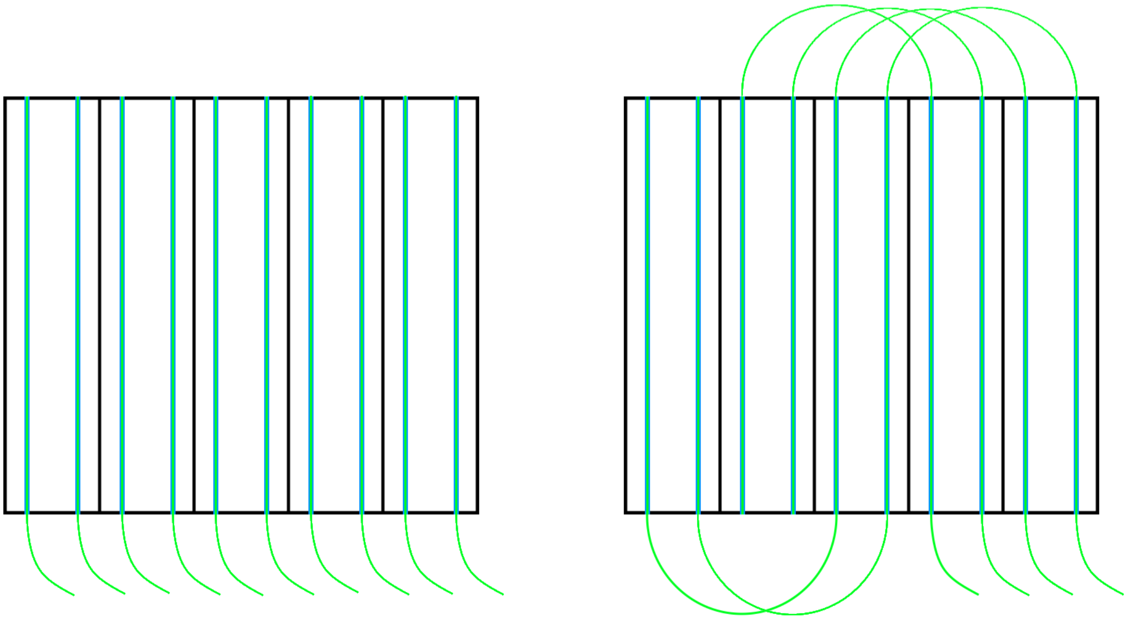

Figure 4.7.: On the left side are Fermilab's scintillator bars, embedded with Kuraray fibers for the position sensitive pixel layers. These fibers have one open end, which is covered with aluminum tape to minimize light loss. Each scintillator is paired with two fibers. On the right are the bars embedded with fibers for the coincidence layers. The open end of these fibers is also covered with aluminum. Two fibers connect three bars, while two different fibers connect two bars.

## 4.3. Connection Scintillator-Fiber

To enhance the detection of MIP, optimizing the light yield is crucial. Minimizing light loss is, therefore, a key objective. This is achieved by designing scintillator bars with continuous holes specifically for accommodating optical fibers, thereby maximizing light collection. A fiber looped through one or more bars ensures maximal light capture. However, to preserve the integrity of the information regarding the specific bar being targeted, connecting multiple scintillators directly is not feasible. Furthermore, to maintain a minimal bending diameter of 10 cm, incorporating a single loop for each bar would necessitate an additional 10 cm on each side of the cube, rendering this approach impractical. As a solution for the "MIP-Cube", two fibers with open ends are laid within the scintillator, and these ends are covered with aluminum foil to reflect the escaping light back into the system. Two fibers are responsible for one scintillator, therefore each pair of fiber is connected to a single SiPM. This configuration applies to the 2 x 5 pixel layers.

In the coincidence layer, all five scintillator bars are connected to a single SiPM. The scintillators are placed adjacent to each other. Due to the minimal bending diameter of the fibers, connecting all five scintillators directly is not practical. Therefore, three scintillators are connected to a single SiPM using two fibers, and the remaining two scintillators are connected to the same SiPM. This configuration is illustrated in Figure 4.7.

## 4.4. Precision Fiber-SiPM Coupling

Figure 4.8.: Array mask with fibers securely glued into place. Noticeable are the illuminated fibers, in contrast to the eight non-illuminated fibers along the diagonal and the single non-illuminated fiber in the bottom left corner, as detailed in. With the blank fibers in background.

One task involves connecting the optical fibers to the SiPM array. The coupling mechanism should prevent photons from traveling from the end of one fiber to an adjacent SiPM. To achieve this, each fiber must be carefully guided and securely pressed against the SiPM. Typically, the fibers are glued to the SiPMs; however, this method permanently attaches the SiPM to the fiber, rendering the SiPM unusable for future projects. Therefore, optical cement cannot be employed directly for the initial prototype. Instead, a system of frames designed to hold the fibers in place without adhesive has been developed and is 3D printed, as shown in Figure 4.14.

The 3D printed bracket showcased in Figure 4.9 plays a pivotal role in stabilizing the assembly of 130 optical fibers and the entire coupling system on the DT5202, utilizing screws for secure attachment. The corresponding attachment points can be observed at the CAEN adapter, as depicted in Figure 3.6b. Moreover, this bracket design facilitates the addition of a light-proof cover or hose, which can be snugly fitted over the bracket's upper cylindrical portion to enhance light isolation. A specially designed groove in the cylindrical section allows for the secure fastening of a light-proof cover using either a clamp or cable ties, ensuring optimal darkness within the system. The bracket transitions from a cylindrical to a squared section, accommodating the rest of the coupling system components. Notably, at the juncture of these two sections, a slight overhang prevents any upward movement of the coupled parts, further ensuring the system's stability and integrity.

The supplementary components for the "MIP-Cube" are fabricated utilizing Stereolithography (SLA) 3D printing technology to ensure high precision, achieving tolerances of 0.01 mm on the z-axis and 0.0285 mm on the x- and y-axes. At the heart of the coupling system lies the array mask (Figure 4.10), designed to accurately position the optical fibers with

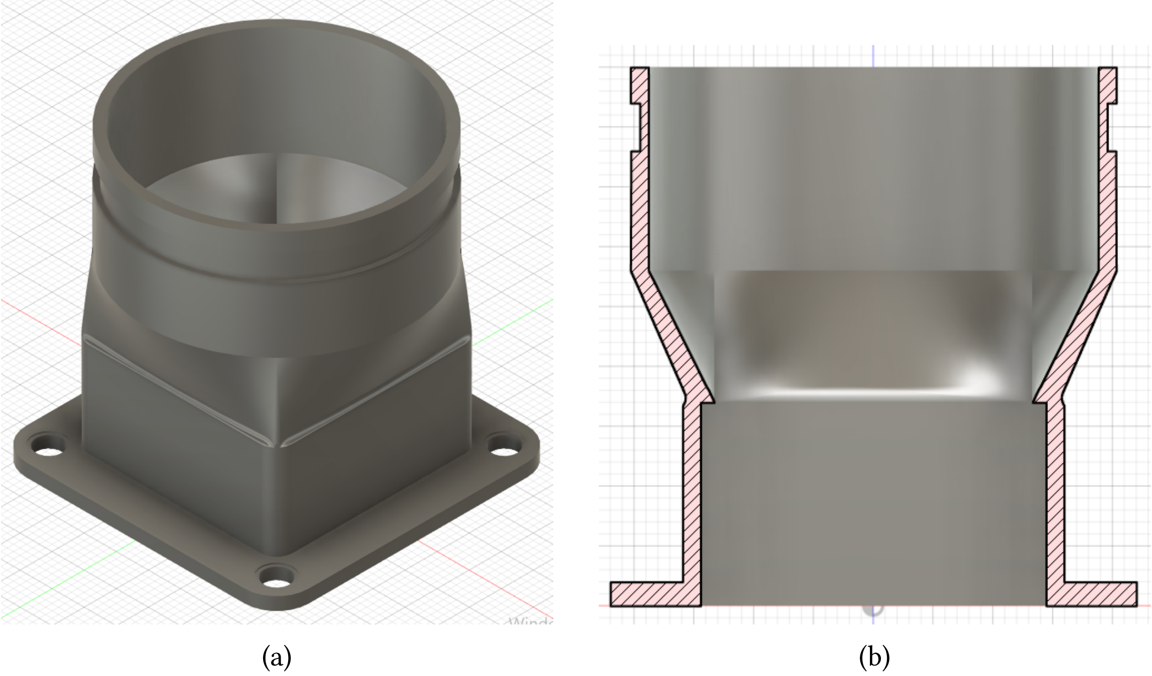
(a) (b)

Figure 4.9.: Figure 4.9a offers an isometric view of the 3D model for the mechanical coupling system, meticulously designed so that the hole spacing aligns perfectly with that of the CAEN adapter. This precise alignment ensures a seamless integration of components, crucial for the stability and functionality of the system. Figure 4.9b displays the same 3D model but with a cross-section, providing an insightful look into the bracket's internal structure.

an adhesive. This mask is composed of 51 identical square sections, each channeling two optical fibers towards a single SiPM in the array. The dimensions of these squared sections and the diameter of the two holes for the fibers are specified as 3.2 x 3.2 mm and 1.4 mm, respectively, indicating placeholders that should be replaced with actual measurements. Adjacent to the fiber holes is an additional hole intended to facilitate the adhesive's application.

Significantly, five out of the 13 guiding components on the left side are equipped with four holes each, catering to the coincidence layer by directing four fibers from the scintillator bars to a single SiPM. The remaining eight components are slightly lower in height but also feature holes, serving as reservoirs for slow-flowing glue during the assembly process. This design ensures optimal adhesive distribution, crucial for the stable and effective positioning of optical fibers within the system.

During the assembly process, a base, as illustrated in Figure 4.11, is positioned underneath the mask to ensure uniform fiber length and serve as a containment area for excess glue. Following the application of glue, this base undergoes a meticulous sanding and polishing procedure until its surface is seamlessly aligned with the onset of the array mask. The upper portion of this base is designed to be 0.3 mm thick, facilitating a precise fit. To enhance the manufacturability of the base, its thicker section is crafted with a 45° angle,

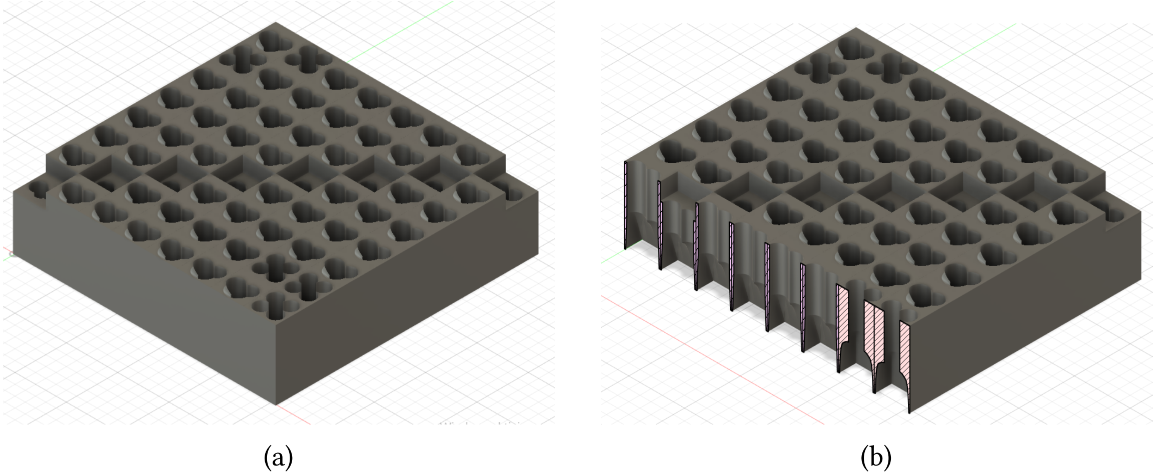

(a) (b)

Figure 4.10.: Figure 4.10a presents an isometric view of the 3D model for the mask array, meticulously designed to hold and guide either two or four optical fibers towards a single SiPM, facilitating precise alignment and efficient signal transmission. Figure 4.10b depicts the same 3D model but with a cross-section, offering a clear visualization of the internal structure. This cross-sectional view elucidates the intricate design that enables the mask array to efficiently channel optical fibers, underscoring the sophisticated engineering behind the “MIP-Cube” project.

a modification intended to streamline the 3D printing process. This thinner section is engineered to snugly fit within the frame depicted in Figure 4.12, ensuring a cohesive and stable assembly of the entire system.

The design meticulously prevents adhesive leakage, thereby enhancing the efficiency and cleanliness of the assembly process. The frame is engineered to fit precisely into the bracket, with its upper, slender segment designed to interlock seamlessly with the connector, as depicted in Figure 4.13. This integration, in conjunction with the connector, is crucial for securely anchoring the mask within the mechanical bracket. The primary objective of this coupling system’s design is to ensure the optical fibers are firmly pressed against the SiPM array, thereby optimizing signal detection while minimizing the potential for misalignment or light leakage.

Detailed assembly instructions are provided in Figure 4.14, offering clear visual guidance for the setup process. The completion of the assembly process, with the optical fibers securely glued into position, is showcased in Figure 4.8. This figure exemplifies the successful realization of the coupling system, underscoring the precision and effectiveness of the design in achieving optimal alignment and signal integrity.

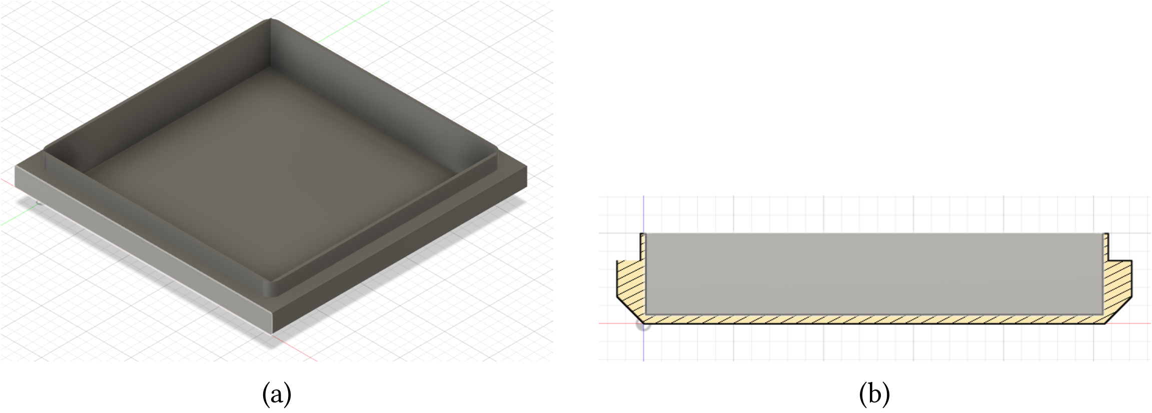
(a) (b)

Figure 4.11.: Figure 4.11a - An isometric view on the 3D model for the bottom of the coupling system. It stores the glue and after the glue is hardened, it is sanded down Figure 4.11b - Same 3D model with a cross-section to visualise the inner structure.

For accurate identification of each scintillator pixel, it is crucial to know which scintillator is connected to which SiPM in the SiPM-array. To facilitate this, a mapping has been designed and is illustrated in Figure 4.15. For assignment purposes, each scintillator bar in the pixel layers is given a unique designation that specifies its position and side. The sides are labeled with the letters *A* to *E*, and each bar within the pixel layers is assigned a number from 1 to 10, as shown in Figure 4.16. The coincidence layer is marked with *C*. This numbering scheme is also utilized in Figure 4.15. The mapping is strategically designed to ensure that adjacent scintillators are not connected to adjacent SiPMs in the array to avoid cross-talking with multiple SiPMs of the array. Due to an oversight in symmetric reasoning, only channels A9 and AC have been adjusted and aligned on the same cube side. In the Figure, bars with the same number on each side are grouped and color-coded, and the nine unused SiPMs are indicated in black. In the array mask of the coupling system (Figure 4.10), these are visible as the recessed parts of the mask, which serve as additional glue storage during the gluing process. Additionally, reserved spaces for the trigger layer fibers are indicated by the presence of four holes instead of two. Only channel A9 and AC are adjusted and in the same plane, because of a symmetric thinking fault.

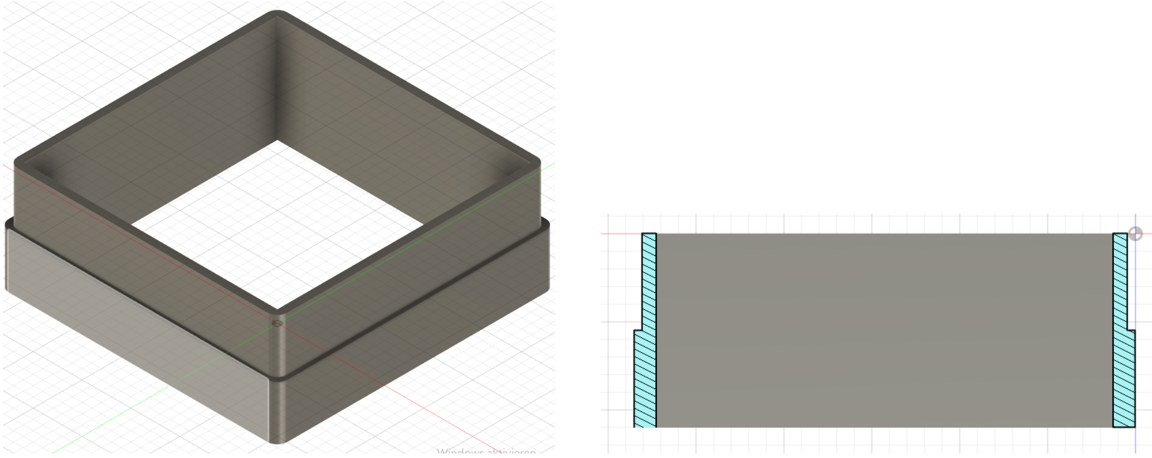
(a) (b)

Figure 4.12.: Figure 4.12a - An isometric view on the 3D model for the frame. it holds the mask array and the bottom together and prevents the glue from leaking. Figure 4.12b - Same 3D model with a cross-section to visualise the inner structure.

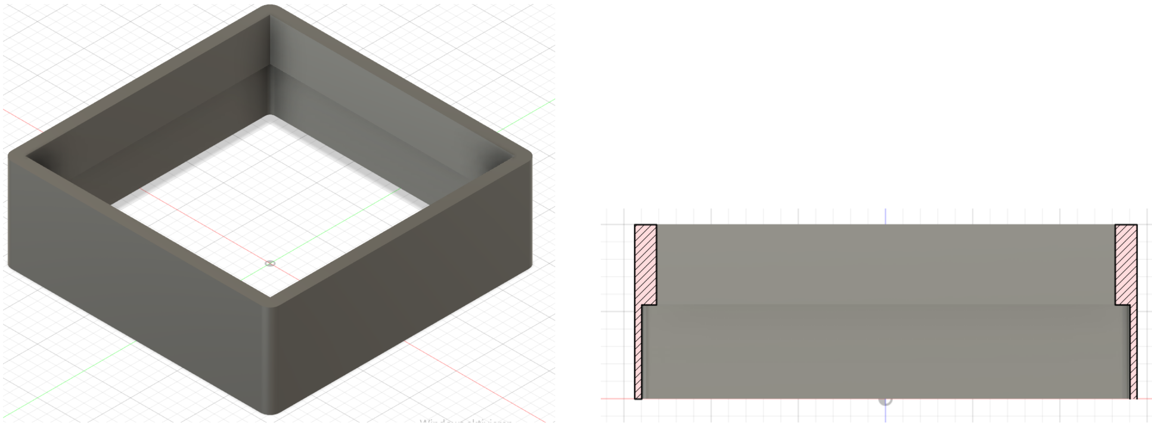
(a) (b)

Figure 4.13.: Figure 4.13a - An isometric view on the 3D model for the connector of the coupling system. It secures the frame inside the mechanical bracket. Figure 4.13b - Same 3D model with a cross-section to visualise the inner structure.

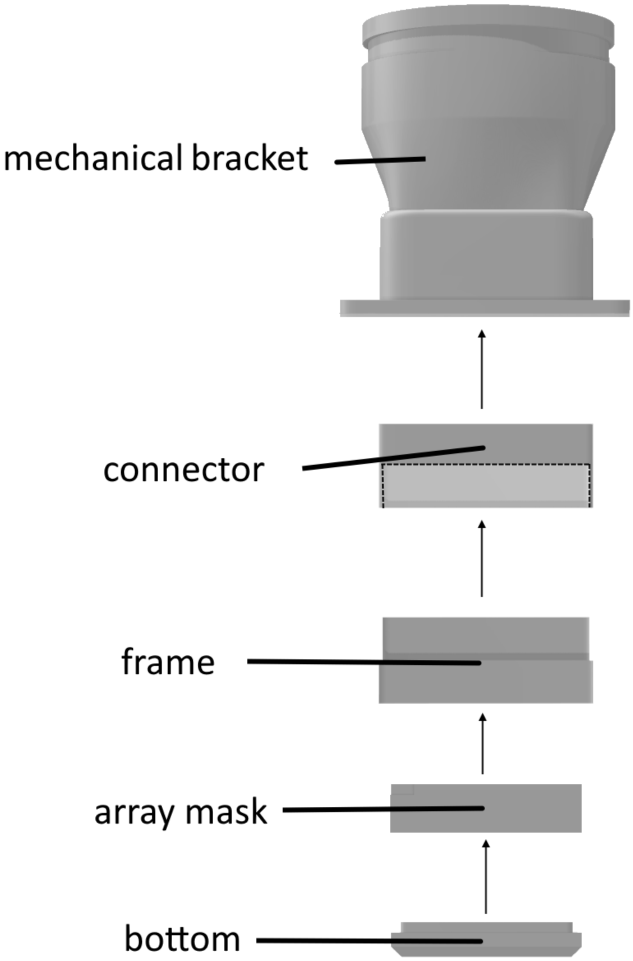

Figure 4.14.: Construction instruction for the mechanical coupling system.

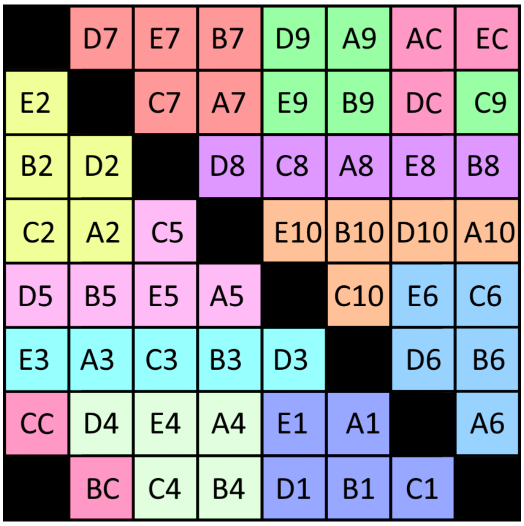

| | | | | | | | |
|---|---|---|---|---|---|---|---|
| ■ | D7 | E7 | B7 | D9 | A9 | AC | EC |
| E2 | ■ | C7 | A7 | E9 | B9 | DC | C9 |
| B2 | D2 | ■ | D8 | C8 | A8 | E8 | B8 |
| C2 | A2 | C5 | ■ | E10 | B10 | D10 | A10 |
| D5 | B5 | E5 | A5 | ■ | C10 | E6 | C6 |
| E3 | A3 | C3 | B3 | D3 | ■ | D6 | B6 |
| CC | D4 | E4 | A4 | E1 | A1 | ■ | A6 |
| ■ | BC | C4 | B4 | D1 | B1 | C1 | ■ |

Figure 4.15.: Mapping for the 8x8 SiPM-array involves assigning each letter to represent a specific scintillator on a side of the cube. To facilitate better allocation, a sketch is provided in Figure 4.16. This mapping strategy is carefully designed to prevent connecting a scintillator on the same side to an adjacent SiPM. Furthermore, scintillators sharing the same number on each side are grouped together and color-coded for ease of identification. Notably, nine SiPMs are unused and are marked in black.

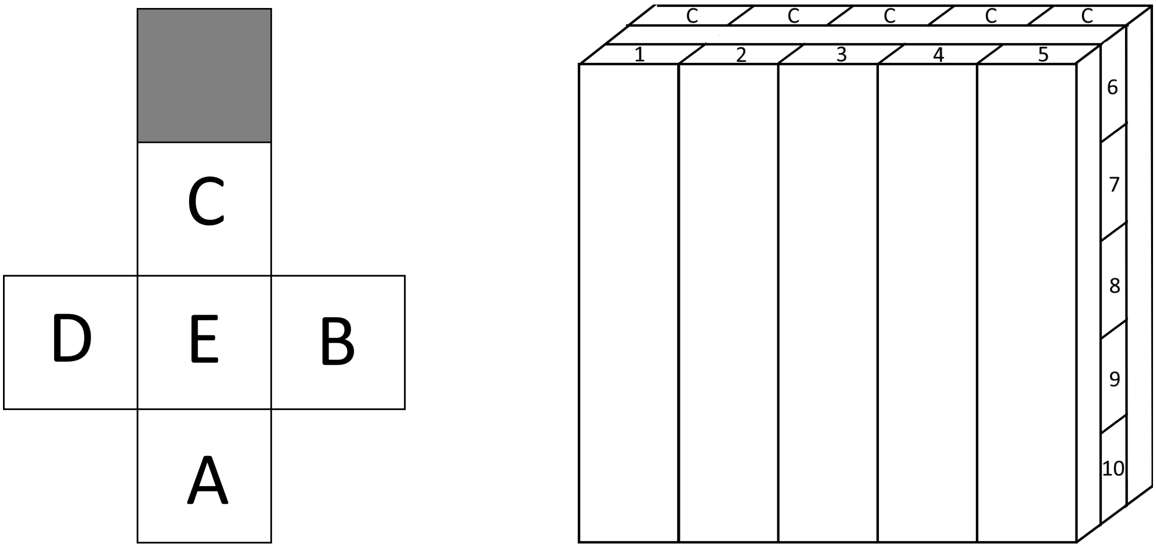

(a)

(b)

Figure 4.16.: Figure 4.16a - The geometric net of a cube with sides labeled *A* to *E*, with each letter representing a scintillator-covered side of the "MIP-Cube". The second letter C represents the coincidence layer considering of five connected bars. Figure 4.16b - The numbering from 1 to 10, indicating the horizontal and vertical scintillator bars within each pixel layer, as the configuration documented in Figure 4.16a.

## 4.5. Routing

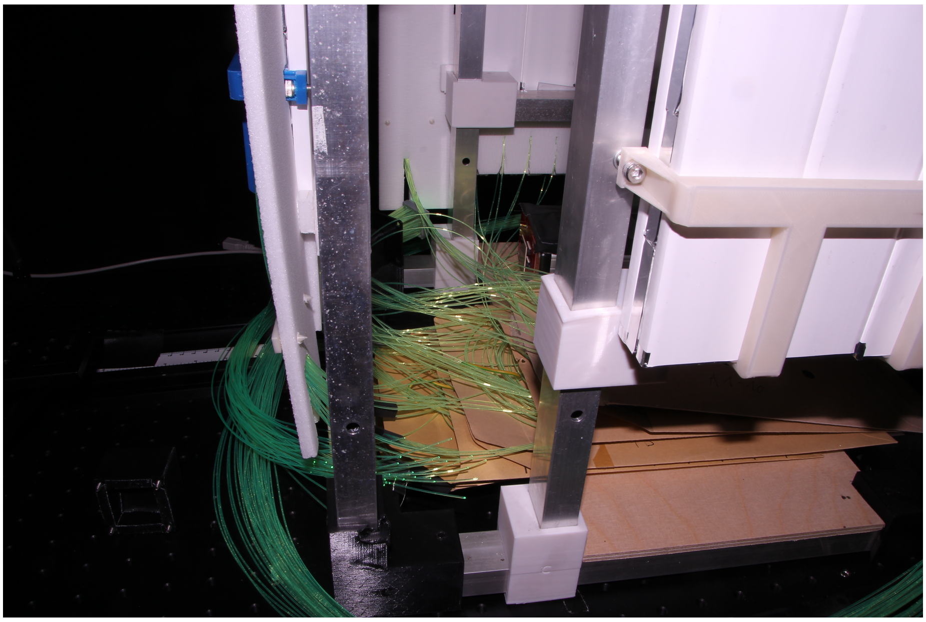

Figure 4.17.: Closer view on the stored fibers at the bottom of “MIP-Cube”. In the background the DT5202 with mounted SiPM-array is visible.

To ensure a secure connection between the scintillator and the SiPMs, the optical fibers must be routed around corners and edges with a minimum bending diameter of 10 cm. Styrofoam is utilized for this purpose, providing guidance from each scintillator layer to the inner side of the cube. In addition to accommodating the bending diameter, the fibers must also be routed beneath the lead layer. For prototyping purposes, the design approach was adjusted to facilitate the assembly process, resulting in the current models being based on the presented concepts. Specifically, for sides *A* to *C*, the routing for the vertical bars follows a uniform design, as shown in Figure 4.18a. This routing is secured in place using styrofoam spacers and double-sided tape. The rectangular protrusions at the upper side of the model are designed to accommodate scintillator holders. Additionally, the routing features a funnel-shaped entrance, carefully guiding the fiber into the tunnel that leads it securely inside. The semi-circular bulges along the routing path are strategically placed to keep the fibers securely positioned. Following this design principle, the concept is consistently applied across all routing models; wherever the fiber exits the scintillator for the first time, a secure bulge is strategically positioned to ensure the fiber’s stability and protection.

The same design principle is illustrated in Figure 4.18b, which depicts the routing for the horizontal Fermilab bars. This routing arrangement effectively guides the optical fibers downwards and into the interior of the cube, positioning them beneath the lead shield. This strategic routing ensures the overall functionality and reliability of the “MIP-Cube” system.

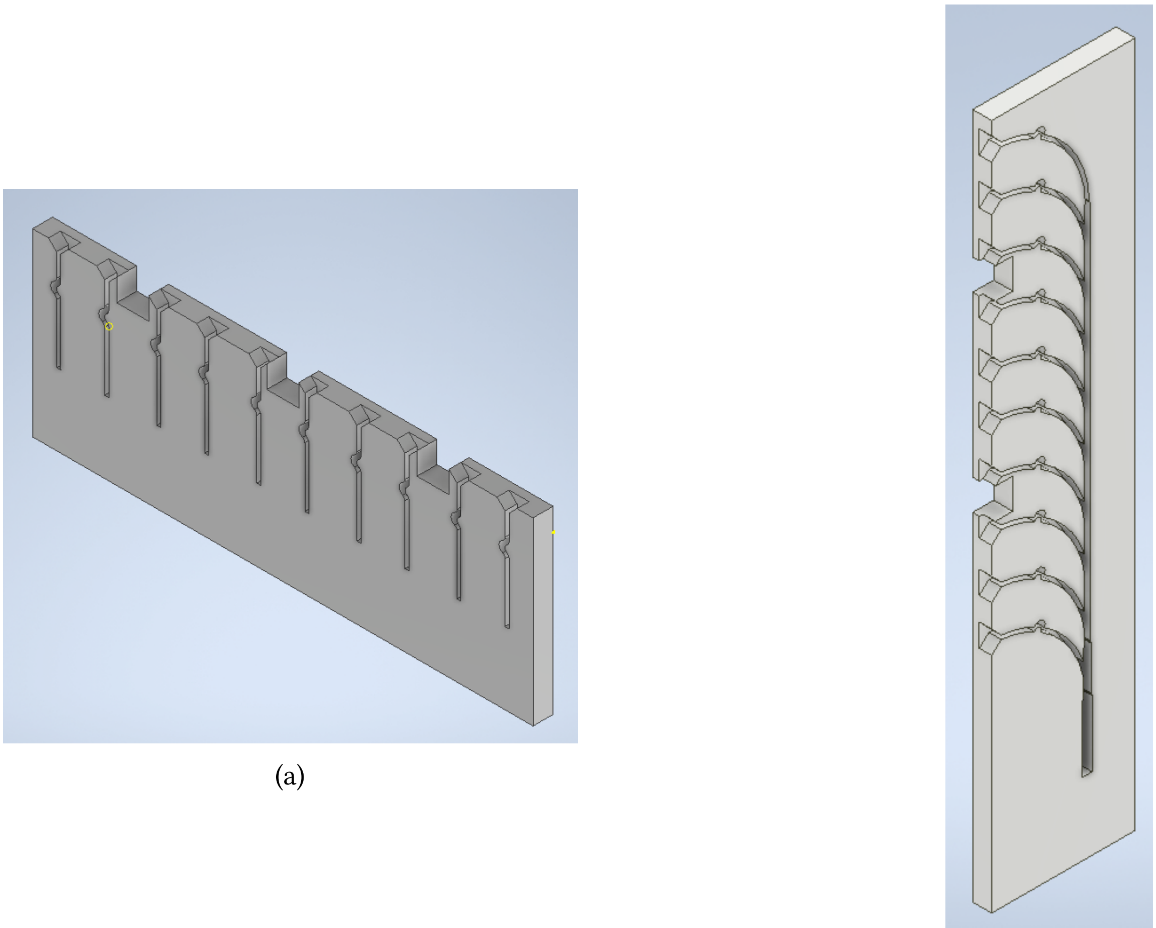

(a)

(b)

Figure 4.18.: Figure 4.18a - Routing for the vertical pixel layers at the vertical sides $A$ to $C$. Figure 4.18b - Routing for the horizontal pixel layers at the vertical sides $A$ to $C$.

The lower part of the routing for the coincidence layer of sides *A* to *C* is illustrated in Figure 4.19a it fulfills the requirement of connecting two scintillator bars and guiding the fibers inside the cube. The same fiber secure system is used as before. The Figure 4.19b illustrates the same routing principle but for the top side *E*. It guides the fibers to left, from there they are guided downsides and inside the cube.

The routing design for the lower part of the coincidence layer on sides *A* to *C* is detailed in Figure 4.19a, showcasing how it meets the crucial requirement of connecting two scintillator bars while guiding the fibers into the cube's interior. This design employs the same fiber secure system previously described, ensuring consistency in fiber management and protection across the cube. Figure 4.19b further exemplifies this routing principle, albeit for the top side *E*. In this configuration, the fibers are directed towards the left, from where they are then guided downwards and into the cube.

As depicted in Figure 4.7, the incorporation of the coincidence layer necessitates additional space at both lateral sides of the cube. In response to this requirement, a compact routing design, as demonstrated in Figure 4.19b, was conceived. This design efficiently minimizes spatial requirements through the strategic use of styrofoam, while also ensuring secure fiber routing. Its applicability is particularly suited to scenarios where fibers connect between scintillators rather than routing internally within the cube. This compact routing approach is uniformly applied across all coincidence layers, with an exception for side *D*, where it is specifically implemented at the base. This methodical design choice effectively addresses spatial constraints, maintaining the "MIP-Cube's" compact form without compromising the routing system's effectiveness and security.

The top layer pixel fibers are guided differently to the SiPM. Before they got inside they heave to be leaded beneath the lead shield. Therefore the fibers go to one point and from there thy guided together with the fiber of side *B* interior the cube. The same methodology is used to secure the position of the fibers and the position of the routing.

This necessitates a minimum fiber length of $l_{min} = 2.2\,\mathrm{m}$, particularly for fibers of one pixel and the coincidence layer from side *D*, which must be extended over side *E* to the bottom, as the lead shield is accessed from side *D*. The coincidence routing looks similar to the one in Figure 4.20a. The pixel routings are depicted in Figure 4.22. The fibers of the vertical bars are guided with the routing in Figure 4.22a to the left and as mentioned over side *E* to the bottom. The routing for the horizontal pixel layer in Figure 4.22b is guided to the bottom left afterwards around one aluminum profile and inside the cube. Along with side *E*, 38 of the 120 fibers are directed from the top to the bottom, passing under the lead layer. To manage this quantity of fibers on the styrofoam, a holder has been designed, as illustrated in Figure 4.23. For organizing the fibers at the bottom of the cube, envelopes are utilized for each individual layer, as depicted in Figure 4.17. Since the fibers act as scintillator the indirect of two sides could worsen the reuslt of "MIP-Cube". It could may necessary to use an additional lead shield at this part of the routing.

This configuration necessitates a minimum fiber length of $l_{min} = 2.2\,\mathrm{m}$ especially for the fibers associated with a single pixel and the coincidence layer from side *D*. These fibers must extend over side *E* to reach the cube's bottom, accommodating the entry point for

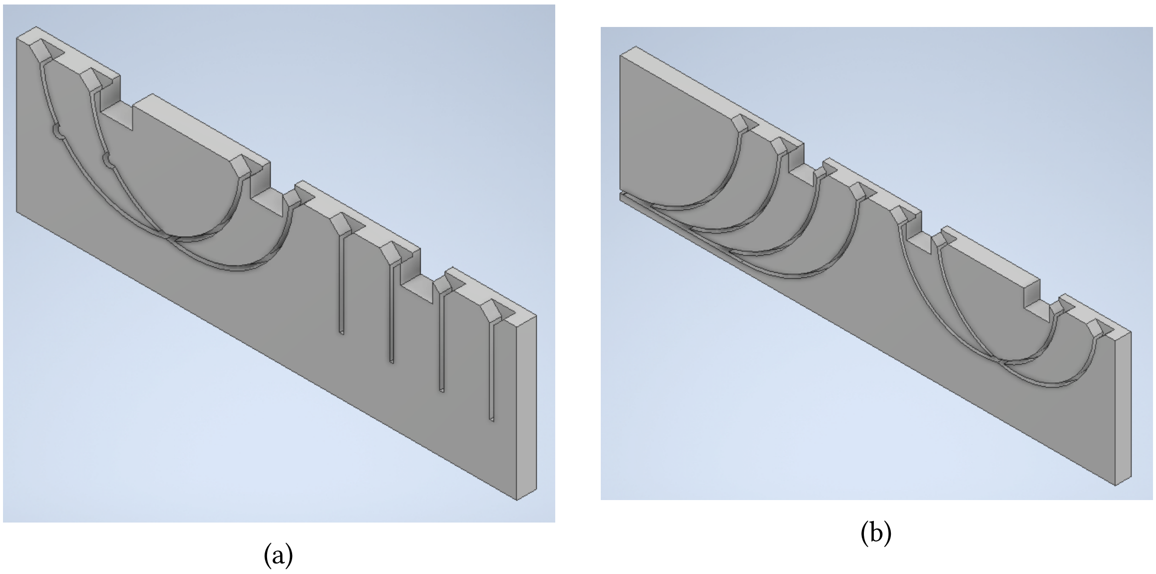
(a) (b)

Figure 4.19.: Figure 4.18a - The routing design for the coincidence layer incorporates a strategic approach where two fibers are connected through a semi-circle, facilitating a smooth transition and alignment. Additionally, four fibers are guided into the interior of the cube. Figure 4.18b - Routing for the horizontal pixel layers at the vertical sides *A* to *C*.

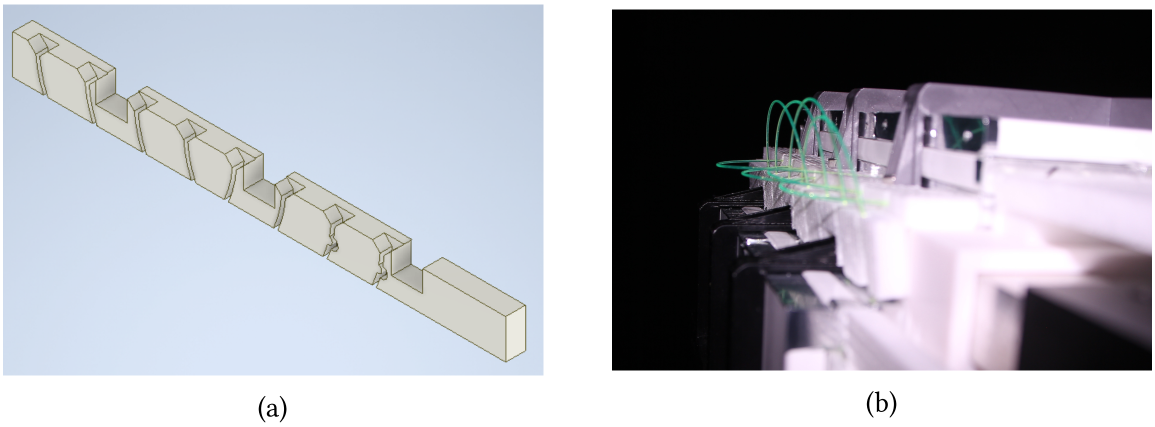
(a) (b)

Figure 4.20.: Figure 4.20a - Illustrates the routing design for the upper part of the coincidence layer, which connects three scintillator bars. In an effort to conserve space on one side of the cube, this design partially covers the fibers. This approach ensures a minimal gap between adjacent scintillator sides while still providing secure guidance for the fibers as they route from one scintillator to the next. Figure 4.20b - Showcases an image of two coincidence routings that overlap. The fibers are guided securely and effectively between scintillators.

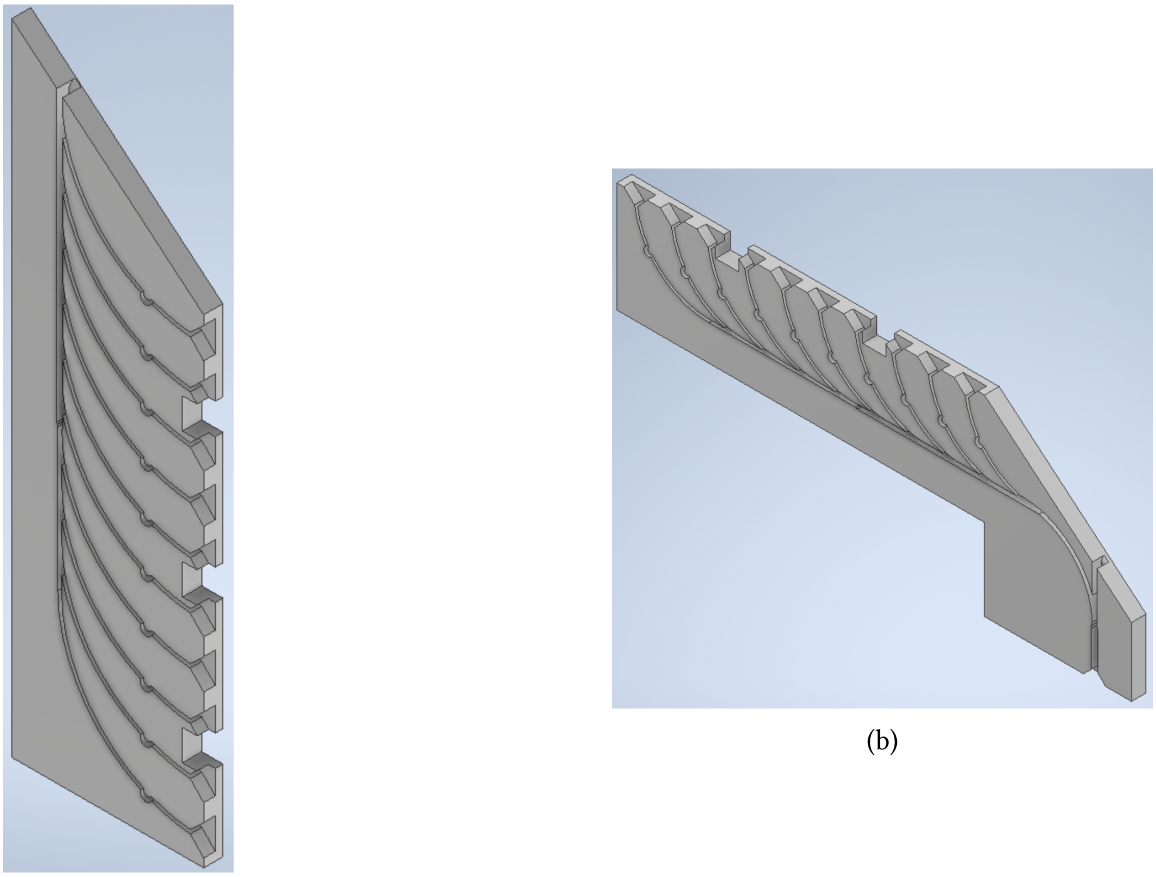

(a)

(b)

Figure 4.21.: Figure 4.21a - Illustrates the routing for the pixels on the top side, employing the same methodology used for the other pixel sides. This routing provides direct guidance to the same area where the coincidence layer fibers are directed downwards. Figure 4.21b - Showcases the second routing approach for the pixel fibers on the top side, guiding the fibers to the right, then downwards, and finally into the interior of the cube.

the lead shield from side *D*. The coincidence layer's routing bears resemblance to that shown in Figure 4.20a, while the specific pathways for the pixel routings are outlined in Figure 4.22. For the vertical pixel bars, the routing strategy depicted in Figure 4.22a directs the fibers to the left and, as previously described, over side *E* and *B* to the cube's base. The horizontal pixel layer routing, illustrated in Figure 4.22b, is navigated to the bottom left, then around an aluminum profile, and finally into the cube's interior. Alongside side *E*, a total of 38 out of 120 fibers are routed from the top to the bottom, passing beneath the lead shield. To accommodate this volume of fibers on the styrofoam, a specialized holder has been developed, showcased in Figure 4.23. At the cube's base, envelopes are employed to organize the fibers for each layer, as demonstrated in Figure 4.17. Given that the fibers serve as scintillators, indirect routing between two sides might impact the "MIP-Cube's" effectiveness. Consequently, an additional lead shield may be required to optimize the routing section's protection.

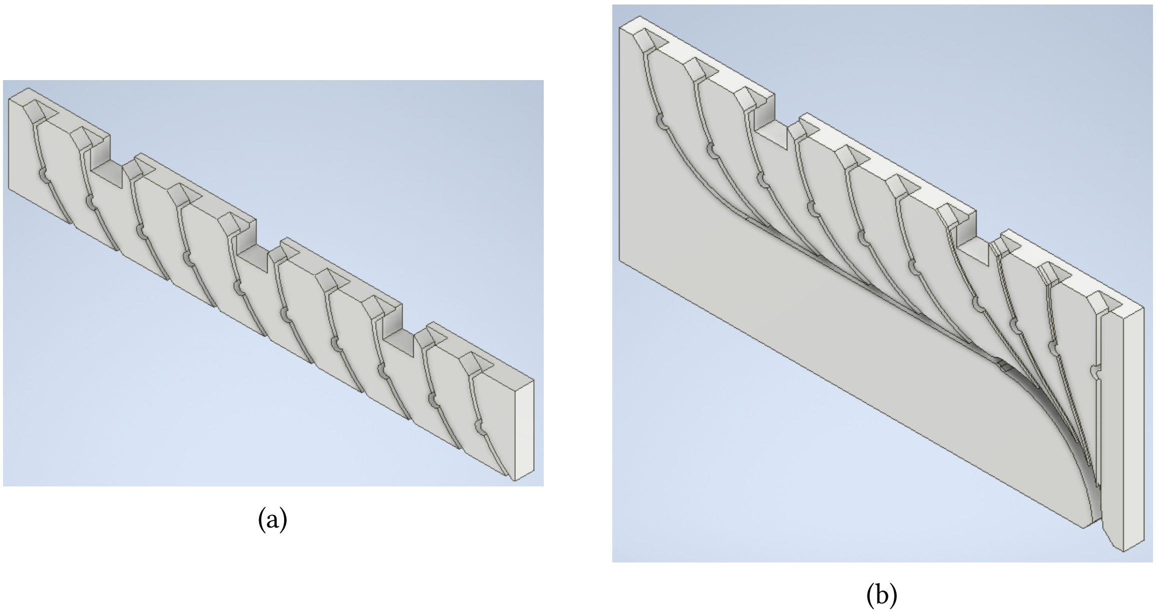

(a)

(b)

Figure 4.22.: Figure 4.22a - Illustrates an alternative routing method for pixel fibers on side *D*, directing the fibers downwards to the left, around the aluminum profile, and ultimately into the cube's interior, positioned beneath the lead shield for added protection. Figure 4.22b - Showcases the second routing approach for the pixel fibers on the side *D*, guiding the fibers to the downwards left, around the aluminum profile and finally into the interior of the cube beneath the lead shield.

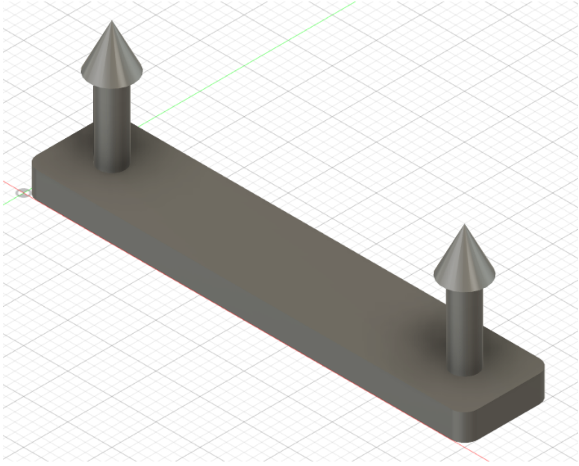

Figure 4.23.: 3D model of a fiber holder, designed to secure optical fibers atop a styrofoam base.

The total weight of the device, encompassing all aluminum profiles, 3D prints, routing sections, and scintillators, amounts to 16.2 kg. Additionally, a flat lead shield with a thickness of 1 cm and dimensions of 33 x 36 cm , which was not available by the conclusion of this thesis, would contribute an extra 13.6 kg to the overall weight.

# 5. Measurements

## 5.1. Measuring Hardware Characteristics of DT5202

### Identify SiPM-numbering of *Janus*

The primary goal of these measurements is to confirm the accuracy of the hardware mapping within the CAEN Software *Janus*. This confirmation is crucial due to discrepancies between the numbering systems described in the CAEN [46] and Hamamatsu [37] manuals. Accurately correlating the SiPM numbers assigned by *Janus* with the actual SiPMs is vital for the mapping process detailed in Chapter 4.4.

To perform the measurement, a single fiber is carefully connected to an SiPM at the bottom right corner of the array and illuminated with a Light Emitting Diod (LED). This arrangement affects both counting and spectroscopy modes, offering insights into the array mask's effectiveness (Figure 4.10) in preventing cross-talk light between adjacent SiPMs.

Each measurement is conducted in the light-proofed SPOCK laboratory at KIT [8], with an exposure time of five minutes.

In spectroscopy mode, notable shifts in the histogram peak and changes in the curve's shape are observed, particularly for channel 61 as shown in Figure 5.1a. Figure 5.1b displays the counts for each SiPM. Remarkably, Figure 5.2a demonstrates significantly fewer counts in the ADC channels below 2000, indicating that this channel is connected to the fiber.

A comparative analysis of Figure 5.1b and Figure 5.2b, focusing on the counting mode, shows that channel 61 has a significantly higher count compared to other SiPM channels and its own counts in Figure 5.2b. These observations, combined with the spectroscopy mode results, further confirm that channel 61 is the connected channel.

This measurement substantiates the alignment between the *Janus* mapping and the actual hardware configuration. It specifically verifies that the mapping and assignment by *Janus* precisely mirror the hardware layout, aligning the physical array's bottom right corner with the software-represented array's bottom right corner in Figure 5.1b, and identifying channel 61 as the corresponding SiPM channel. Consequently, modifying the fiber connection to the bottom left corner necessitates a software-side adjustment to channel 35, located in the same position. This modification is documented and visualized as counting mode in Figure 5.3. As predicted, channel 35 displays a significantly higher count, underscoring the effective mapping adaptation.

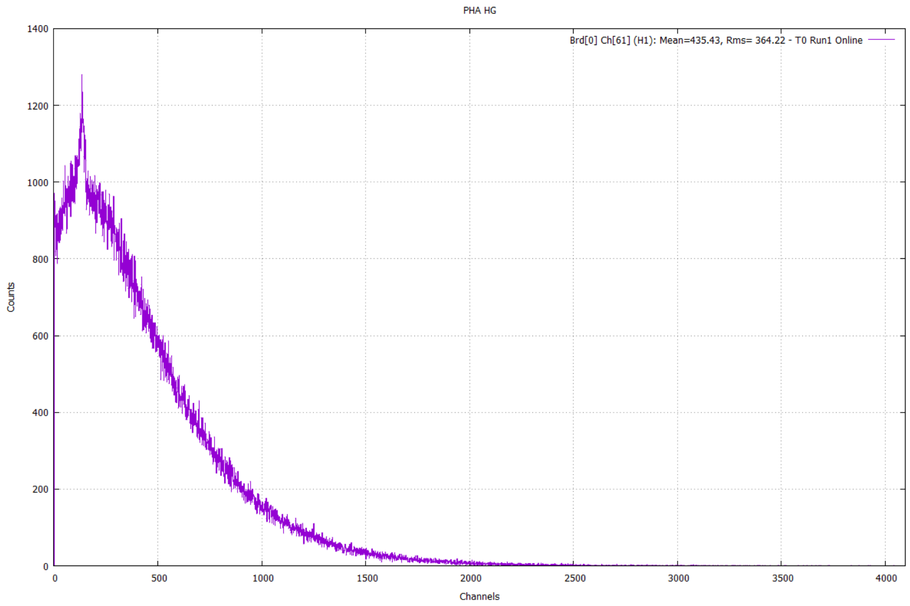

(a) ADC spectrum of the single SiPM channel 61

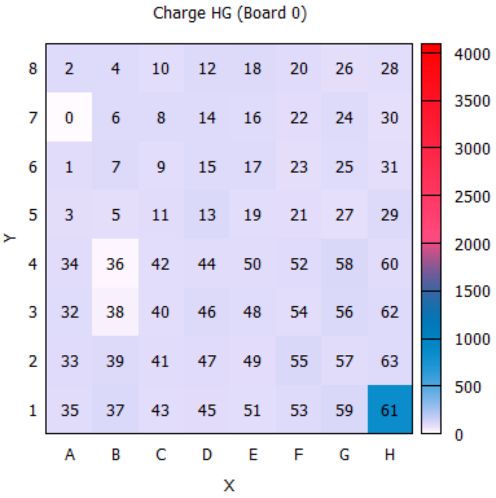

(b)

Figure 5.1.: Figure 5.1a - The ADC-spectrum of a single illuminated SiPM with the *Janus* given number 61. Figure 5.1b - Counts of entire array at each SiPM by *Janus* with the one illuminated channel 61.

The initial mapping of the SiPM-array of *Janus* appeared disorganized. To clarify the readout and consolidate mapping insights, nine fibers were meticulously connected to specific channels of the SiPM-array (11, 12, 18, 35, 36, 50, and 53), as illustrated in Figure 5.4a. This setup was illuminated using a LED, and the results, captured in counting mode, are presented in Figure 5.4a. The illuminated channels registered significantly higher counts, approximately 3000 times those of the non-illuminated SiPMs.

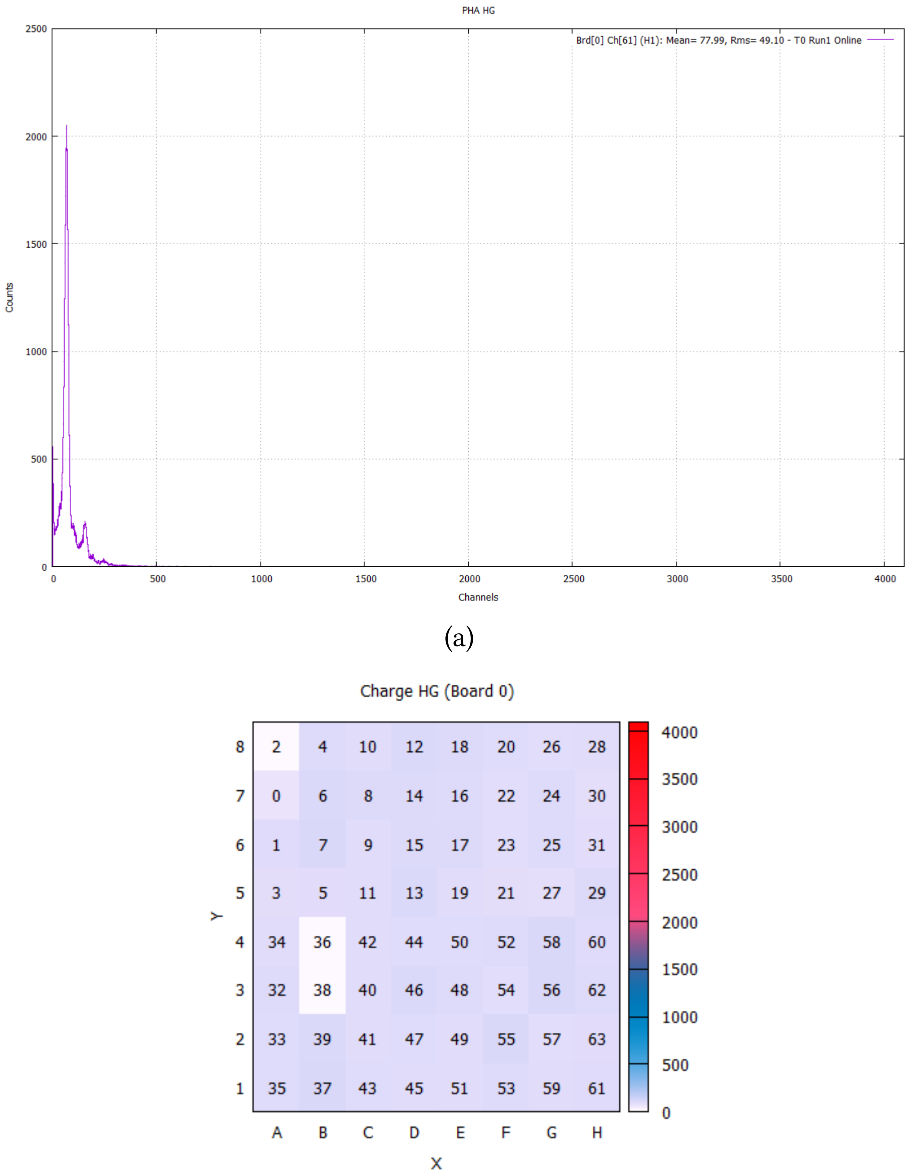

(a)

(b)

Figure 5.2.: Figure 5.2a - The ADC-spectrum of a single non-illuminated SiPM (channel 61). Figure 5.2b - Counts of the array with no illuminated SiPM.

An exception was observed with the channels 52, located at position 5/4, which recorded counts at one-third the level of the illuminated channels. This discrepancy suggests a potential flaw in the array mask at this juncture, indicating ineffective light shielding. Alternatively, it may imply insufficient fiber connections. Consequently, a new mask was fabricated to enhance light shielding effectiveness. To ensure an optimal connection for the “MIP-Cube” to the SiPM-array, the fibers were securely glued and pressed onto the array, as detailed in Chapter 4.4.

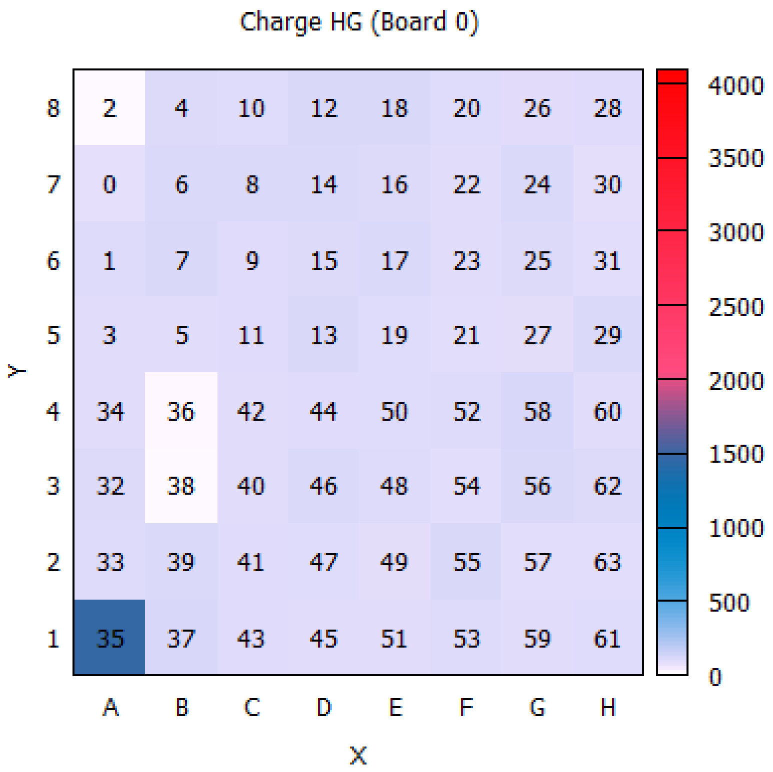

Figure 5.3.: Array in counting mode, illustrating a single fiber connected to the SiPM array at the bottom left corner. Illuminated with a LED.

A reorganized arrangement, positioning channel one in the bottom left corner and channel 64 in the upper right corner, yielded a pattern resembling a smiley emoticon, as shown in Figure 5.4b. The sorting algorithm presented in Section A.2 arranges an array from the top left corner to the bottom right corner, covering channels 0 through 64. To align with the assignment described in this chapter, the order of the lines must be inverted. The issue has been resolved by utilizing an enhanced array mask, produced with improved printing quality, and by applying additional adhesive to the fibers to ensure their secure placement, as opposed to merely positioning them without adequate fixation. Through this experimental process, the numerical assignments of *Janus* were deciphered, aligning with the hardware mapping. With the mapping displayed in Figure 5.3, individual channels can now be accurately identified.

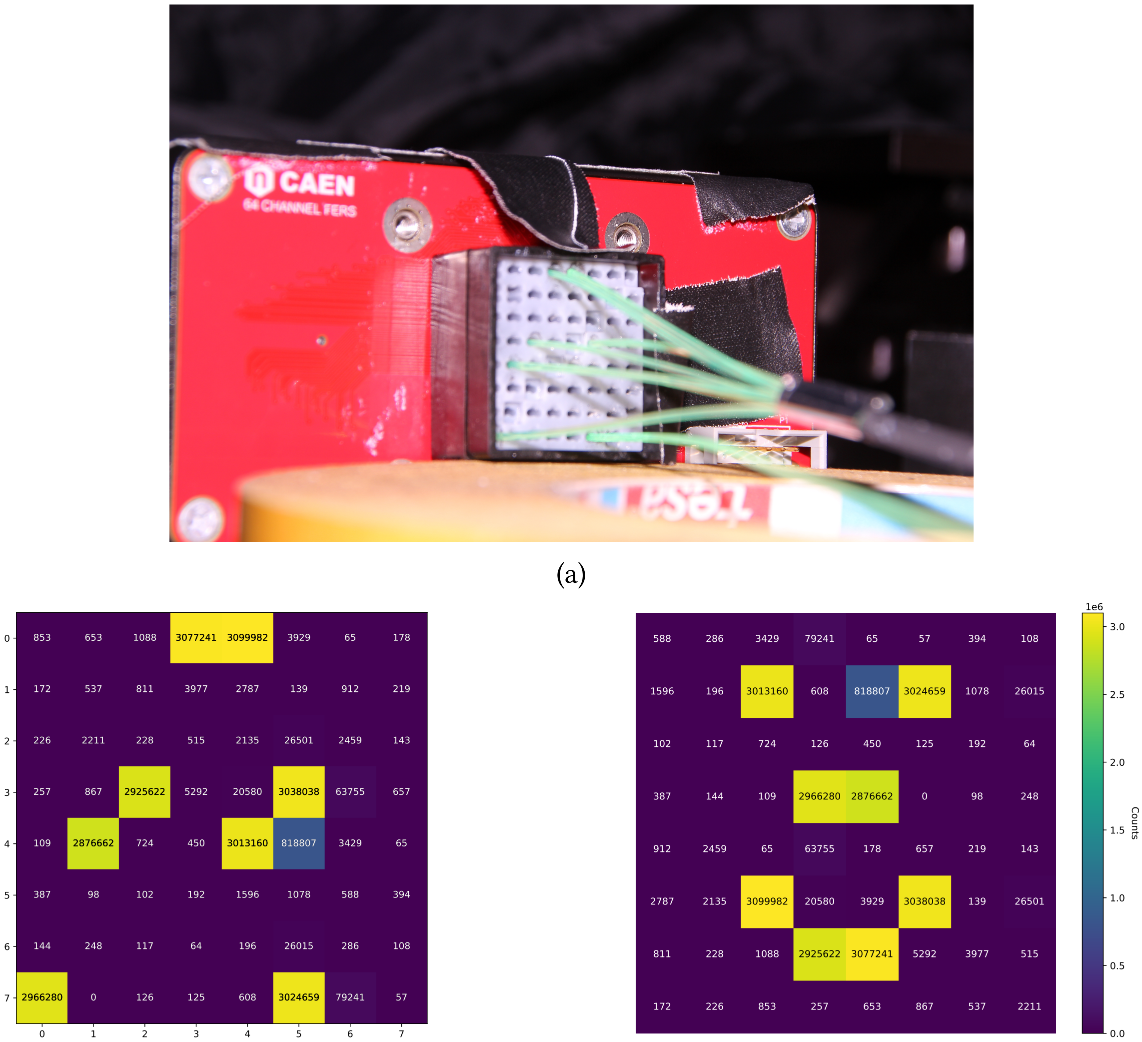

(a)

|  | 0 | 1 | 2 | 3 | 4 | 5 | 6 | 7 |
|---|---|---|---|---|---|---|---|---|
| 0 | 853 | 653 | 1088 | 3077241 | 3099982 | 3929 | 65 | 178 |
| 1 | 172 | 537 | 811 | 3977 | 2787 | 139 | 912 | 219 |
| 2 | 226 | 2211 | 228 | 515 | 2135 | 26501 | 2459 | 143 |
| 3 | 257 | 867 | 2925622 | 5292 | 20580 | 3038038 | 63755 | 657 |
| 4 | 109 | 2876662 | 724 | 450 | 3013160 | 818807 | 3429 | 65 |
| 5 | 387 | 98 | 102 | 192 | 1596 | 1078 | 588 | 394 |
| 6 | 144 | 248 | 117 | 64 | 196 | 26015 | 286 | 108 |
| 7 | 2966280 | 0 | 126 | 125 | 608 | 3024659 | 79241 | 57 |

(b)

|  |  |  |  |  |  |  |  |
|---|---|---|---|---|---|---|---|
| 588 | 286 | 3429 | 79241 | 65 | 57 | 394 | 108 |
| 1596 | 196 | 3013160 | 608 | 818807 | 3024659 | 1078 | 26015 |
| 102 | 117 | 724 | 126 | 450 | 125 | 192 | 64 |
| 387 | 144 | 109 | 2966280 | 2876662 | 0 | 98 | 248 |
| 912 | 2459 | 65 | 63755 | 178 | 657 | 219 | 143 |
| 2787 | 2135 | 3099982 | 20580 | 3929 | 3038038 | 139 | 26501 |
| 811 | 228 | 1088 | 2925622 | 3077241 | 5292 | 3977 | 515 |
| 172 | 226 | 853 | 257 | 653 | 867 | 537 | 2211 |

(c)

Figure 5.4.: In Figure 5.4a: The DT5202 with mounted SiPM-array and array-mask with nine connected Kuraray fibers. Figure 5.4b: The matrix illustration of the *Janus* given 8x8 channel array numbering. In Figure 5.4c: Sorted array from bottom left corner channel one to upper right corner channel 64. This configuration is illuminated with a LED.

### Position of MIP-Peak

The DT5202 and *Janus* software provide the capability to perform a Peak High Analysis (PHA) within the ADC-spectrum. This analysis evaluates the peak produced by each SiPM and records its height in an ADC-channel. The maximum number of photo-electrons detectable is 2500 p.e., with noise constituting approximately 1 % of the signal; the pedestal is situated at ADC-channel 40 [45]. As described in Chapter 3.1, a MIP is expected to yield 40 to 50 p.e., corresponding to an ADC-channel range of 64 to 80. Consequently, a typical peak in the ADC spectrum of a MIP, when combined with the pedestal, is superimposed in this PHA analysis during spectroscopy mode. Figure 5.2a presents a dark count measurement, whereas Figure 5.5 shows the spectrum of the same SiPM connected to a scintillator. Though approaches of a spectrum can be seen in the ADC-channels around 250. However, a similar peak is also visible in the PHA dark-count spectrum. While an increased counts at lower ADC-channels is visible, no distinct peak can be identified in this mode. In conclusion this mode is unsuitable for identifing a MIP peak. Also no statements about the deposited energy can be made with the DT5202.

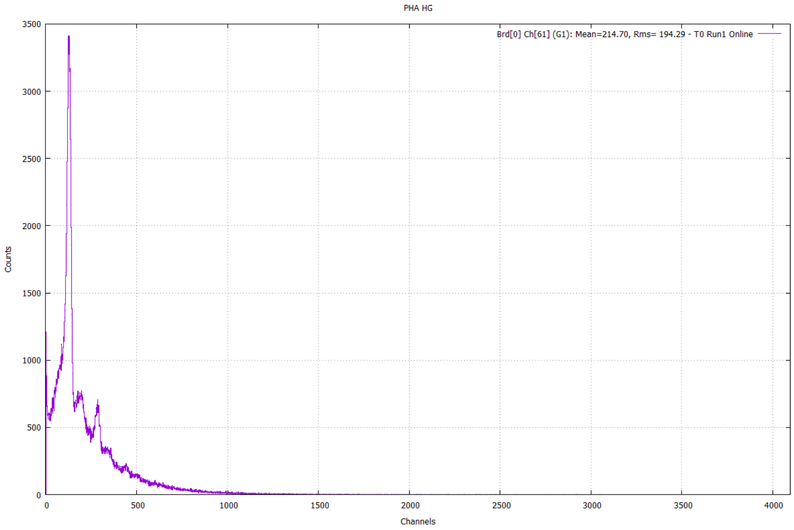

Figure 5.5.: PHA spectrum of one SiPM with a connected scintillator. For comperison Figure 5.6 illustrates the dark counts. No significant difference can be analysed, because of the superimposed with the pedestal.

### MIP-Peak in Counting Mode

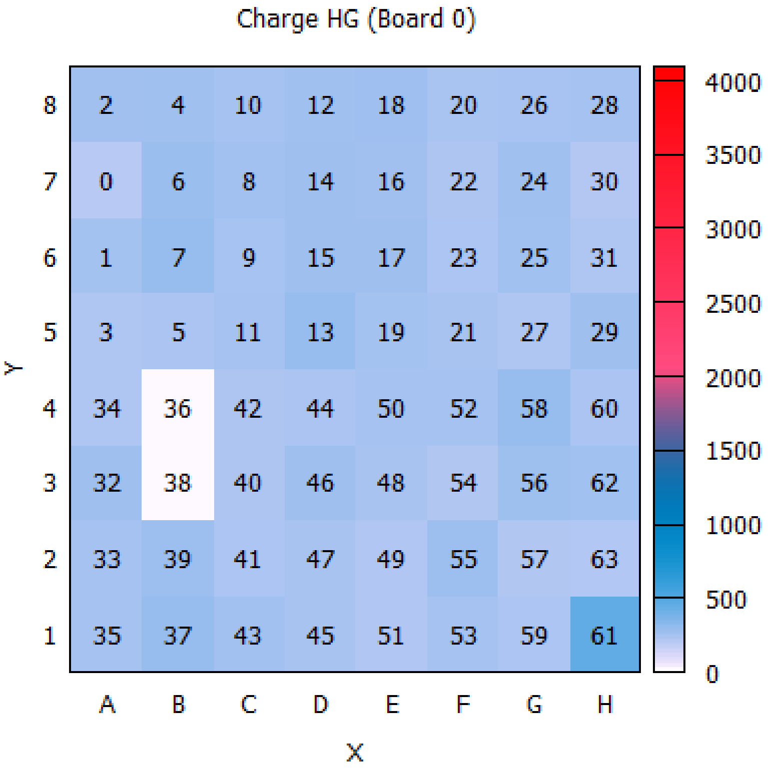

Figure 5.6.: Array in counting mode, illustrating a single fiber connected to the SiPM array at the bottom right corner. Illuminated with a scintillator.

Unlike the spectroscopy mode, the counting mode reveals a significant difference in counts when a scintillator is connected to a SiPM. The experimental setup described in Chapter 5.1 and illustrated in Figure 5.4a is utilized for this measurement, with the LED replaced by a scintillator that connects all fibers. The heat map of this configuration is presented in Figure 5.7, showcasing the hardware assignment in Figure 5.7a and the ordered assignment in Figure 5.7b. The pattern of a smiley emoticon is discernible. Notably, channel 53 registers 500 counts, more than fivefold the counts of the also illuminated channel 12. This discrepancy indicates that calibration is necessary before connecting the "MIP-Cube". Consequently, the HG is adjusted individually for each SiPM.

Utilizing the staircase plot provided by *Janus*, it is possible to observe the counts at each threshold value for every SiPM. Through a measurement of dark counts and setting a standard HG value of 30, the channel registering counts at the highest threshold value is identified. The gain for the remaining channels is then incrementally increased until they also register counts at the given threshold level. Moreover, an alteration in the coupling method is necessitated, as previously mentioned in chapter 5.1. This adjustment is part of the experimental procedure and will be implemented in subsequent steps.

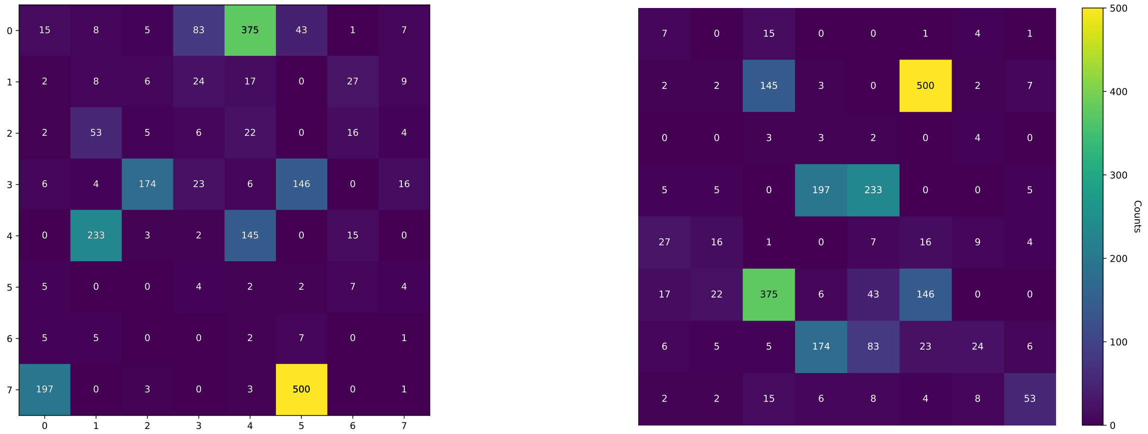
(a) (b)

Figure 5.7.: Figure 5.7a: The matrix illustration of the *Janus* given 8x8 channel array numbering. Figure 5.7b: The sorted array from bottom left corner channel one to upper right corner channel 64. This measurement has the same experimental configuration as explained in Figure 5.4, but with exchanging the LED by a scintillator.

## Testing Coupling

In Figure 4.8, all fibers that have been securely glued in preparation for connection to the scintillators and the DT5202 are depicted. To conduct an initial test of the coupling, the CAEN device along with these fibers were placed in the SPOCK chamber and exposed to a bright LED to ascertain whether the diagonal would be illuminated. The outcomes of this test are shown in Figure 5.8, highlighting the non-illuminated SiPMs along the diagonal and in the bottom right corner. This corresponds with the expectations presented in Figure 4.15 90 degree turned to the left. Additionally, a gradual decrease in light from the bottom left to the upper right corner is observable. This phenomenon is attributed to the positioning of the LED at the bottom right, adjacent to the DT5202, resulting in photon obstruction by the fibers themselves.

This implies that the fibers are now capable of being connected to the scintillators, thereby rendering the “MIP-Cube” operational and prepared for conducting measurements.

| | 0 | 1 | 2 | 3 | 4 | 5 | 6 | 7 |
|---|---|---|---|---|---|---|---|---|
| 0 | 953848 | 170181 | 9031 | 75970 | 13411 | 43169 | 10883 | 45 |
| 1 | 407563 | 647370 | 508617 | 233722 | 221092 | 788083 | 33 | 2448228 |
| 2 | 1460681 | 322555 | 576057 | 809286 | 700331 | 27 | 835981 | 1071582 |
| 3 | 15 | 186125 | 790030 | 139718 | 6 | 965931 | 419712 | 648918 |
| 4 | 1220644 | 781160 | 811813 | 8 | 116871 | 178777 | 1399518 | 849018 |
| 5 | 502283 | 1242716 | 192 | 1193660 | 778973 | 712828 | 419178 | 907546 |
| 6 | 2522027 | 1507 | 851306 | 1935825 | 1809667 | 613786 | 1060339 | 1373713 |
| 7 | 75 | 2246223 | 1544807 | 2615472 | 1283117 | 2255479 | 1297875 | 996 |

Figure 5.8.: All fibers connected are illuminated with a bright LED. The not illuminated diagonal and the single SiPM in the right bottom corner can be identified. Also loss of light from bottom left to upper right.

## 5.2. MIP-Cube Event Building

Addressing the challenge of identifying a MIP, particularly muons, requires elucidation. While a single SiPM channel coupled with a scintillator enables the counting of incoming particle flux, accurate identification demands the integration of multiple scintillator layers. The “MIP-Cube” incorporates three such layers on each cube face, as described in Chapter 4, including two pixel layers and a coincidence layer. The efficacy and necessity of the coincidence layer for particle identification remain questions to be resolved. To tackle these queries, a flow chart has been constructed, as depicted in Figure 4.1, predicated on employing the timing mode of DT5202 and *Janus*. Contrary to the spectroscopy mode, where every trigger timestamp for each SiPM-channel is recorded, the timing mode conserves storage and analysis time by logging only those channels that detect a signal exceeding the threshold within a designated trigger period. Besides the trigger moment, the temporal distance to this trigger—referred to as ToA—and the duration the signal surpasses the threshold (ToT) are also documented. Given the temporal resolution of 0.5 ns in this mode, and considering the cube’s dimensions (approximately 50 cm) alongside a muon’s near-light-speed velocity, a muon’s transit through the cube (max 1.5 ns) is well within the measurable range of this setup’s time resolution.

The flow chart is designed specifically for operation in this mode, making a distinction at the outset between events that either include or exclude a coincidence layer on both the right and left sides. For the purposes of this discussion, an "event" is defined as encompassing all ToA entries that occur within the same trigger period. It should be noted that *Janus* does not automatically sort the ToA timestamps, thus necessitating a thorough examination of the entire event.

In the section of the flow chart that addresses scenarios without a coincidence layer, each event is characterized by two ToA timestamps. Should any of these timestamps belong to a coincidence layer, the event is immediately disregarded, as it lacks a corresponding scintillator pixel that can be related to. Only when a compatible pixel pair (tuple) exists, does the analysis proceed to evaluate the ToA differences within this tuple. If these differences fall below a predefined coincidence time threshold, it is indicative of a particle having traversed one side of the cube.

The left part checks at first place, if a coincidence layer is in the event, else the event is discarded for this cube side. Afterwards the fitting side has to be checked for fitting tuples. If they are existing, the ToA difference has to be checked, if it is less or equal to the coincidence time. If there are multiple tuples in one side the event has to be discarded. A proper pixel allocation isn't possible, for example if there two particles pass one side of the cube, the coincidence layer and two four scintilator bars see a signal. As closer example side *E* and the bars 2, 4, 7 and 9 triggered. The pixels E27, E29, E47 and E49 are possible, so it is undecidable which two pixel of these four the particle passed. At least the ToA difference between the pixels and the coincidence layer has to compared to the coincidence time. If it is less, than there passed a particle this side.

In the flow chart's left section, the initial step involves verifying the presence of a coincidence layer within the event; its absence results in the event's exclusion for that particular side of the cube. Subsequent to this check, the analysis seeks to identify suitable pixel tuples. If such pairs are found, the next step is to examine the ToA differences within these tuples, ensuring they do not exceed the predefined coincidence time. Events featuring multiple tuples on one side are deemed inconclusive and therefore disregarded, as accurate pixel mapping becomes unfeasible. This scenario might occur, for instance, when two particles simultaneously traverse one side of the cube, activating the coincidence layer and several scintillator bars. Taking side *E* as an example, where bars 2, 4, 7, and 9 are activated, potential pixel combinations could include E27, E29, E47, and E49. In such cases, determining the precise path of the particles through these pixels is not possible. Finally, the ToA difference between the identified pixels and the coincidence layer is assessed against the coincidence time. A ToA difference within this threshold indicates a particle has traversed this side of the cube.

This procedure is required for every side of the cube. Afterward, the differences in Time of Arrival (ToA) across all channels need to be thoroughly examined. The coincidence timing for interactions involving two different sides of the cube is marginally greater than that for pixel pairs, being calculated based on the actual distance between two pixels. This meticulous step is crucial for a comprehensive analysis, facilitating precise event characterization and particle tracking throughout the cube.

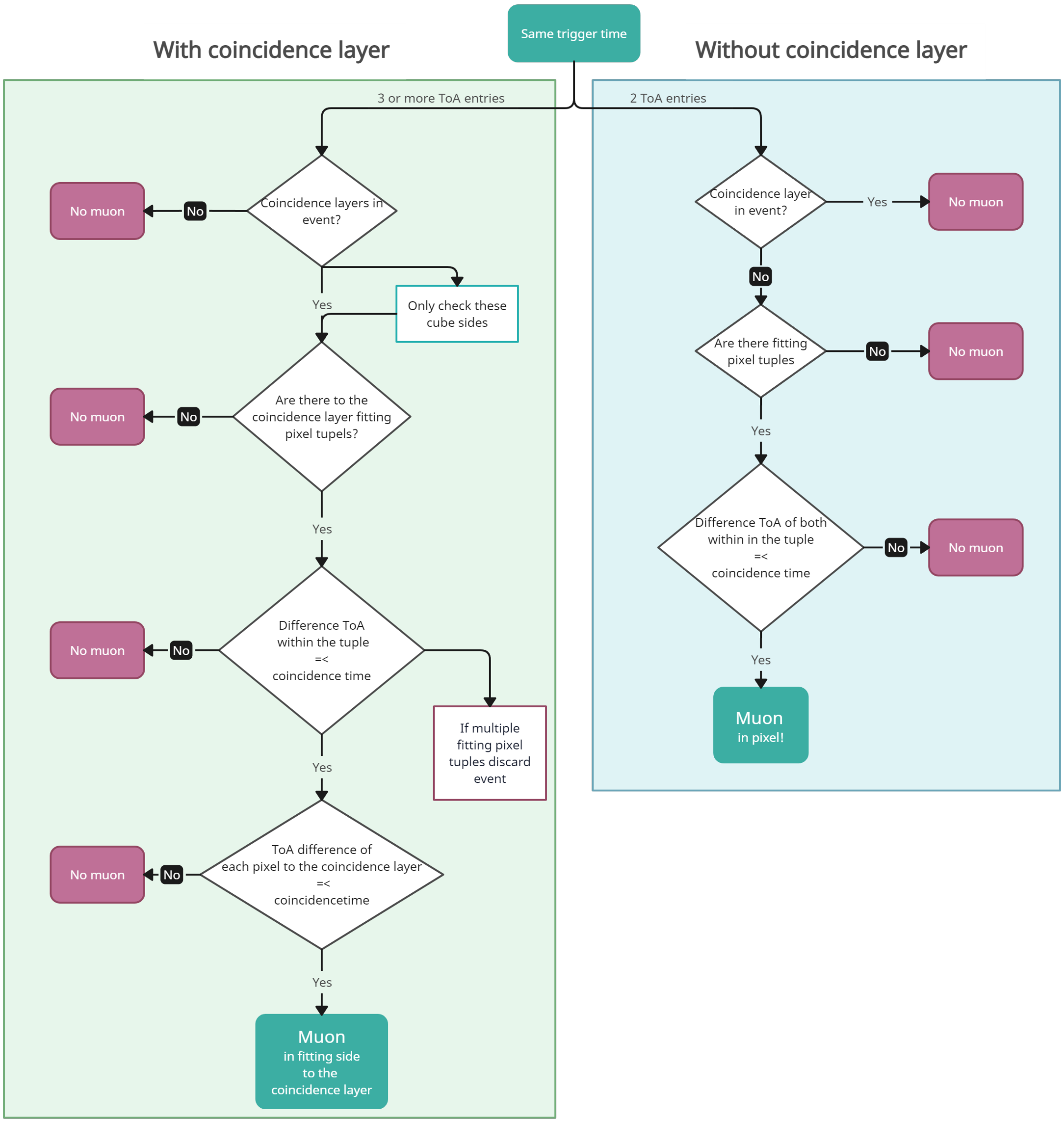

Figure 5.9.: Flowchart to decide if a muon passed the cube.

For events with multiple entries, the process involves determining the number of potential pixel pairs that have a time difference smaller than the established coincidence time. If an event on one side of the cube has several matching pairs, the entire event is disregarded. Similarly, events are discarded if they exhibit more than two sides with time differences smaller than the calculated coincidence time. An event is deemed valid only if it contains matching pairs with appropriate time differences. This criterion is applied regardless of whether the coincidence layer is involved. The primary distinction lies in the definition of matching pairs: for scenarios involving the coincidence layer, minimal three entries are required to form a valid tuple, whereas minimal two suffice in its absence. If tuples exist on different sides, the minimum ToA difference is assessed against the coincidence time. In cases where there are four tuples, and two pairs can be distinctly identified based on coincidence time, two angles are reconstructed, enhancing the precision of the analysis. For the initial measurements, to streamline the process, only tracks with distinct characteristics were reconstructed. Consequently, angles were reconstructed using pixel pairs with the coincidence layer included, exclusively with other pairs where the coincidence layer is also present. Similarly, reconstructions were made with pixel pairs without the coincidence layer, without mixing these two types of pairs. This approach simplifies the analysis for this thesis, although the integration of mixed pairs could be considered for future projects.

The code which realize this flow chart is described in the Appendix. With this reconstruction code the “MIP-Cube” data can be analysed for muon tracking.

## 5.3. MIP-Cube First Light

The measurements conducted with the "MIP-Cube" were performed without the lead shield, as mentioned in Chapter 4.2. The installation of the shield was not feasible due to time constraints and the absence of appropriately shaped lead.

### Heatmap

For the inaugural data collection with the "MIP-Cube", a five-minute data recording session was conducted, with a coincidence time of 1.5 ns between the pixel scintillators and 3.5 ns between the different sides. Additionally, for the subsequent measurements, no lead shielding will be employed for the stored optical fibers. To facilitate precise angle reconstruction, cube side *A* was manually oriented northward using a compass. The resultant data file, containing trigger times, ToA, and ToT, was processed using the Python code referenced in Chapter 5.2. Analysis of cube side *E*, which is illustrated in Figure 5.10, reveals it as the side most impacted by hits, likely due to its orientation parallel to the Earth's surface. Figure 5.10 presents contrasting heat maps generated from two analytical approaches: with and without the coincidence layer, adhering to the pixel numbering depicted in Figure 4.16b. A notable discrepancy in event counts is observed, with the total events for this side of the cube detailed in Figure 5.11. Exclusion of the coincidence layer yields a total of 1707 events, whereas its inclusion diminishes this figure to 634, roughly one-third. This reduction is also reflected in the heat map comparisons for this side, where the event count per pixel, considering the coincidence layer, markedly decreases in comparison to those without it. Supplementary analyses of the remaining cube sides are provided in the Appendix, demonstrating a reduced muon flux, as anticipated, with the coincidence layer similarly halving event counts. In summary, the incorporation of the coincidence layer significantly diminishes the event count per side, affirming its efficacy as a tool for verifying muon traversal through a particular cube side. This analysis, which concentrates on a single side, can be interpreted as detecting low energy particles that pass through the first two scintillator layers and are registered as an event, despite a background noise level exceeding theToT.

Figure 5.12 presents the heatmap from the 5-minute measurement incorporating the coincidence layer for each side of the cube, acting as independent detector, which is equipped with scintillators. This is represented as a quasi-geometrical cube net, similar to the schematic sketched in 4.16b, but with sides *B*, *C*, and *D* adjusted to an upright position. Every scintillator pixel is discernible, with a notably higher count observed on side *E*.

Figure 5.13a displays the number of muons traversing two distinct sides, reflecting the flux combinations these sides encounter over a 5-minute interval. The total number of events passed two sides is 120 with included coincidence layer. As anticipated, side *E* experiences a significantly higher muon flux. Given the steep angle of incoming muons, an increased flux from side *E* to sides *A* and *D* is expected due to the closer proximity of *E*'s scintillators to those on *A* and *D* than them of *B* and *C*, thereby increasing the

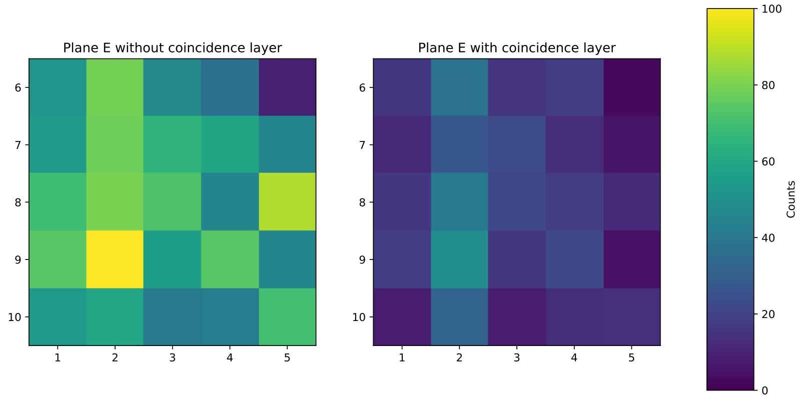

Figure 5.10.: Left: Heatmap depicting the distribution of counts per pixel on cube side *E* from a 5-minute measurement, without considering the coincidence layer. The pixel numbering corresponds to that shown in Figure 4.4b. Right: Heatmap of the same cube side *E*, this time with the coincidence layer included in the analysis, demonstrating the impact on event counts.

likelihood of scintillators on these side combinations being involved in a single event. Surprisingly, there is also a high flux to *E*, suggesting muons originate from the ground, which is plausible but unexpectedly frequent.

Figure 5.13b, depicting a similar analysis without the coincidence layer, recorded a total of 73 events, suggesting fewer events are omitted when an additional side is implicated, cumulatively resulting in 193 events. Mirroring the patterns in 5.13a, the flux from *E* remains the most substantial, with an increased flux from *E* to *A* and *D*. However, the flux to *E* is unexpectedly higher. This pattern persists in the combined flux analysis in 5.14.

The anomaly might be attributed to inaccuracies in data acquisition by the DT5202. Given the minimum time resolution of about 0.5 ns and the muon transit time through the cube of approximately 1.5 ns — close to the time resolution — timing discrepancies can arise. Another source of the unexpected anomaly could be, if a muon enters at the end of a scintillator bar farthest from the SiPM on one side and closer to the SiPM on the other side, the timestamp for the initial event may erroneously appear later than that for the subsequent event. Another possible source of this anomaly could be the not lead shielded optical fibers operate as detector. Consequently, in the analysis, the realistically later side may be misidentified as the first one. This could explain the higher observed flux from sides *A* and *D* to side *E*. The notably high flux observed from side *D* to side *E* might be attributed to the routing configuration for the coincidence layer and one pixel layer, which is directed over sides *E* and *B* towards the cube's base. Furthermore, the fibers originating from side *D* are positioned above those from side *E*. Consequently, this arrangement may lead to MIPs generated a signal in the fibers of side *D* prior to triggering a signal in the fibers of side *E*. This sequential signal generation could explain the observed flux pattern, highlighting the influence of fiber routing on the detection capabilities of the “MIP-Cube”. Additionally, the simultaneous arrival of two independent muons within the same time window, without traversing two sides, may result in misinterpretation.

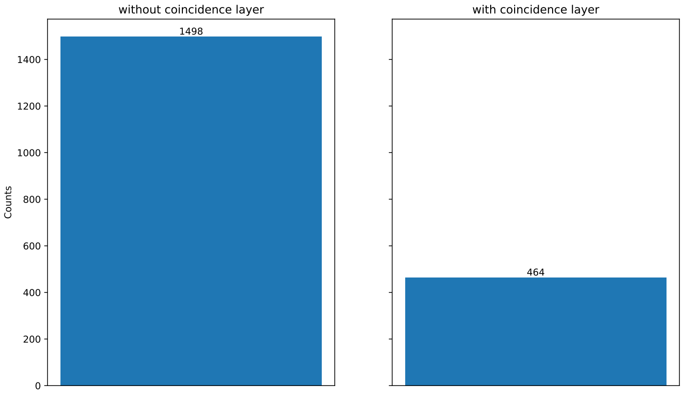

Figure 5.11.: Left: The number of events recorded during a 5-minute measurement employing the trigger logic depicted in Figure 4.1, without the implementation of a coincidence layer. Right: The number of events recorded under the same conditions but with the coincidence layer activated. Comparative analysis reveals that the coincidence layer effectively filters out more than one-third of the events for a given side.

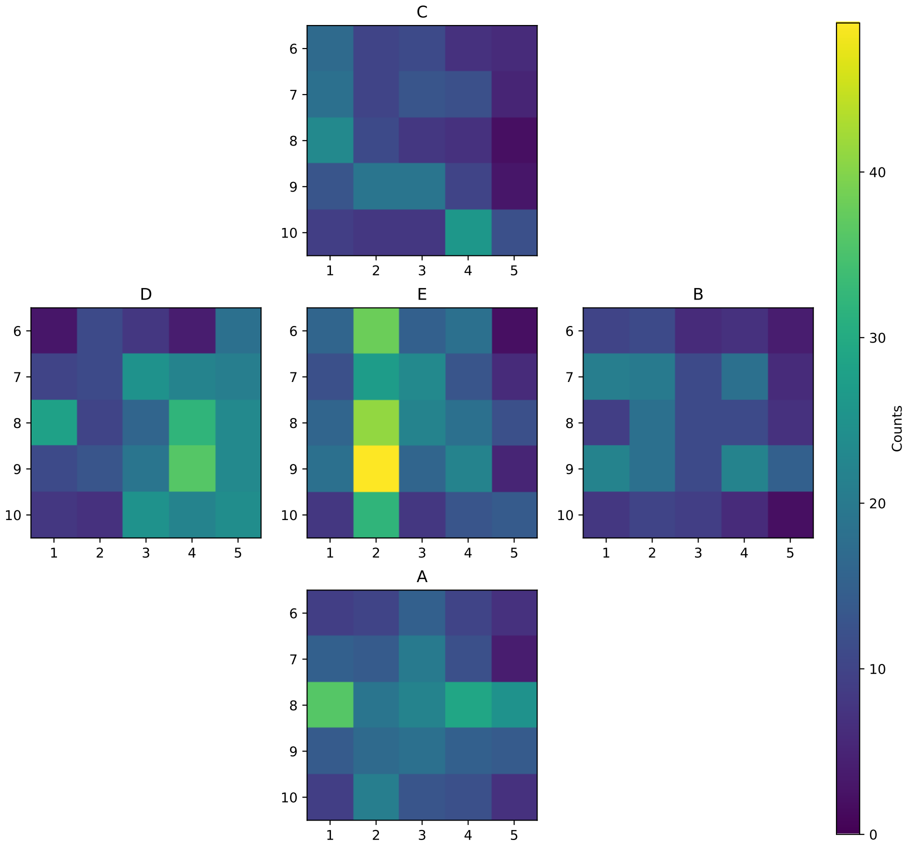

Figure 5.12.: The geometric net representing the heatmaps of every side of the cube incorporates the coincidence layer and features upright orientations for sides *B*, *C*, and *D*. Notably, an increased flux is observed on side *E*, indicating its higher exposure. Each side acts as independent detector.

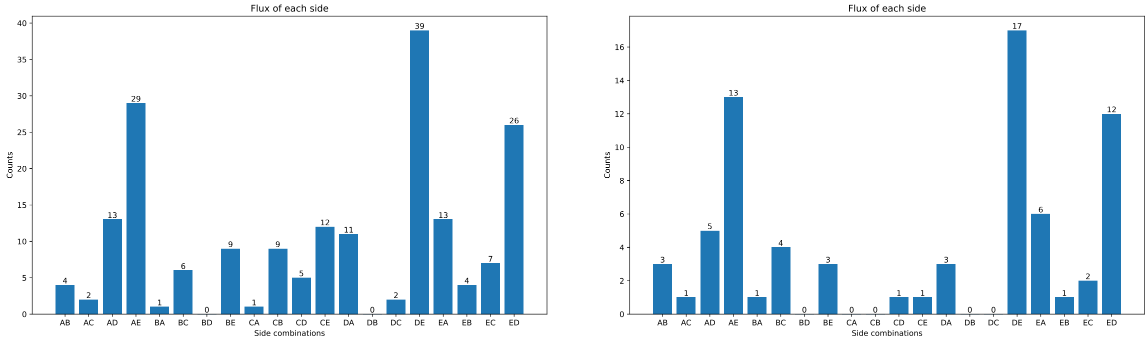

(a) (b)

Figure 5.13.: a) Muon flux recorded during a 5-minute interval across all possible two-side combinations with coincidence layer taken into account. b) Muon flux recorded during a 5-minute interval across all possible two-side combinations with coincidence layer **not** taken into account.

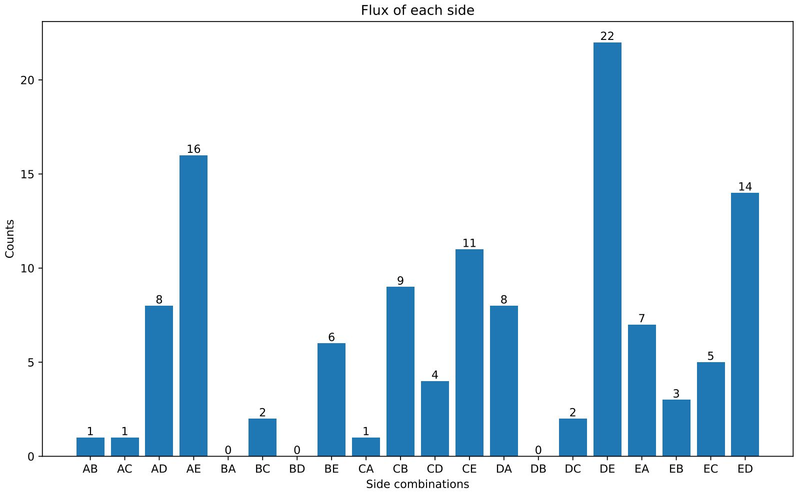

Figure 5.14.: Muon flux recorded during a 5-minute interval across all possible two-side combinations. Combined counts of with and without coincidence layer.

### Angle reconstruction

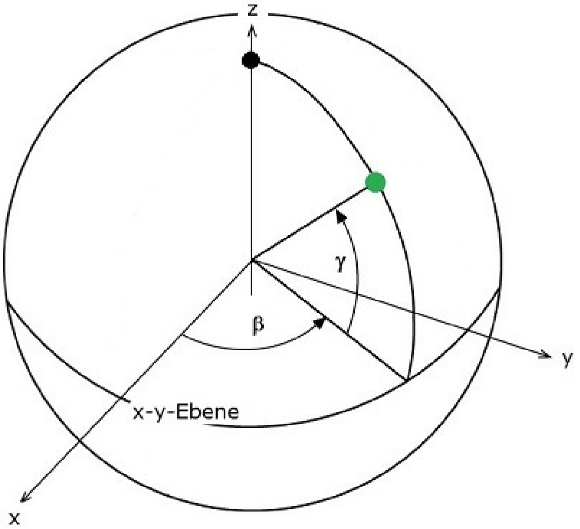

Figure 5.15.: Schematic depiction of the azimuth angle $\beta$ and altitude angles $\gamma$ [47].

To reconstruct the azimuth and altitude angles, it's crucial to know the precise positions of the scintillator pixels. The orientation of both angles are schematically illustrated in Figure 5.15. The focal point of a 3D pixel, with dimensions 50 mm x 50 mm x 20 mm, serves as the reference point for one pixel. When two pixels are activated simultaneously within the same trigger period, the azimuth angle ($\beta$) is calculated as follows:

$$\begin{aligned}
\beta &= \arctan\left(\frac{\Delta y}{\Delta x}\right), \text{ for } x > 0 \\
\beta &= \frac{\pi}{2} \cdot \operatorname{sgn}(\Delta y), \text{ for } x = 0 \\
\beta &= \arctan\left(\frac{\Delta y}{\Delta x}\right) + \pi, \text{ for } x < 0 \text{ and } y \geq 0 \\
\beta &= \arctan\left(\frac{\Delta y}{\Delta x}\right) - \pi, \text{ for } x < 0 \text{ and } y < 0
\end{aligned}$$

The altitude angle ($\gamma$) is determined by:

$$\gamma = \arctan\left(\frac{\Delta z}{\sqrt{\Delta x^2 + \Delta y^2}}\right)$$

where $\Delta x$, $\Delta y$ and $\Delta z$ represent the differences in positions between the two pixel points.

Given that each pixel point is considered representative of an entire pixel's area, a MIP passing through any part of the pixel is treated as if it traversed the designated pixel point.

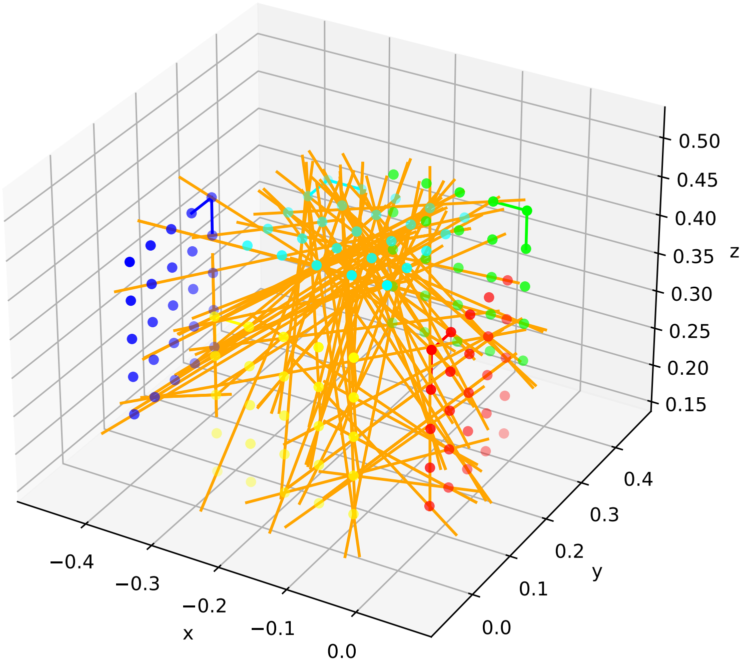

Figure 5.16.: 3D visualisation of the cube passing muons of a five minute measurement.

This approach necessitates incorporating a degree of uncertainty into the analysis, as the exact path of a MIP within the pixel cannot be precisely determined from its interaction with a single point. To account for this uncertainty, especially in calculating the azimuth angle, a Gaussian (Gauß) uncertainty calculation is employed. This statistical method provides a way to estimate the uncertainty associated with the assumption that a MIP's passage through any part of the pixel can be approximated by its crossing through the pixel point. The value is calculated with:

$$\sigma_\beta = \sqrt{\left(-\frac{\Delta y}{(\Delta x)^2 + (\Delta y)^2}\right)^2 \cdot (\sigma_{x_1}^2 + \sigma_{x_2}^2) + \left(\frac{\Delta x}{(\Delta x)^2 + (\Delta y)^2}\right)^2 \cdot (\sigma_{y_1}^2 + \sigma_{y_2}^2)}$$

The uncertainties $\sigma_{x_2}$, $\sigma_{x_1}$, $\sigma_{y_2}$ and $\sigma_{y_1}$ represent the variations in the x and y positions of the pixel points involved in the calculation. These uncertainties are crucial for accurately determining the position and thereby the angles associated with a MIP's path through the cube. The variability in these positions stems from several factors, including the physical attributes of the cube sides. A systematic uncertainty of 0.0005 m is attributed to all positions due to construction tolerances. For a cube side that is orthogonal to the x-axis, for example, there is an additional uncertainty of half a pixel's length (0.025 m) in both the y and z directions, accounting for the inherent imprecision in the pixel's placement.

With these uncertainties defined, the uncertainty in the azimuth angle can be similarly quantified. This approach ensures that the calculations of angles, crucial for determining the directionality of particles passing through the cube, incorporate the spatial imprecision inherent in the cube's design and construction. The uncertainty is given by:

$$\sigma_a = \sqrt{\left(\frac{\partial \gamma}{\partial x_2} \cdot \sigma_{\Delta x}\right)^2 + \left(\frac{\partial \gamma}{\partial y_2} \cdot \sigma_{\Delta y}\right)^2 + \left(\frac{\partial \gamma}{\partial z_2} \cdot \sigma_{\Delta z}\right)^2}$$

Prior to analyzing the 5-minute measurement, it's necessary to compute all potential angles and their frequencies. This analysis is depicted in Figure 5.17, showing that while azimuth angles are nearly uniformly distributed, some angles appear more frequently than others. An azimuth of 0° corresponds to north, with the cube side facing northward. For altitude angles, 0° is parallel to the Earth's surface, 90° aligns with the zenith, and -90° with the nadir as metioned in Figure 5.15. The absence of angles at 90° and -90° highlights the detection limitations for steep angles due to the cube's design, lacking scintillators at the bottom. This is a crucial disadvantage, because most cosmic ray muons will reach "MIP-Cube" in a steep angle. Also some other angles are not detectable. Based on these theoretical angles, a sky map is constructed, as shown in Figure 5.18. This corresponds to isotropic disturbed incoming rays. Understanding the theoretical angular distribution is instrumental in interpreting the measurement data and its significance.

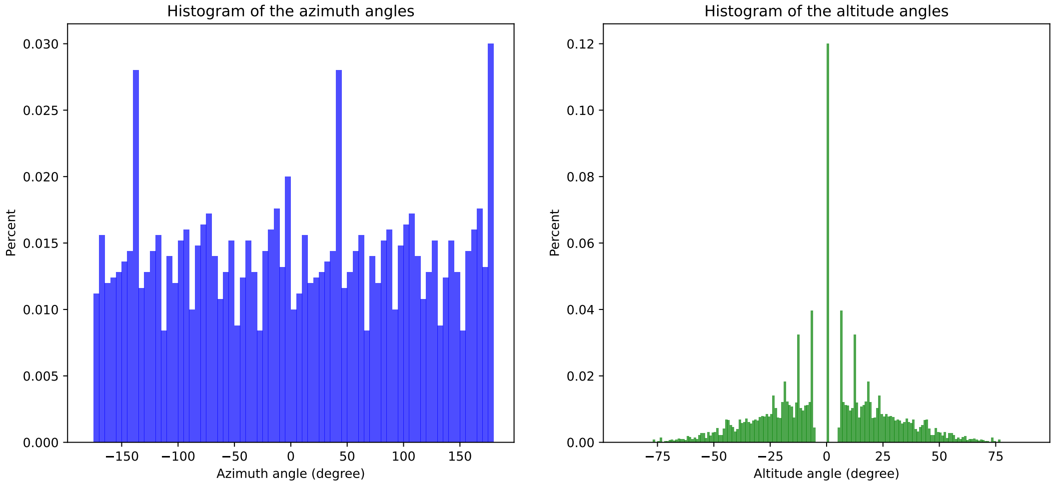

Figure 5.17.: Theoretically possible azimuth and altitude angles due to the cube's design with its pixel size of 50 mm x 50 mm x 20 mm. Left: The distribution of azimuth angles is nearly uniform, although certain angles appear more frequently; 0° denotes north, with the corresponding cube side facing northward. Right: The distribution of altitude angles, where 0° is parallel to the Earth's surface, 90° indicates the zenith, and -90° points to the nadir. The absence of measurements at 90° and -90° is attributed to the cube's design, specifically the lack of scintillators on the bottom, which precludes the detection of steep angles.

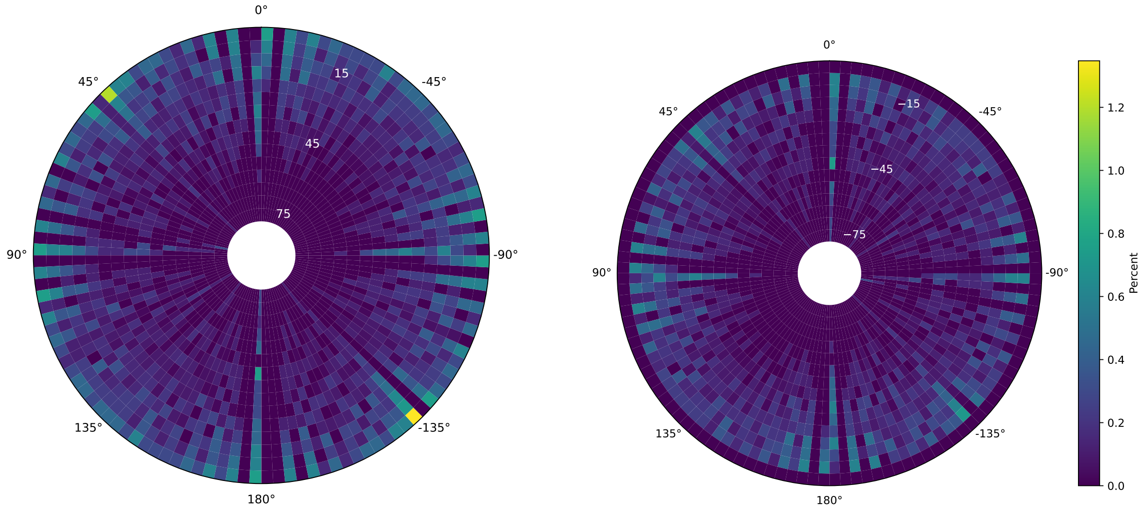

(a) (b)

Figure 5.18.: Theoretically possible azimuth and altitude angles due to the cube's design. a) Map of the sky for positive altitude angles. b) Map of the sky for negative altitude angles.

Figure 5.19 presents the angular distribution of azimuth and altitude angles from a 5-minute measurement conducted in the SPOCK laboratory. This diagram notably highlights the absence of extreme altitude angles at 90° and -90°, alongside a diminished presence of altitude angles around 0°. So a similar distribution as the theoretical angles for altitudes n Figure 5.17 can be seen. No distinct pattern is observed within the azimuth angles. The figure compares events with and without the coincidence layer, revealing similar distributions for both scenarios. This observation suggests that the coincidence layer's impact on angle reconstruction may be minimal.

For the sky map depicted in Figure 5.20 similarly as in Figure 5.19 a significant occurrence of negative altitude angles are visible. This is related to the flux discussed with Figure 5.14 and has as similar explanation. Also both plots, at a maximal number of counts of nine for the skymap (Figure 5.20), a significant structure can't be detected. Potentially it could may intend a flux from left (west) top side. To verify this an extended exposure time is necessary. Figure 5.16 presents a three-dimensional visualization of this measurement. However, for datasets containing a larger number of events, this visualization approach may not be ideal due to potential overcrowding in the graphical representation. Nevertheless, even with lower statistics, this could be a suitable visualisation for identifying an absorber within the cube.

In conclusion, this measurement confirms that the cube functions as intended; however, several aspects remain unclear, necessitating further calibration. Additionally, enhancing our understanding of the DT5202 could significantly improve the device's capacity for optimal reconstruction. As a proof-of-principle experiment, the cube has demonstrated its viability.

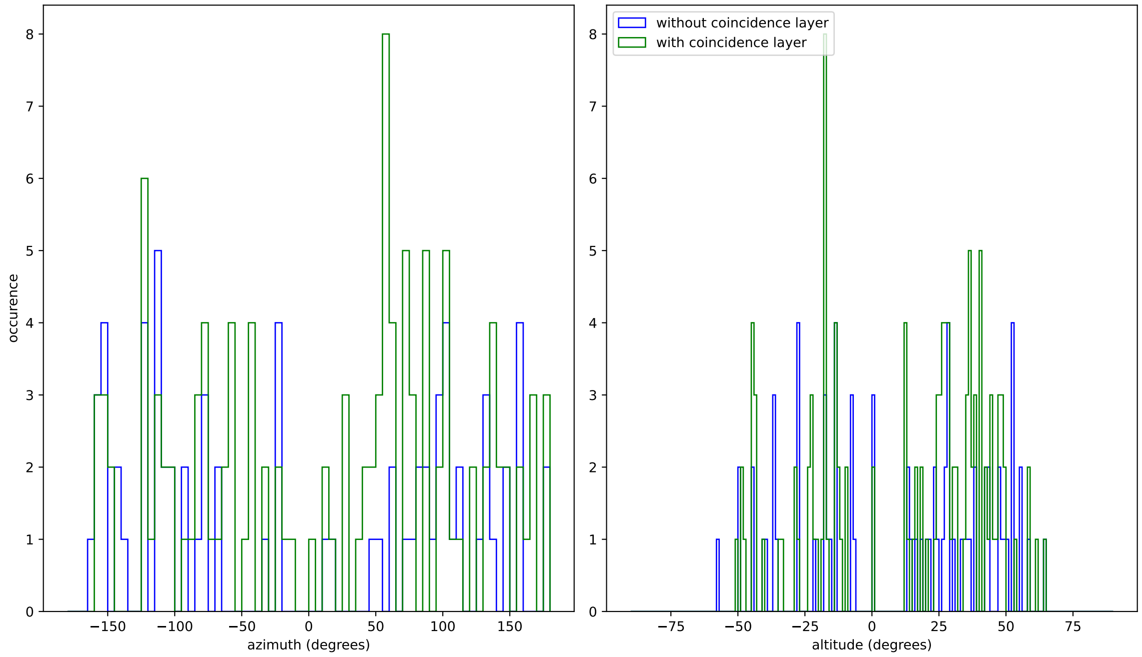

Figure 5.19.: Reconstructed azimuth and altitude angulars for a 5-minutes measurement. For comparison, the events with and without coincidence layer are shown.

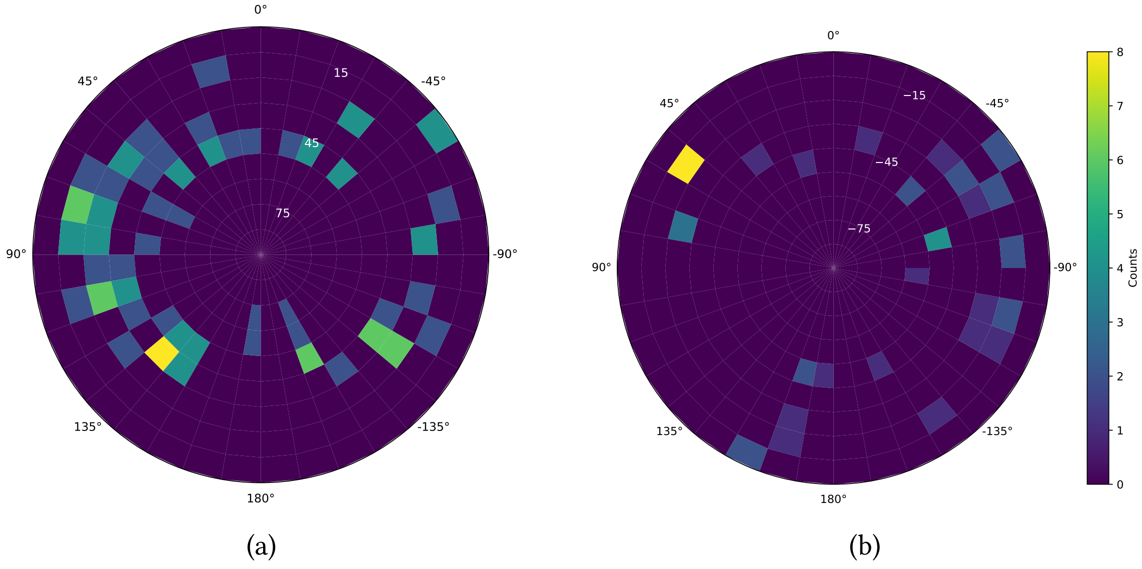

(a)

(b)

Figure 5.20.: Measured angular distribution from the 5-minute measurement session. No discernible structure was detected, indicating that additional data is required for a conclusive analysis.

## 5.4. Operational Functionality Test

### One hour heatmap

After the first light a one-hour measurement was conducted in order to investigate deeper the functionality. This results for side *E* in a total number of 21811 reconstructed events, 16951 without and 4860 with coincidence layer. Accordingly, the same analyses as described above were applied. The results, including the heatmaps (Figure 5.21), the analysis comparing the presence and absence of the coincidence layer (Figure 5.22), the heatmaps for each cube side with the coincidence layer (Figure 5.23), and the plots depicting each possible side-to-side flux (Figures 5.24 and 5.25), corroborate the findings reported in Chapter 5.3. The total number reconstructed angles is 929, 436 without and 439 with coincidence layer. Notably, the flux plots continue to show a significant flux originating from the ground towards side *E*, suggesting a potential systematic issue, where it is under if it is based on a technological issue of “MIP-Cube” or the DAQ and reconstruction. This needs to be further investigated, which was not possible within the frame of this thesis.

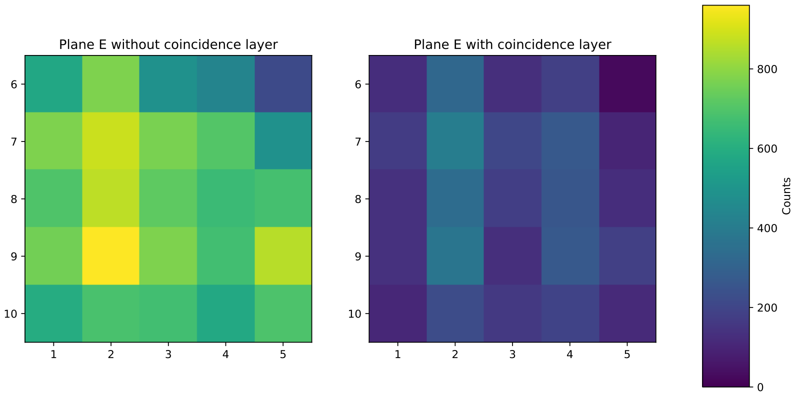

Figure 5.21.: Left: Heatmap depicting the distribution of counts per pixel on cube side *E* from a 1-hour measurement, without considering the coincidence layer. The pixel numbering corresponds to that shown in Figure 4.4b. Right: Heatmap of the same cube side *E*, this time with the coincidence layer included in the analysis, demonstrating the impact on event counts.

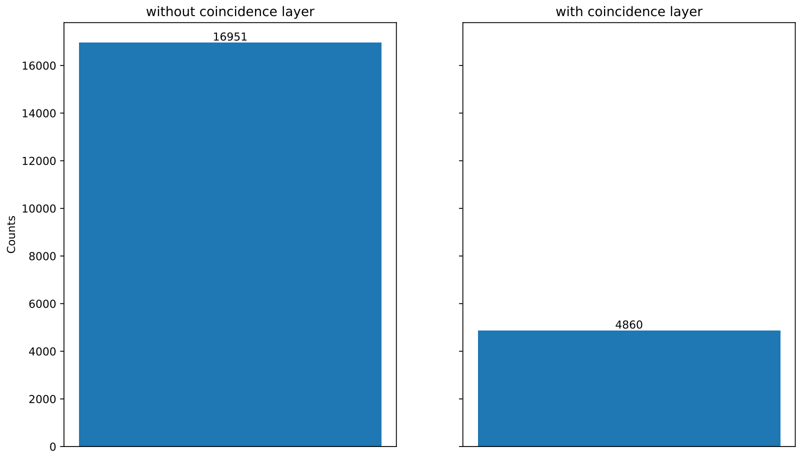

Figure 5.22.: Left: The number of events side *E* recorded during a 1 hour measurement employing the trigger logic depicted in Figure 4.1, without the implementation of a coincidence layer. Right: The number of events recorded under the same conditions but with the coincidence layer activated. Comparative analysis reveals that the coincidence layer effectively filters out more than one-third of the events for a given side.

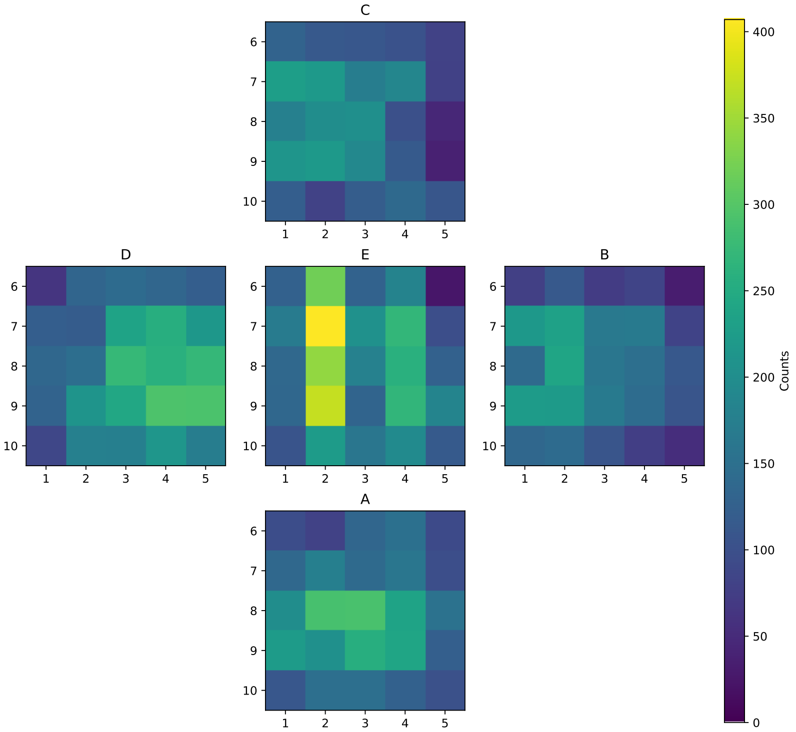

Figure 5.23.: The geometric net representing the heatmaps of each side of the cube for a one-hour measurement incorporates the coincidence layer and features upright orientations for sides *B*, *C*, and *D*. Each side acts as independent detector. Notably, an increased flux is observed on side *E*, indicating its higher exposure.

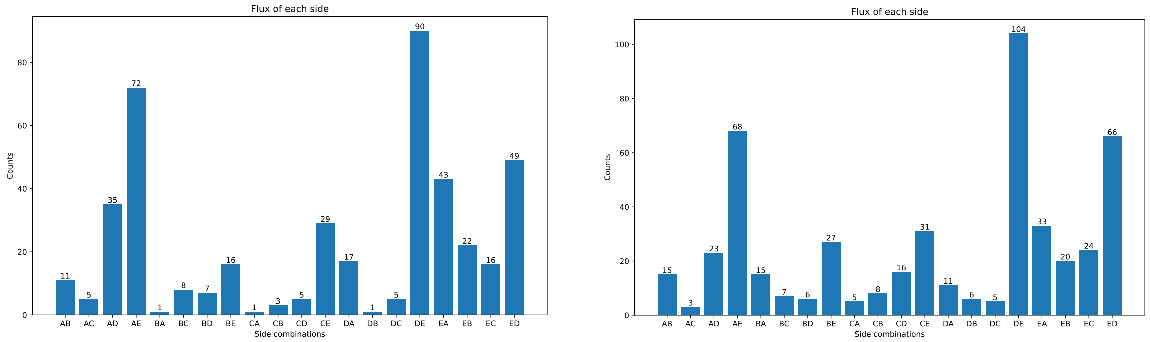

(a) (b)

Figure 5.24.: a) Muon flux recorded during a one-hour interval across all possible two-side combinations with coincidence layer not taken into account. b) Muon flux recorded during a one-minute interval across all possible two-side combinations with coincidence layer not taken into account.

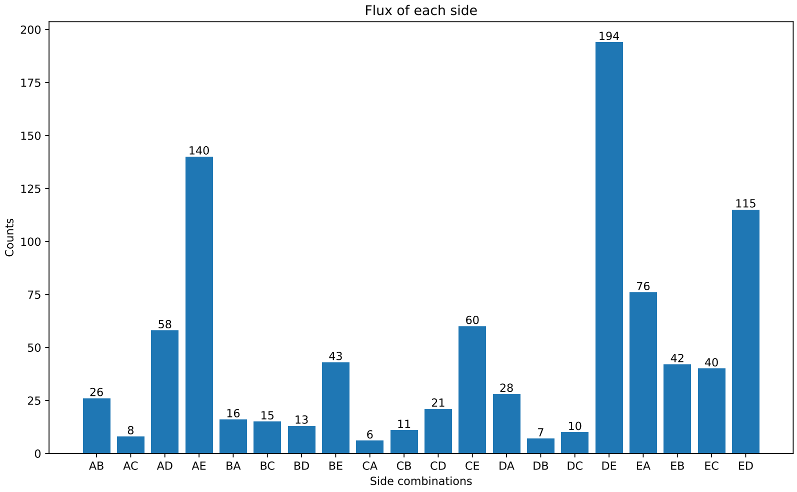

Figure 5.25.: Muon flux recorded during a one hour interval across all possible two-side combinations. Combined counts of with and without coincidence layer.

## Angle reconstruction

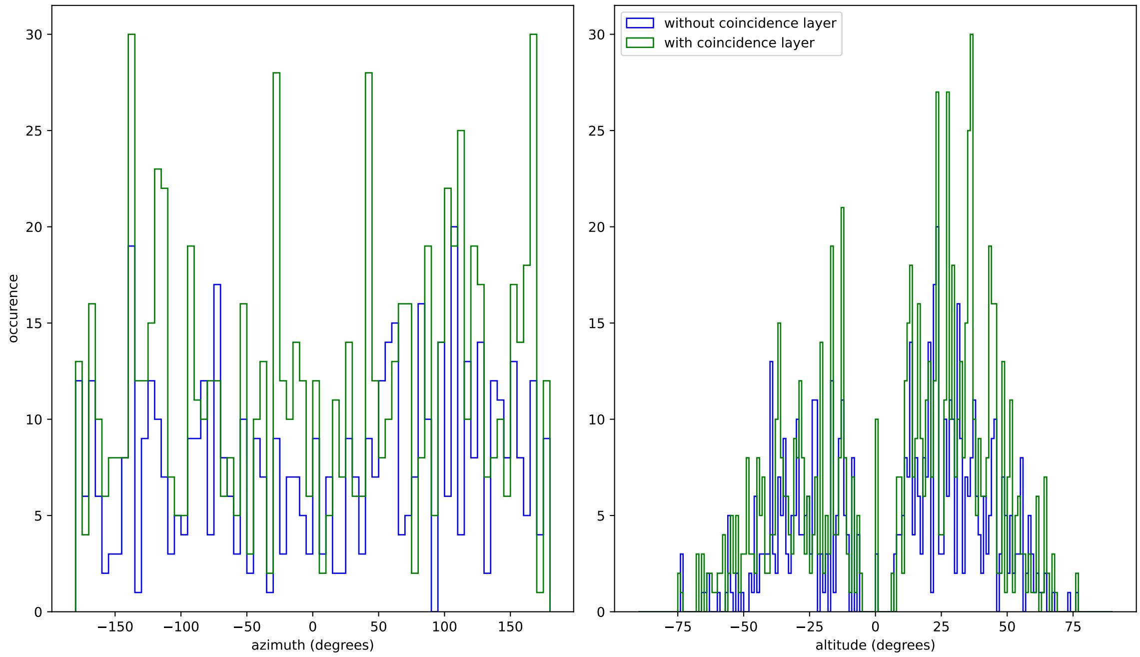

Figure 5.26.: Reconstructed azimuth (left) and altitude (right) angulars for a one hour measurement. Shown are the events with and without coincidence layer.

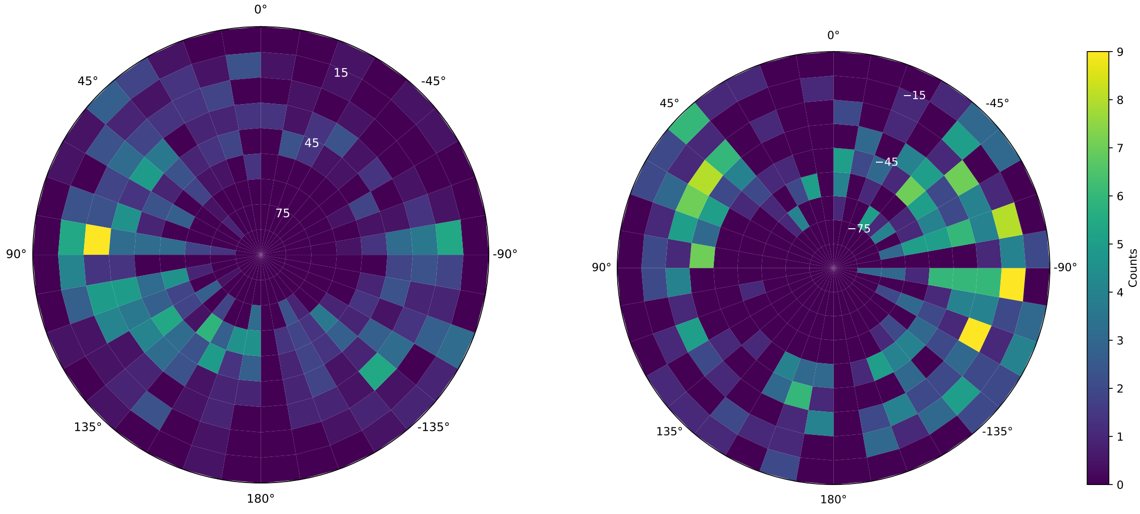

(a)

(b)

Figure 5.27.: Measured angular distribution from the one hour measurement session. a) Positive altitude angles are depicted. b) Negative altitude angles are shown. No discernible structure was detected, indicating that additional data is required for a conclusive analysis. A tendency can be seen for flux from the west side.

Figure 5.26 reveals a more defined structure compared to Figure 5.19, aligning with theoretical predictions. Specifically, the altitude angles exhibit two maxima around ±20°, and the azimuth angle distribution appears more uniform. This observation further corroborates the hypothesis presented in Chapter 5.3 regarding the similarity in event behavior, regardless of the coincidence layer's presence in angle reconstruction. Additionally, it highlights the heatmap of a single side and its notable decrease in muon counts.

The sky map presented in Figure 5.27 also displays more discernible structure, particularly evident from the flux from top (Figure 5.27a), suggesting a directional pattern from an azimuth angle of 45° to 180°. In addition to the previously noted patterns, an observed flux from the bottom to the top, spanning azimuth angles from about -10° to -90° (Figure 5.27b), indicates activity on the opposite side azimuth angles as in Figure 5.27a. This observation, in conjunction with the hypothesis that events seemingly originating from the ground, i.e. lower horizon from point of view of the "MIP-Cube" plane, are incorrectly identified and are instead attributable to cosmic rays, suggests a potential for increased flux from the south-west direction. However, with a maximum count of nine, this pattern does not reach statistical significance. Consequently, it is recommended to undertake more extensive measurements for a more conclusive analysis.

In conclusion the operational functionality of "MIP-Cube" is given, with the confirmation of first light measurement findings. The prototype is ready to be improved and to apply for further applications

## 5.5. Long Term Measurement

A potential hardware concern identified was the routing of fibers over the top side *E* for side *D*. To address this, three lead blocks with dimensions of 10 cm x 10 cm x 5 cm were positioned over the fibers' top routing to mitigate the impact of MIPs directly hitting the fiber. This method of shielding differs from the discussed in the chapters above. Unlike the shield inside the cube framethis one it is placed on top. Following this adjustment, the SiPMs were recalibrated. Conducting a more extensive 24-hour measurement inside the SPOCK while employing the same analytical methods described in the preceding chapters has yielded a total of 31640 reconstructed angles. Of these, 12964 were detected with the coincidence layer active, and 18676 angles were reconstructed without it. For side *E* the number of valid events is reduced from 437115 without the coincidence layer to 138561 with it. Similar to observations from the one-hour measurement, the patterns and findings discussed in both previous chapters become more pronounced and evident through this extended analysis.

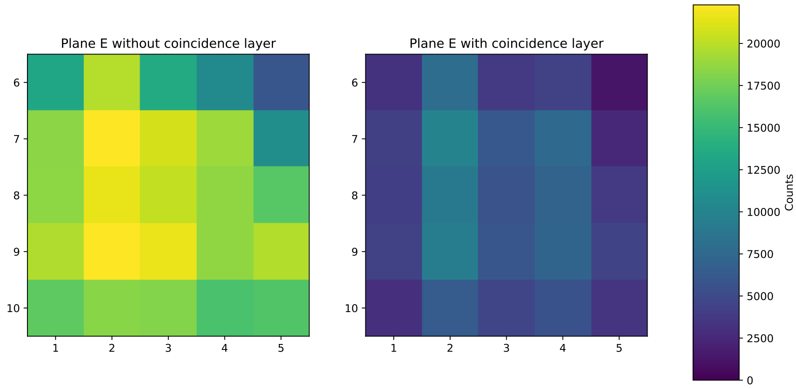

Figure 5.28.: Left: Heatmap depicting the distribution of counts per pixel on cube side *E* from a 24-hour measurement, without considering the coincidence layer. The pixel numbering corresponds to that shown in Figure 4.4b. Right: Heatmap of the same cube side *E*, this time with the coincidence layer included in the analysis, demonstrating the impact on event counts.

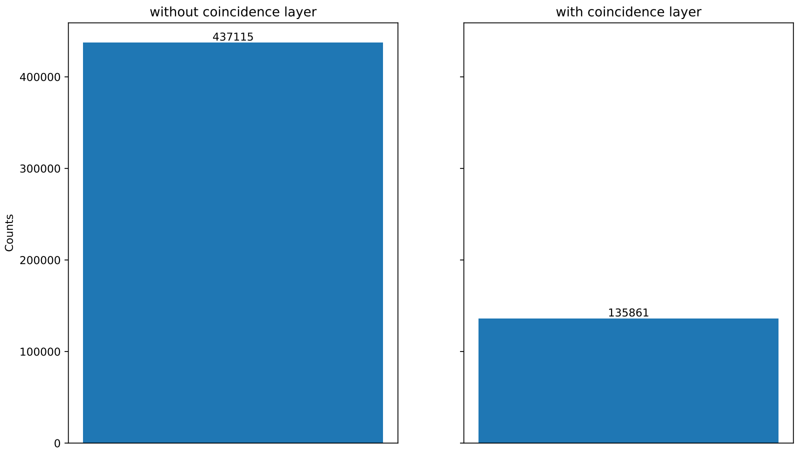

Figure 5.29.: Left: The number of events in side *E* recorded during a 24-hour measurement employing the trigger logic depicted in Figure 4.1, without the implementation of a coincidence layer. Right: The number of events recorded under the same conditions but with the coincidence layer activated. Comparative analysis reveals that the coincidence layer effectively filters out more than one-third of the events for a given side.

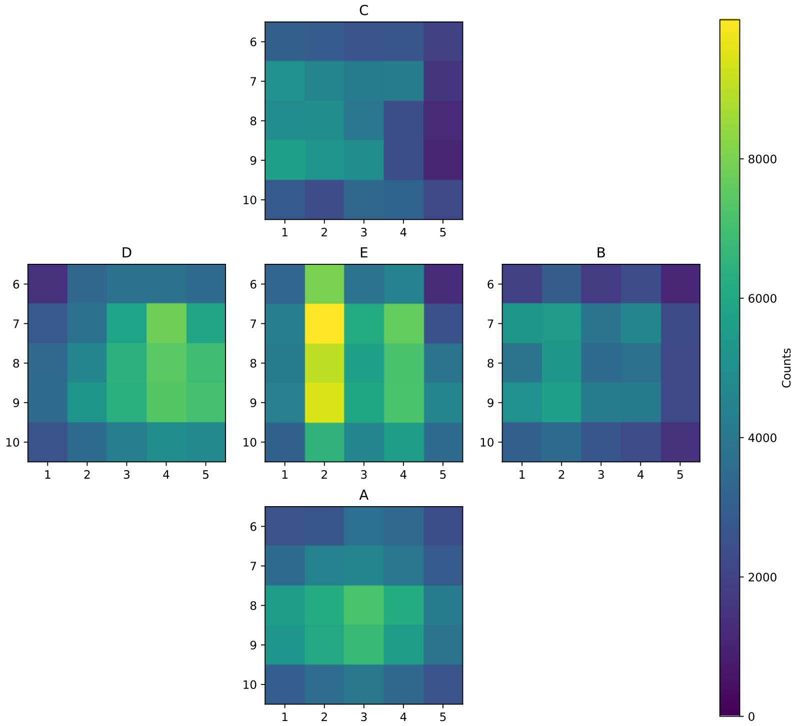

Figure 5.30.: The geometric net representing the cube heatmap for a 24-hour measurement incorporates the coincidence layer and features upright orientations for sides *B*, *C*, and *D*. Notably, an increased flux is observed on side *E*, indicating its higher exposure. Each side acts as individual detector.

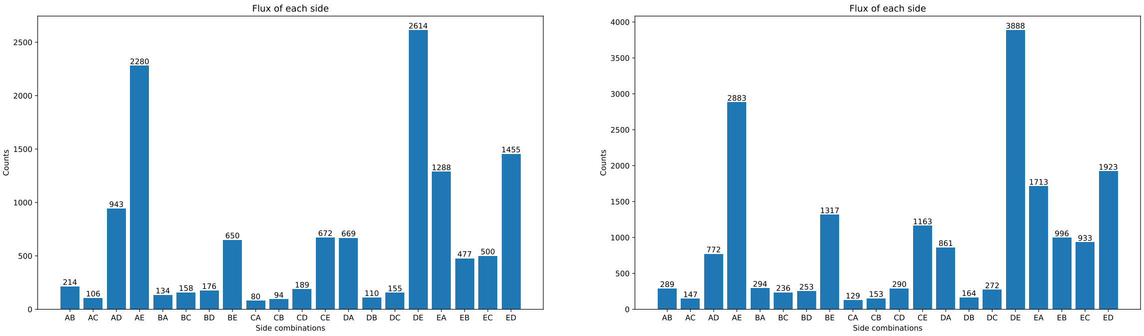

(a) (b)

Figure 5.31.: a) Muon flux recorded during a 24-hour interval across all possible two-side combinations with coincidence layer not taken into account. b) Muon flux recorded during a 5-minute interval across all possible two-side combinations with coincidence layer not taken into account.

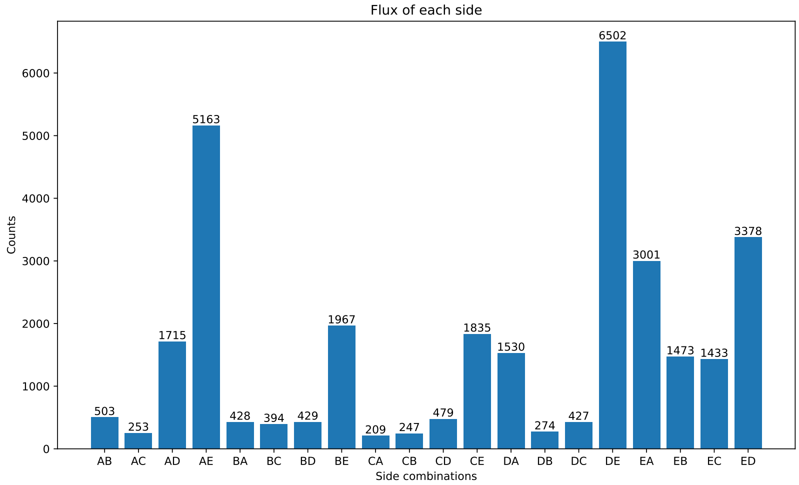

Figure 5.32.: Muon flux recorded during a one hour interval across all possible two-side combinations. Combined counts of with and without coincidence layer.

## Long term measurement angle reconstruction

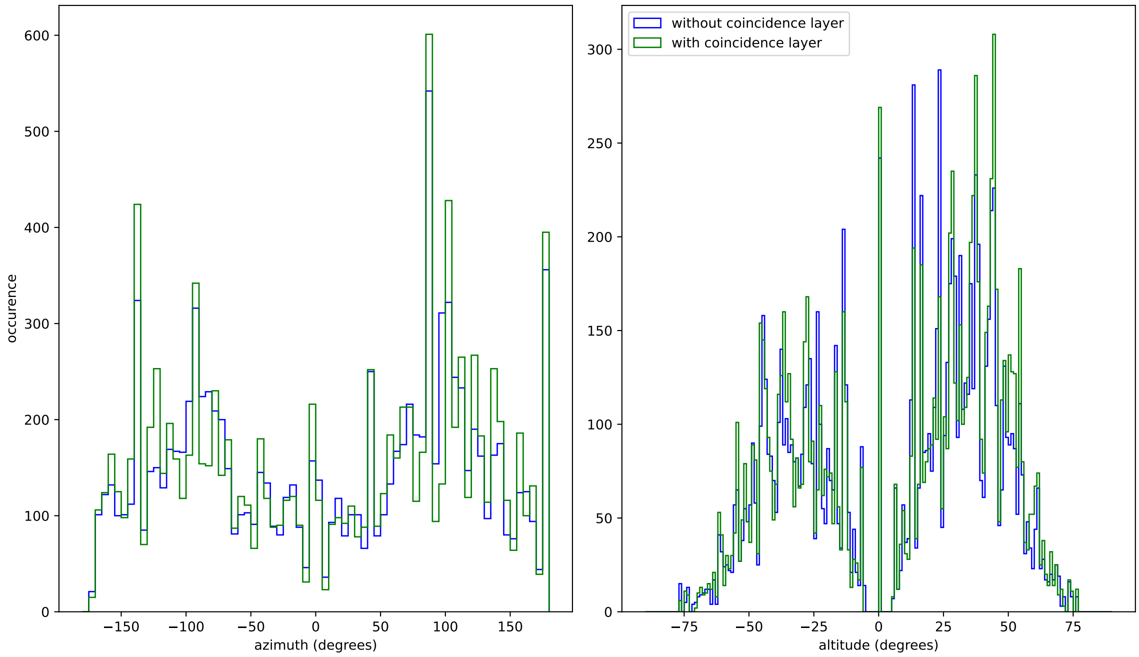

Figure 5.33.: Reconstructed azimuth and altitude angulars for a 24 hour measurement. Events with and without hitted coincidence layers are shown.

The sky map illustrated in Figure 5.34 indicates an increased flux between azimuth angles of 45° to 180° and altitude angles around 45°, as well as a notable flux from 0° to -135° in altitude angles. Echoing the assumptions made in the preceding chapter, these observations once again suggest a predominant flux originating from the south-west direction. Contrary to expectations of a uniform flux across all azimuth angles with a preference for steep altitude angles, the observed pattern suggests a possible deflection of muons prior to their detection by the “MIP-Cube”.

This discrepancy may stem from the geometric characteristics of the “MIP-Cube”. Specifically, sides *A* and *D* are positioned closer to side *E*, as depicted in a top view of the “MIP-Cube” without the mounted side *E* (Figure 5.35). Consequently, the “MIP-Cube” possesses an enhanced capability for measuring steeper altitude angles on these sides, correlating with an increased muon detection rate at these steeper angles. This geometric relationship directly impacts the sky map and the angles detected. Side *A* is faced north so side *D* faces east, so a higher number of events could be measured from west and south. To further understand this effect, a supplementary simulation that assigns greater importance to steeper angles could be conducted, potentially offering more insight into the influence of the cube’s geometry on the detection patterns observed.

For the simulation a weighting of incoming muons of an angle from 90° down to 15°. With a weighting of factor 7 the altitude distribution in Figure 5.36 looks very similar to the measured one in Figure 5.33. Nevertheless the theoretical sky map shown in Figure 5.37 and the measured one differences significant.

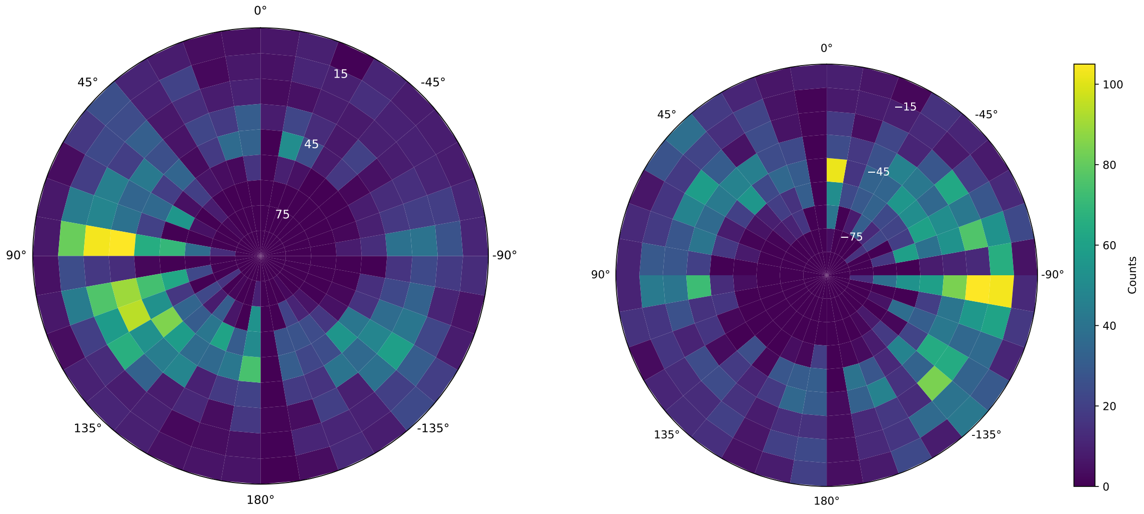

(a)

(b)

Figure 5.34.: Measured angular distribution from the 24 hour measurement session. a) Positive altitude angles with a visible flux origin above the “MIP-Cube” horizon. Which intends a arriving muons from top west direction. b) Negative altitude angles with a visible flux origin below the horizon. Which intends a arriving muons from bottom east direction.

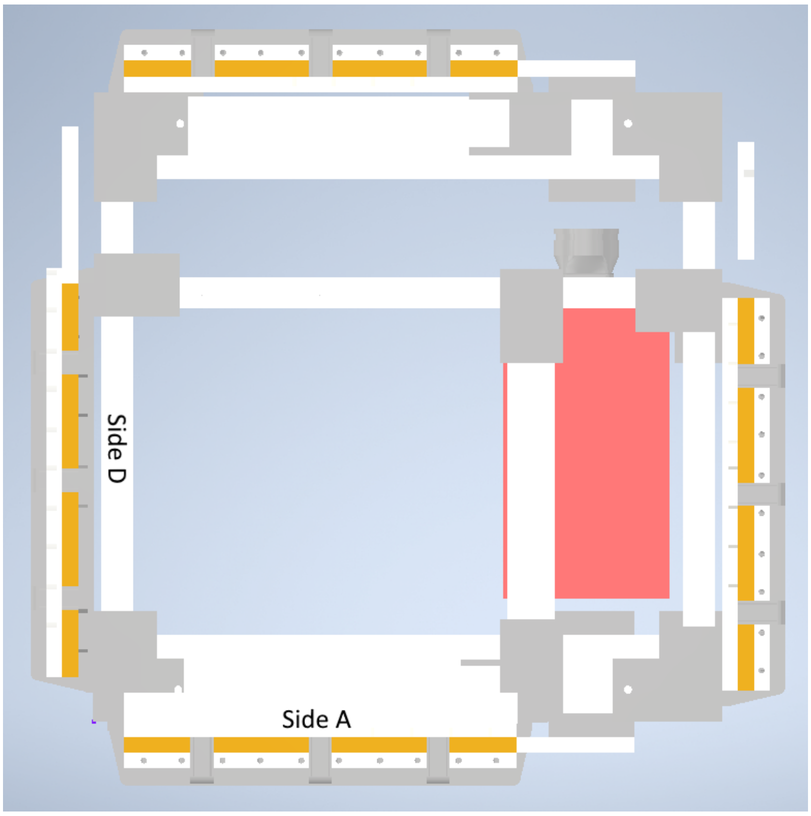

Figure 5.35.: Top view on “MIP-Cube”. Side E is demounted. Side *A* and *D* are marked. At the bottom the DT5202 (red) is visible with the mounted coupling system.

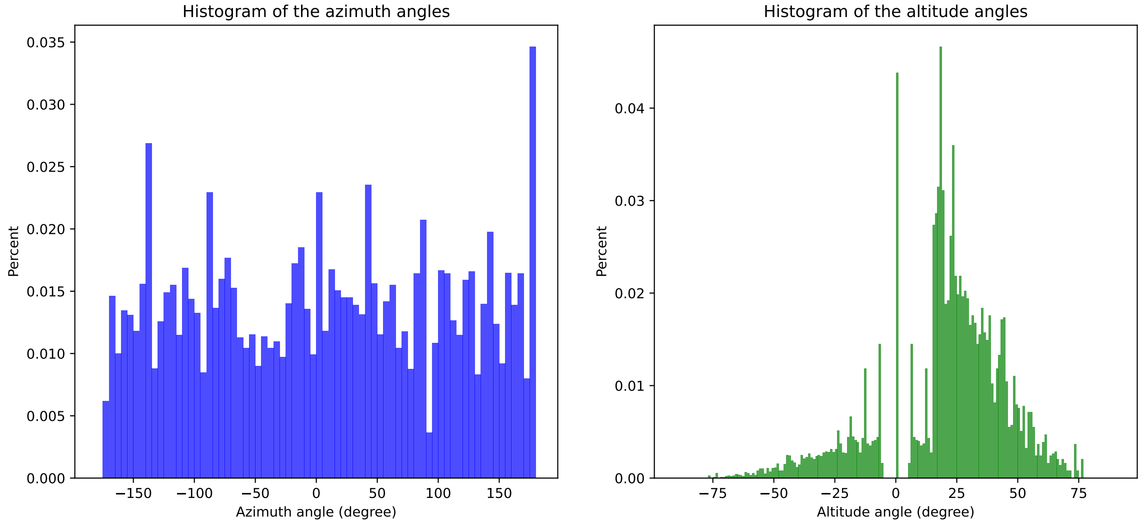

Figure 5.36.: Theoretically possible azimuth and altitude angles due to the cube's design, with an weighting of the incoming MIPs of deep altitude angles of 90° to 15° by factor 7. Left: The distribution of azimuth angles is nearly uniform, although certain angles appear more frequently; 0° denotes north, with the corresponding cube side facing northward. Right: The distribution of altitude angles, where 0° is parallel to the Earth's surface, 90° indicates the zenith, and -90° points to the nadir.

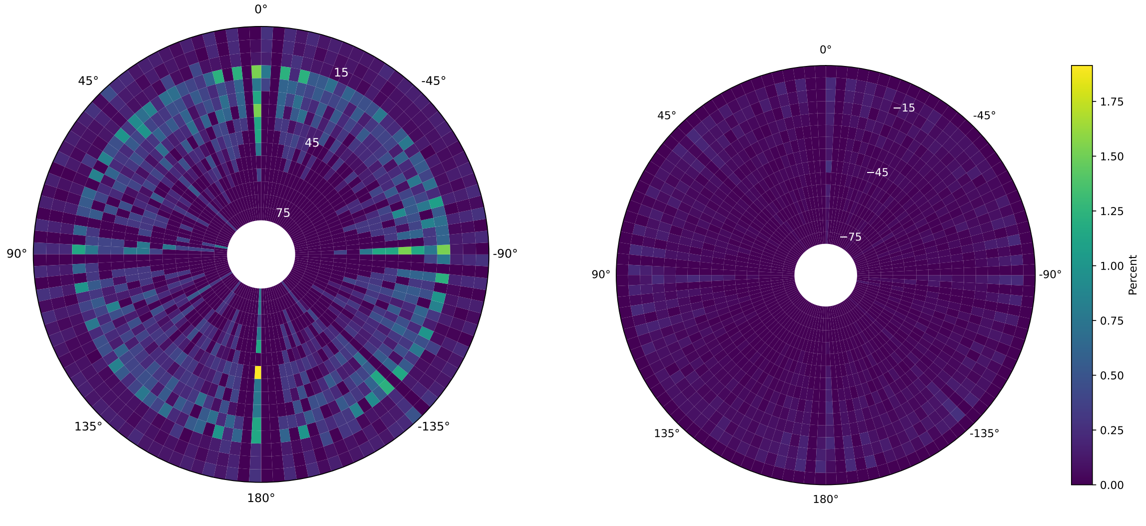

(a) (b)

Figure 5.37.: Theoretically possible azimuth and altitude angles due to the cube's design, with a weigthing of the altitude angles of 90° to 15° with factor 4. a) Map of the sky for positive altitude angles. b) Map of the sky for negative altitude angles.

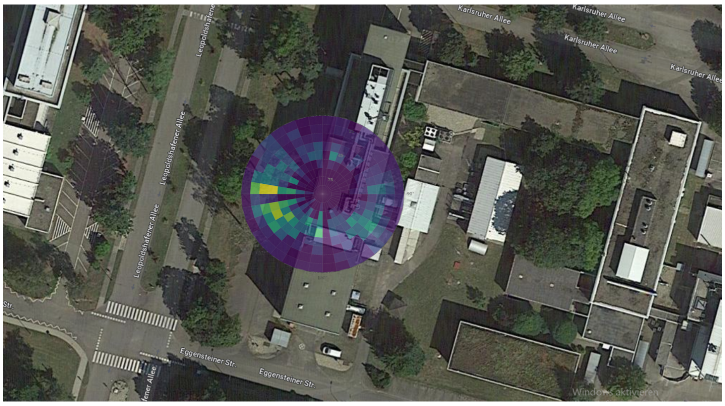

Figure 5.38.: Overlapping the reconstructed sky map with positive altitude angles with a google maps picture of the Institute for Astro Particles (IAP) building. To check the assumption "MIP-Cube" is able to measure the building distracts muons.

The higher flux has other sources. One possibility could be attributed to the structure housing of the SPOCK laboratory. To further investigate this hypothesis, an overlay of the sky map and the laboratory's building layout is provided in Figure 5.34, aiming to correlate the observed muon flux patterns with potential architectural obstructions. To explore the potential influence of the laboratory's building on the observed muon flux patterns, Figure 5.38 present an overlaid image of the sky map with the building's layout. This visual comparison offers a plausible explanation for the detected flux trends. To validate this hypothesis, it is proposed that the "MIP-Cube" be slightly rotated away from its original northward orientation. Should the flux direction remain unchanged post-rotation, it would serve as compelling evidence that the "MIP-Cube" is capable of detecting muon deflections caused by the building's structure.

### Rotation of the cube

To investigate if the observed higher flux from the southwest was influenced by the building's structure, the "MIP-Cube" was rotated 180 degrees to face side *A* southward. This rotation aimed to test whether the building's presence with adjusted analysis could be causing a reduction in flux with constant direction from the northeast. Over the course of a 24-hour measurement, the results, displayed in Figures 5.39 and 5.40, revealed that the flux direction did shift to the northeast as might not have been expected if the building were influencing the flux pattern. This observation contradicts theoretical expectations, even when considering weighted altitude angles as shown in Figure 5.37, indicating an additional hardware issue might be at play. i.e. the "MIP-Cube behaves not symmetrical in the muon-tracking sensivity.

This experiment indicates that while the building may influence the flux direction significant, hardware configurations and protective measures like lead shielding play a crucial role in the cube's detection capabilities and the accuracy of recorded data.

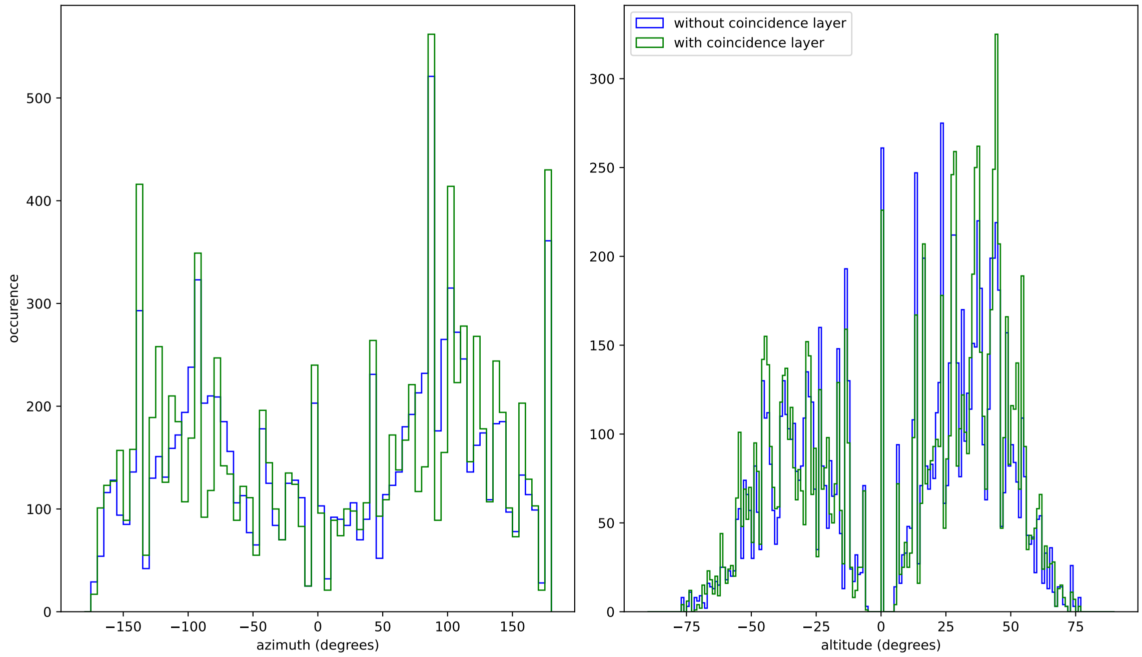

Figure 5.39.: Reconstructed azimuth and altitude angulars for a 24 hour measurement. In comprehension the events with and without coincidence layer. Where the "MIP-Cube" is rotated to the South.

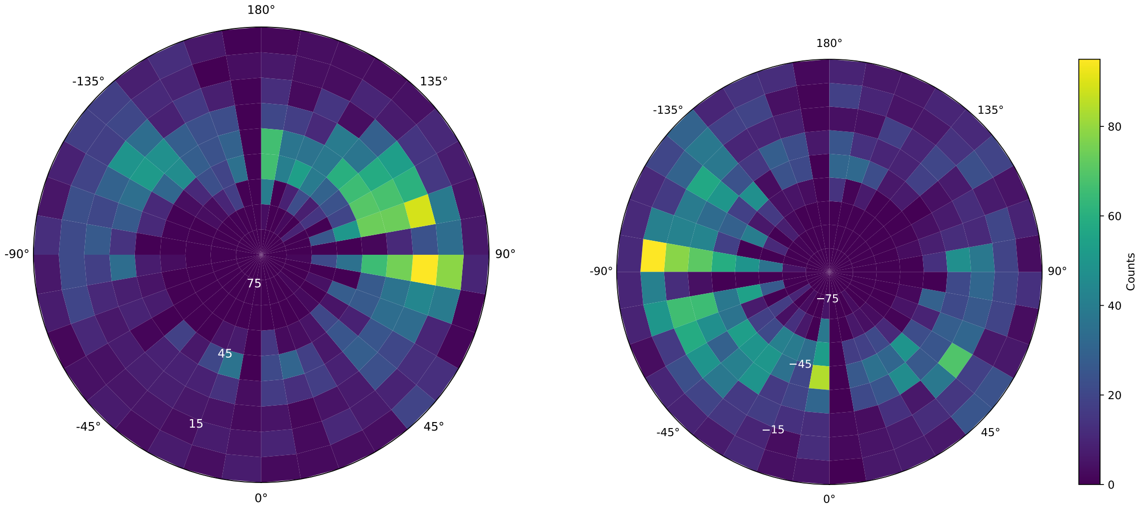

(a)

(b)

Figure 5.40.: Measured angular distribution from the 24 hour measurement session. With rotated "MIP-Cube" to the South. a) Positive altitude angles. b) Negative altitude angles. The flux turned with the turn of the cube which indicates a hardware characteristic.

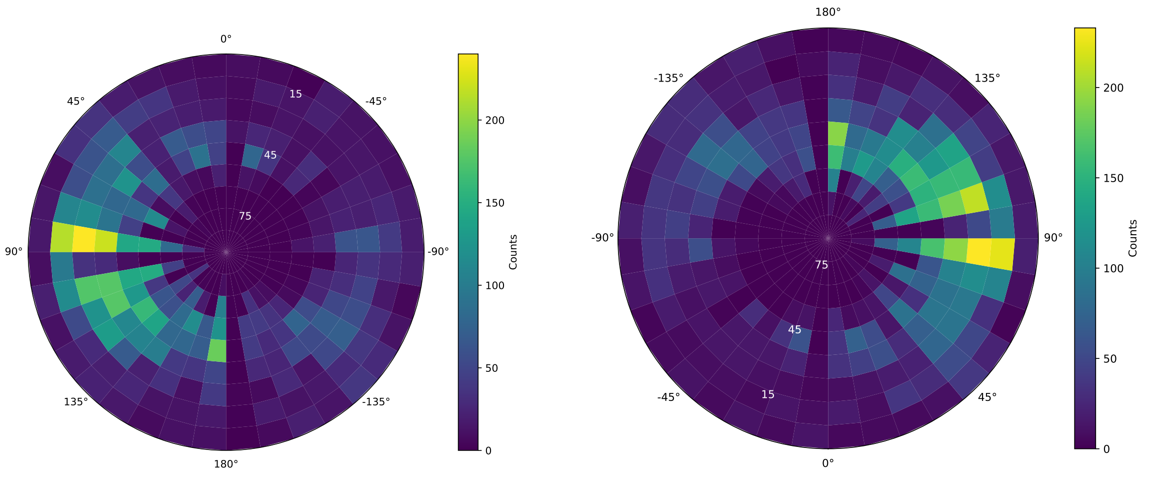

(a) (b)

Figure 5.41.: a) This figure presents the results from a 24-hour measurement with the "MIP-Cube" oriented to the North, including the amounts of altitude angles. Azimuth angles associated with negative altitude angles have been rotated by 180 degrees to correct their orientation. b) The data of the 24 hour measurement, during which "MIP-Cube" rotated to face South, the figure similarly shows the amount of altitude angles with azimuth angles corresponding to negative altitudes adjusted by a 180-degree rotation. An increasing flux at side *D* (See Fig. 5.35) of the cube is visible.

The sky map depicted in Figure 5.41 aggregates data from both 24-hour measurement sessions, adjusting the counts by adding the number of events with negative altitude angles to their positive counterparts and rotating the corresponding azimuth angles for negative altitudes by 180 degrees. A noticeable flux from the side *D* (90 degree) of the cube is evident, and significantly, this flux orientation shifts with the cube's orientation, indicating a hardware-related issue rather than an external environmental influence.

In conclusion, this test reveals two critical observations. Firstly, the accumulation of entries at 90 degrees observed in both cases in Figure 5.41 suggests that this pattern does not result from a measured flux originating from a single direction; rather, it is indicative of a hardware issue, most likely associated with side *D* of the cube. Secondly, the symmetrical distribution of positive and negative altitude angles raises concerns about the accuracy of the angle reconstruction process. This necessitating further investigation.

To further investigate the hypothesis that events from below the cube's horizon should be assimilated into positive altitudes, because of a time resolution issue of the DT5202 conducting experiments with a radioactive test probe is proposed. This probe, characterized by a known direction and flux, would be positioned adjacent to the cube, with its location varied across different measurement sessions. This methodological approach would provide a controlled means to assess the cube's response to directional MIP flux, potentially isolating hardware issues and enhancing the accuracy of muon tracking.

# 6. Conclusion

The task was to design, construct, and operate a mobile device for tracking muons, named "MIP-Cube." This thesis presents the first prototype of such a device consisting of scintillator bars, wavelength shifting fibers, SiPMs and a commercial DAQ system, and demonstrates to work in this thesis.

The investigations conducted within this Master's thesis on the newly designed "MIP-Cube" project have yielded significant insights into the measurement and analysis of the flux and direction of MIPs, particularly muons of cosmic airshowers. Through a series of measurements conducted over various durations—from five minutes to 24 hours — the angular distribution of these subatomic particles has been precisely captured. The results affirm the expectation that detailed angle reconstruction is crucial for understanding muon fluxes and emphasize the importance of the spatial arrangement of scintillator pixels within the "MIP-Cube".

Furthermore, the "MIP-Cube" project was designed with mobility in mind, making it a versatile tool for field studies in various locations. Its compact dimensions, approximately 50 cm x 50 cm x 50 cm, enable easy transportation and deployment, allowing for the investigation of muon fluxes in diverse environments. This mobility is not only a testament to the "MIP-Cube"'s practical design but also significantly expands its application scope, from laboratory-based experiments to outdoor cosmic ray studies. This makes the small device ideal for showcase experiments with students or non-professionals.

The objective to detect an increased flux caused by an external structure, such as a building, was not achieved in the current set of experiments. A primary obstacle encountered was the unexplained higher flux originating from the "southwest" of the "MIP-Cube". This anomaly suggests that factors beyond the anticipated environmental influences, like the presence of a building, or an insufficient reconstruction, may be affecting the flux measurements. The inconsistency points towards the necessity of a more comprehensive dataset to accurately assess the impact of external structures on the flux pattern, which was not possible within this thesis.

Gathering a broader set of data could help isolate the cause of the increased flux from the southwest, allowing for a more detailed analysis of potential external influences. This approach would not only aid in understanding the current discrepancy but also enhance the cube's utility in detecting changes in flux patterns caused by environmental factors. Future experiments designed to capture a wider range of conditions and positions relative to known structures might provide the clarity needed to resolve this issue.

Furthermore, the analysis revealed that while the coincidence layer plays a role in reducing the total number of events per side, it has minimal impact on the accuracy of angle reconstruction. This suggests that the foundational methodology of the “MIP-Cube” is robust enough to conduct precise angle measurements regardless of the presence of this layer. When measuring flux, however the layer plays a pivotal role.

The strongest open issue of “MIP-Cube” in the current configuration is that a significant flux seems to originate from the ground to the upper side of the cube. This needs to be more investigateed. On addition two additional pixel layer at the bottom of the cube at the cost of the coincidence layer at one side, maybe the side which faces the sky, could be considered to close the gap in the altitude angle detection. This would utilize all 64 channels of the SiPM-array. Another point of investigation is to check the difference with a lead shielding above the scintillating Kuraray fibers. Also to increase the distance between the sides of the cube could be necessary. Additionally, to test the hypothesis the IAP building decreases the muon flux a test outside of buildings should be done.

To ensure the aimed mobility, a light-proofed box should be constructed, because in current condition the cube only can be used in the SPOCK laboratory or similar light-proofed environments. Another point would be the manual alignment of the cube side *A* to the north. An additional digital compass would improve the mobility and the "plug and play" character of the project.

In conclusion, the studies conducted on the “MIP-Cube” project within this Master’s thesis contribute valuable knowledge to the understanding of the interaction between cosmic muons and their environment. The findings lay a solid foundation for future investigations. The insights gained not only provide a robust framework for subsequent studies but also open avenues for optimisation of and expanding the “MIP-Cube” concept. This expansion could involve integrating various experiments within the cube’s cavity. The project also can serve as a showcase experiment, potentially making astroparticle physics more accessible to a broader audience. This could inspire interest and deepen public engagement with science.

# 7. Acronyms

**ADC** Analog to Digital Converter

**APD** Avalanche Photodiodes

**ASIC** Application-Specific Integrated Circuit

**CMB** cosmic microwave background

**DAQ** data acquisition system

**DOM** digital optical module

**DT5202** CAEN DT5202 device

**FPGA** Field Programmable Gate Array

**GZK** Greisen - Zatsepin - Kuzmin effect

**HG** High Gain

**HV** High Voltage

**LED** Light Emitting Diod

**LG** Low Gain

**MIP** minimum ionizing particle

**MIT** Massachusetts Institute of Technology

**PET** Positron Emission Tomography

**PHA** Peak High Analysis

**PMT** photon multiplier tube

**SiPM** silicon photomultiplier

**SLA** Stereolithography

**ToA** Time of Arrival

**ToT** Time over Threshold

**WLS** Wavelength shifting

# Acknowledgements

First and foremost, I would like to express my deepest gratitude to Prof. Dr. Ralph Engel, for the chance to realise this great Master's Thesis. Also, I want to thank Prof. Dr. Frank Simon for agreeing as second examiner.

At next I want to thank Thomas Huber for his invaluable guidance, patience, and support throughout the course of this research. His insight and expertise have been fundamental in shaping the direction and success of this work. Also, I want to thank Andreas Haungs for his guidance and optimistim through the time and especially his help at the end of the thesis.

I am also immensely grateful to Michael Riegel, whose expertise was instrumental in handling the building of the hardware of "MIP-Cube". His suggestions and feedback have greatly enhanced the quality of this thesis.

Special thanks go to my colleagues at KIT specifically the IAP-CRT group, for providing a stimulating and fun environment to work in. Their camaraderie and support have made this journey much more enjoyable.

To my family, my parents Regina and Christoph, my brother David and my fiancee Svenja, for their unconditional love, patience, and encouragement, I cannot thank you enough. You have been my rock, and this achievement is as much yours as it is mine.

I wish to extend my appreciation to Andreas Weindel and Bernd Hoffmann, for their advice and help with with soldering cables. And especially my friend Alexander Schneider, who supported me in programming and software development.

This thesis would not have been possible without the contributions and support of all these individuals and groups. To everyone who has been a part of this journey, thank you.

# A. Appendix

## A.1. Hardware

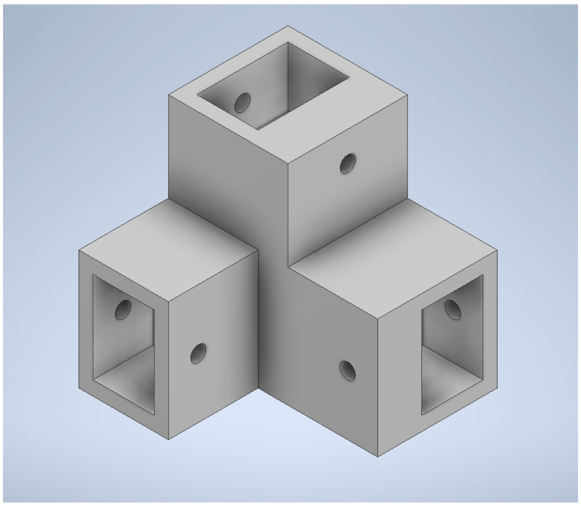

Figure A.1.: Isometric view at one 3D model for a corner

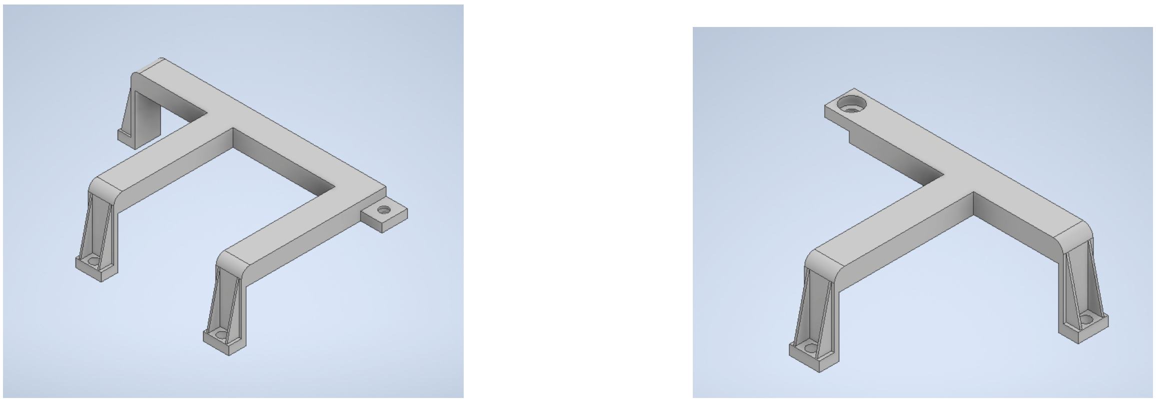

Figure A.2.: Isometric view one the two parts of the holder for the scintillators

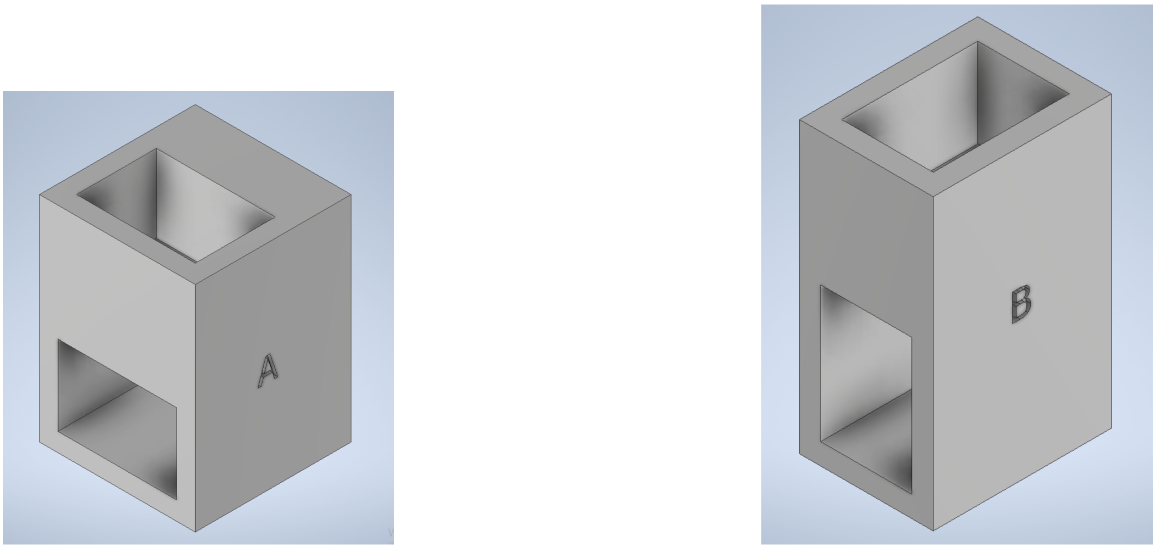

(a) Connector A (b) Connector B

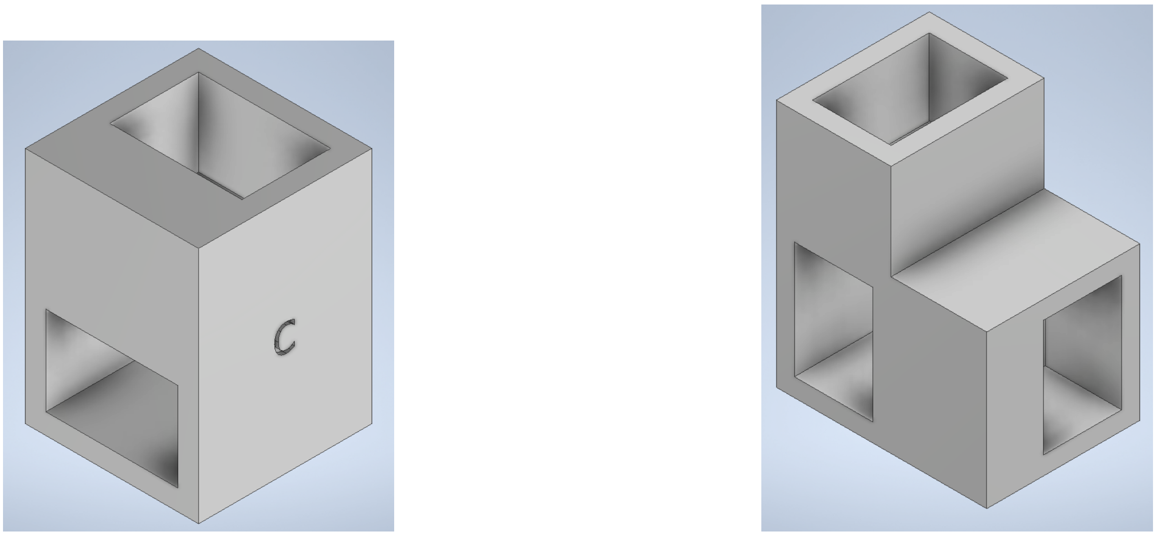

(c) Connector C (d) Connector D

(e) Connector E (f) Connector F

Figure A.3.: Connectors A to F

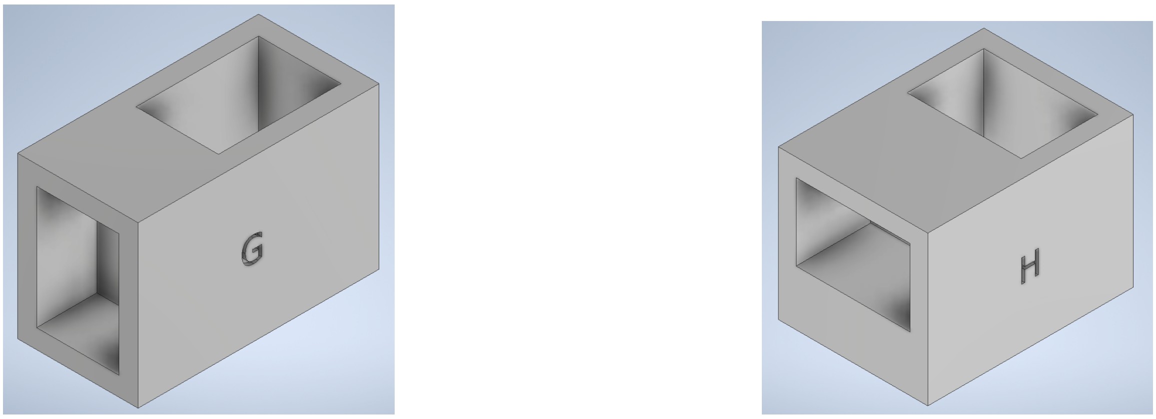

(a) Connector G (b) Connector H

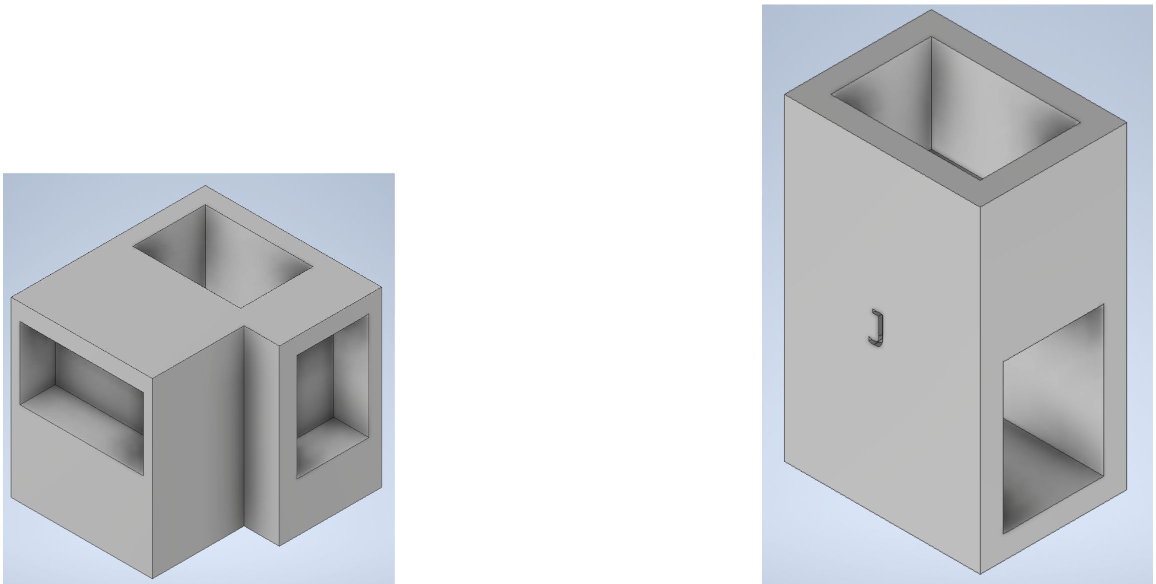

(c) Connector I (d) Connector J

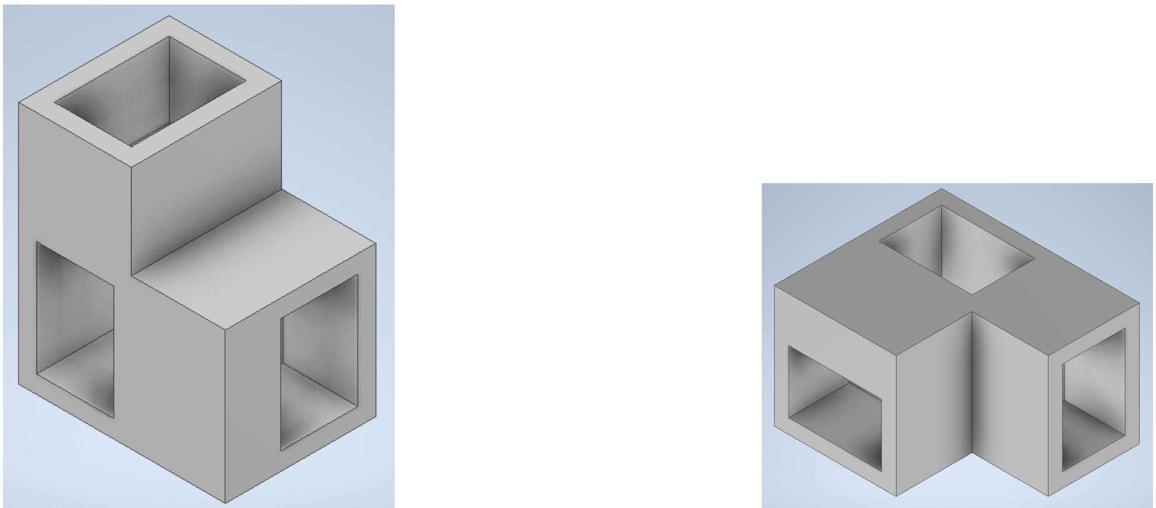

(e) Connector K (f) Connector L

Figure A.4.: Connectors G to L

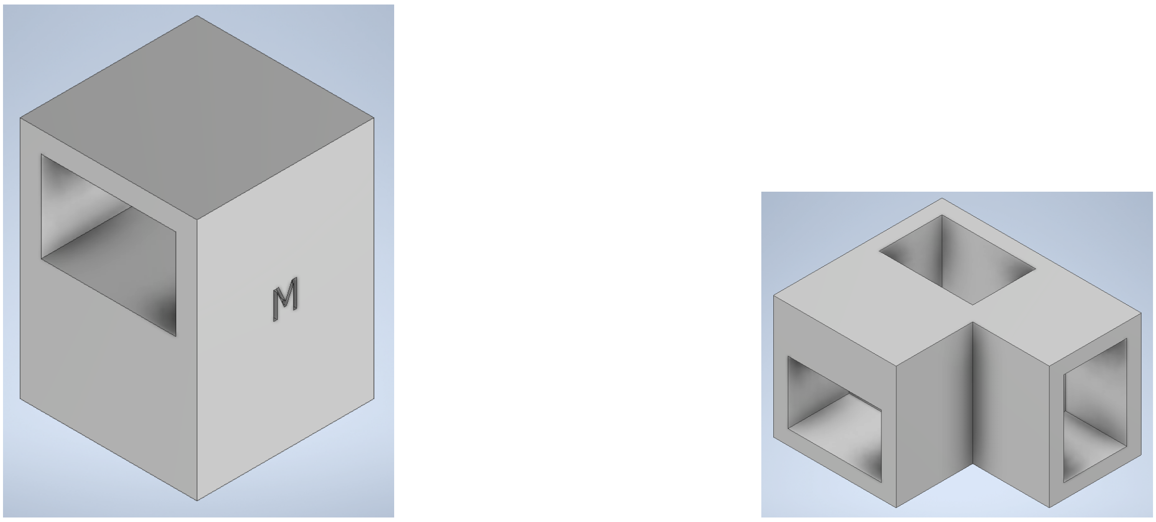

(a) Connector M

(b) Connector N

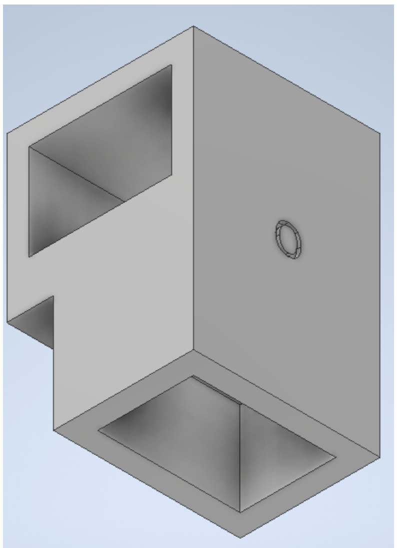

(c) Connector O

Figure A.5.: Connectors M to O

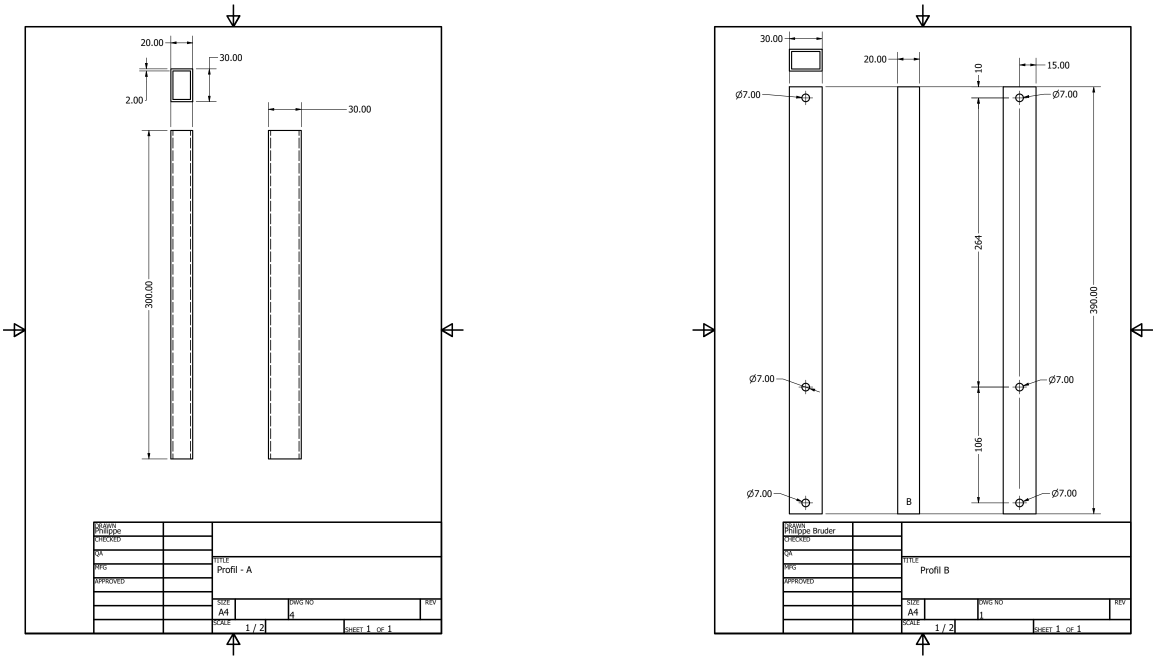

(a) Profile A

(b) Profile B

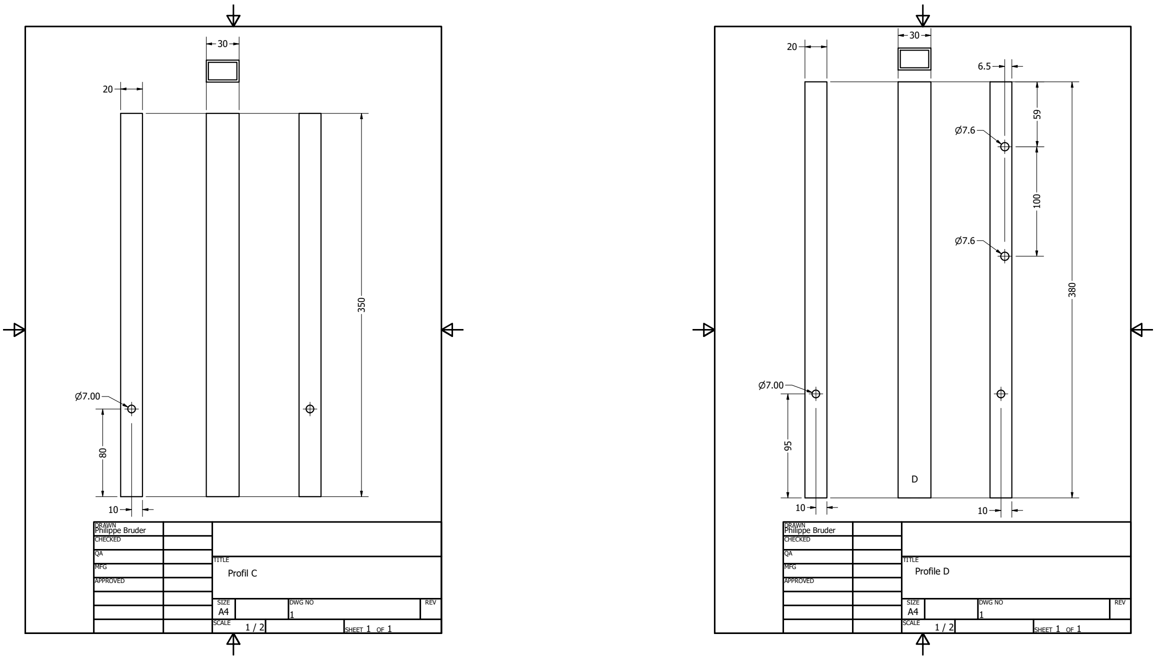

(c) Profile C

(d) Profile D

Figure A.6.: Profiles A to D

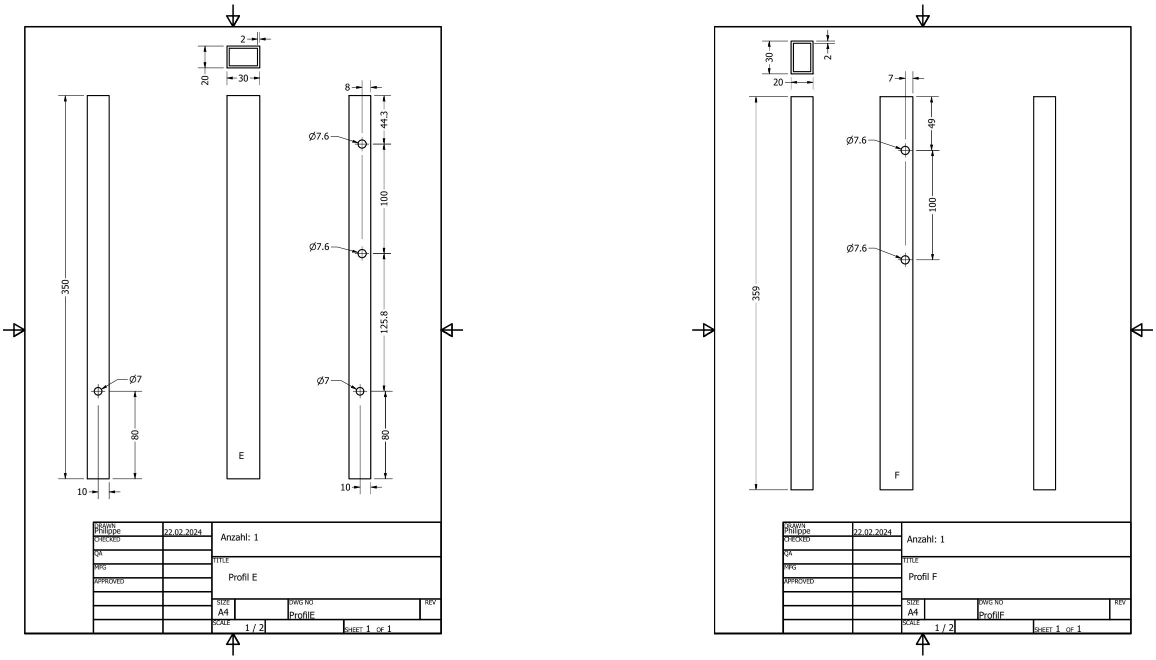

(a) Profile E (b) Profile F

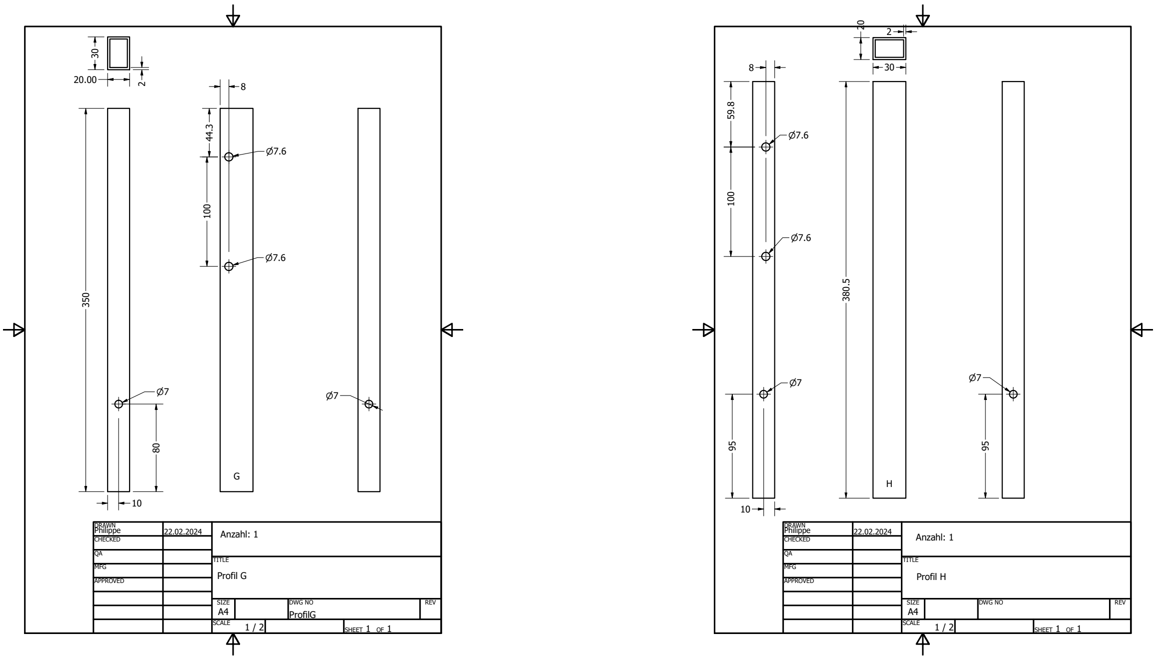

(c) Profile G (d) Profile H

Figure A.7.: Profiles E to H

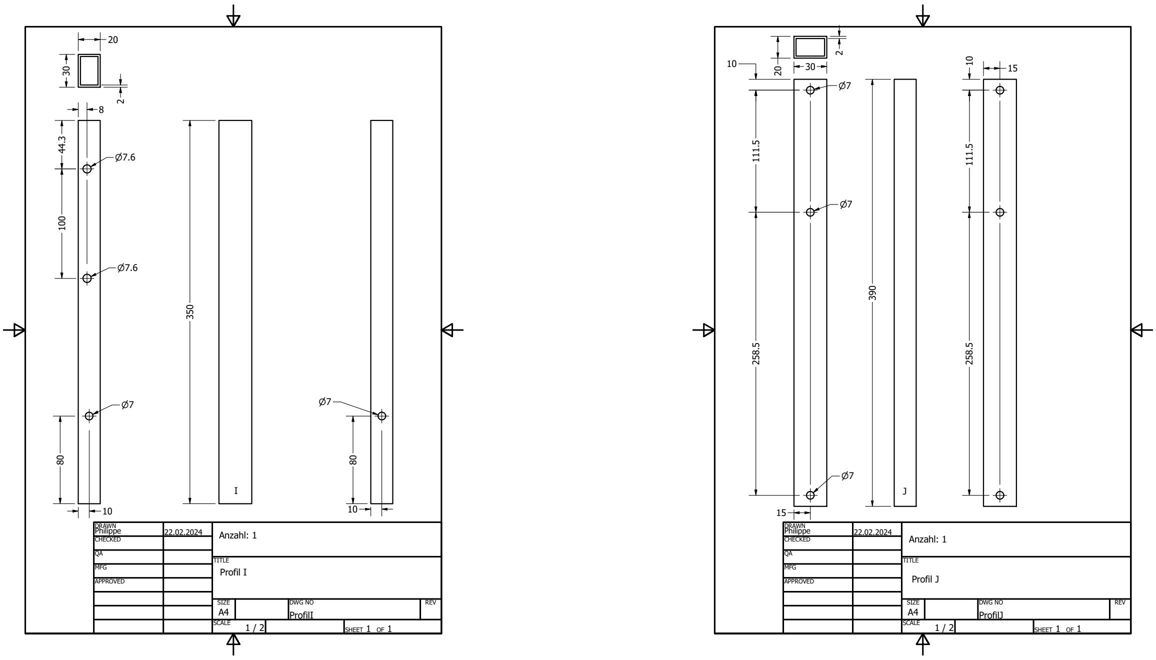

(a) Profile I

(b) Profile J

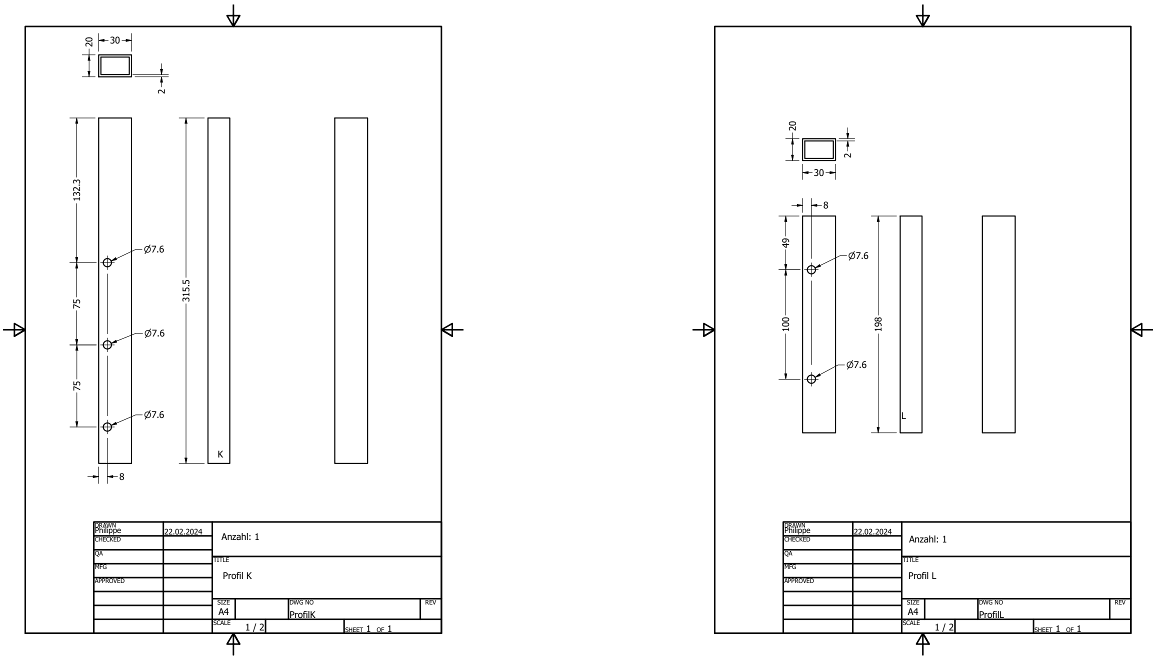

(c) Profile K

(d) Profile L

Figure A.8.: Profiles I to L

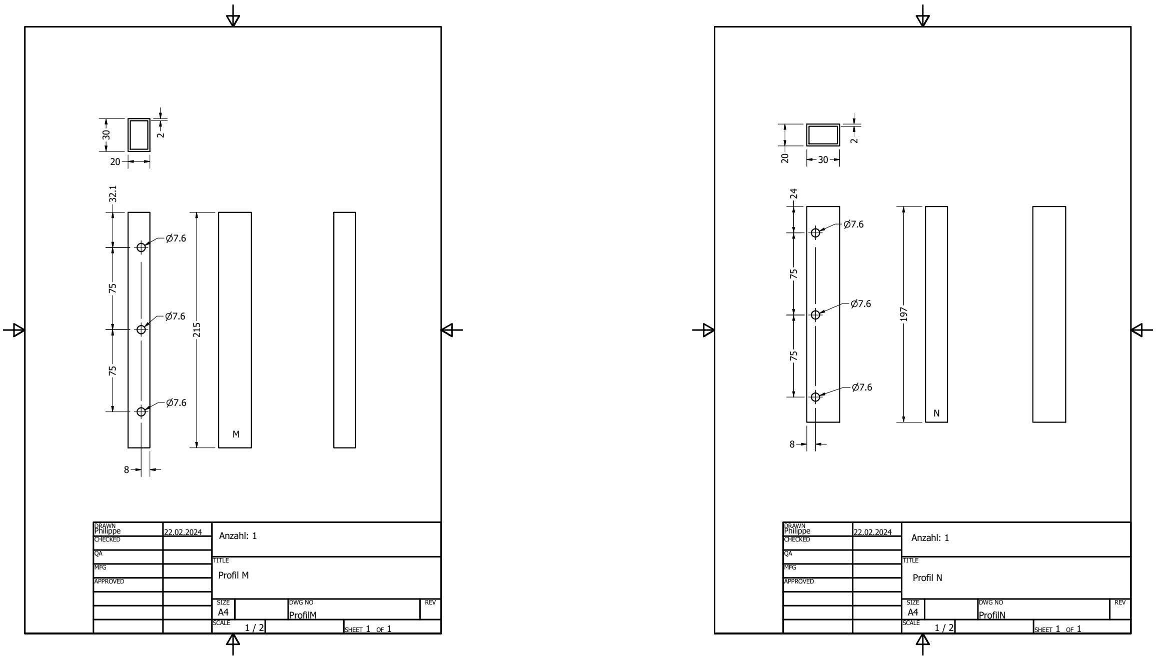

(a) Profile M

(b) Profile N

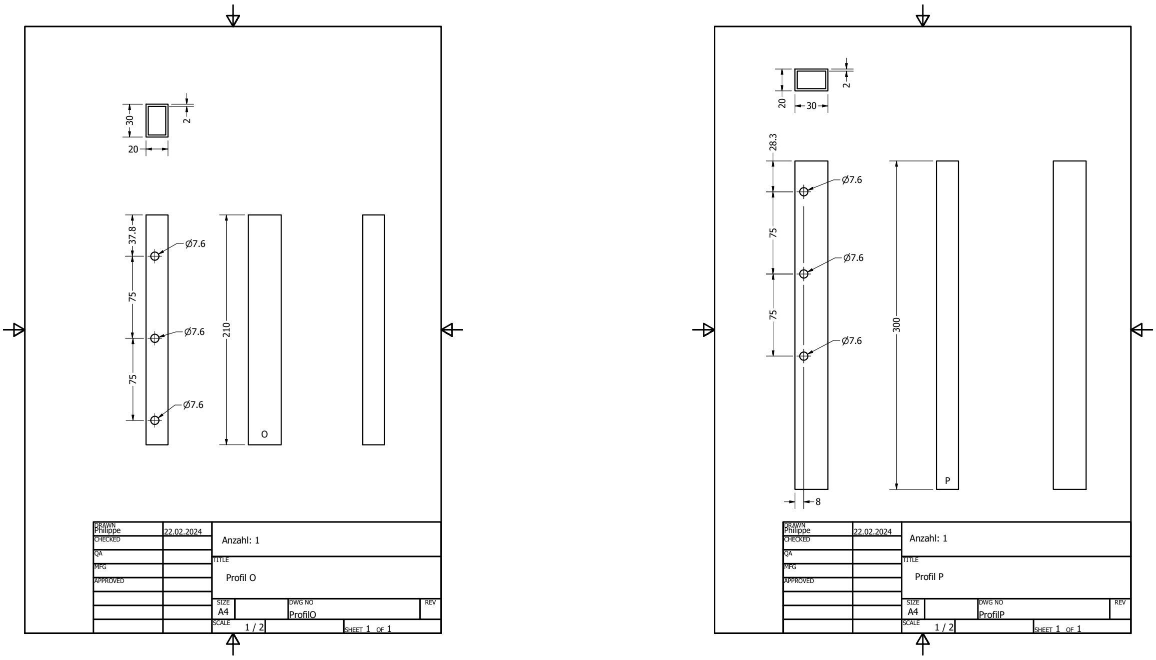

(c) Profile O

(d) Profile P

Figure A.9.: Profiles M to P

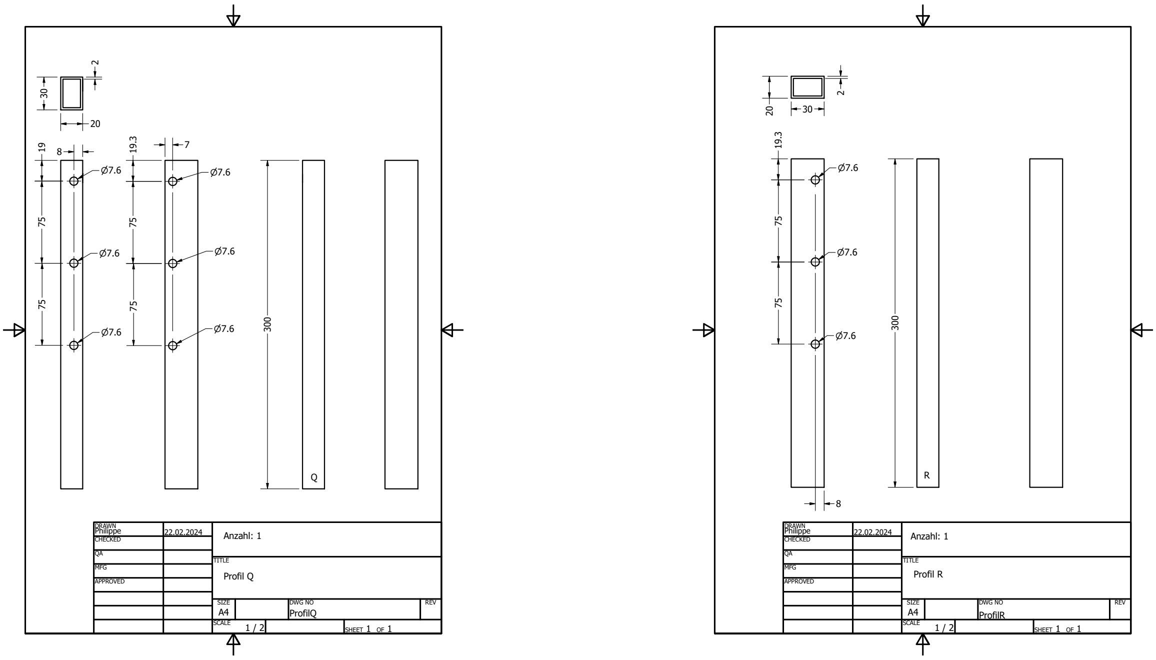

(a) Profile Q

(b) Profile R

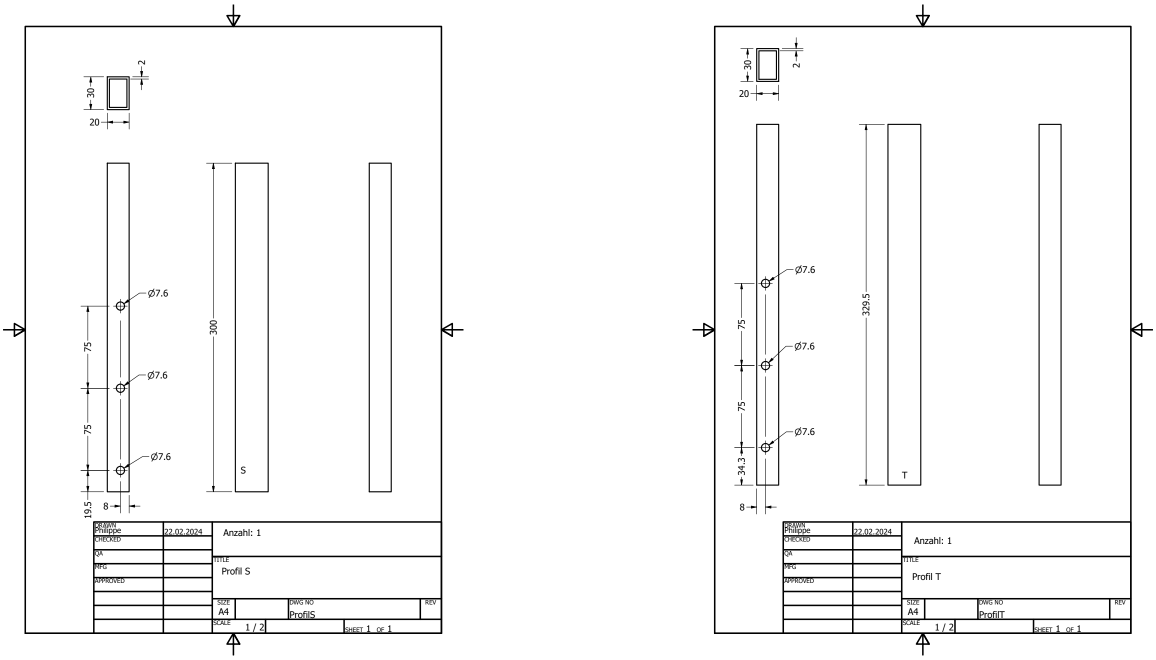

(c) Profile S

(d) Profile T

Figure A.10.: Profiles Q to T

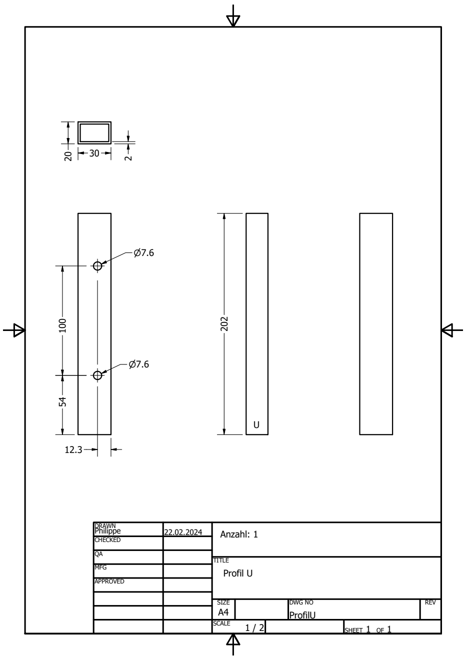

Figure A.11.: Profile U

## A.2. Source Code

Listing A.1: Python-resort-code

```
HardwareArray[1][0] = Array[0][0]
HardwareArray[2][0] = Array[0][1]
HardwareArray[0][0] = Array[0][2]
HardwareArray[3][0] = Array[0][3]
HardwareArray[0][1] = Array[0][4]
HardwareArray[3][1] = Array[0][5]
HardwareArray[1][1] = Array[0][6]
HardwareArray[2][1] = Array[0][7]

HardwareArray[1][2] = Array[1][0]
HardwareArray[2][2] = Array[1][1]
HardwareArray[0][2] = Array[1][2]
HardwareArray[3][2] = Array[1][3]
HardwareArray[0][3] = Array[1][4]
HardwareArray[3][3] = Array[1][5]
HardwareArray[1][3] = Array[1][6]
HardwareArray[2][3] = Array[1][7]

HardwareArray[1][4] = Array[2][0]
HardwareArray[2][4] = Array[2][1]
HardwareArray[0][4] = Array[2][2]
HardwareArray[3][4] = Array[2][3]
HardwareArray[0][5] = Array[2][4]
HardwareArray[3][5] = Array[2][5]
HardwareArray[1][5] = Array[2][6]
HardwareArray[2][5] = Array[2][7]

HardwareArray[1][6] = Array[3][0]
HardwareArray[2][6] = Array[3][1]
HardwareArray[0][6] = Array[3][2]
HardwareArray[3][6] = Array[3][3]
HardwareArray[0][7] = Array[3][4]
HardwareArray[3][7] = Array[3][5]
HardwareArray[1][7] = Array[3][6]
HardwareArray[2][7] = Array[3][7]

HardwareArray[5][0] = Array[4][0]
HardwareArray[6][0] = Array[4][1]
HardwareArray[4][0] = Array[4][2]
HardwareArray[7][0] = Array[4][3]
HardwareArray[4][1] = Array[4][4]
```

```
HardwareArray[7][1] = Array[4][5]
HardwareArray[5][1] = Array[4][6]
HardwareArray[6][1] = Array[4][7]

HardwareArray[5][2] = Array[5][0]
HardwareArray[6][2] = Array[5][1]
HardwareArray[4][2] = Array[5][2]
HardwareArray[7][2] = Array[5][3]
HardwareArray[4][3] = Array[5][4]
HardwareArray[7][3] = Array[5][5]
HardwareArray[5][3] = Array[5][6]
HardwareArray[6][3] = Array[5][7]

HardwareArray[5][4] = Array[6][0]
HardwareArray[6][4] = Array[6][1]
HardwareArray[4][4] = Array[6][2]
HardwareArray[7][4] = Array[6][3]
HardwareArray[4][5] = Array[6][4]
HardwareArray[7][5] = Array[6][5]
HardwareArray[5][5] = Array[6][6]
HardwareArray[6][5] = Array[6][7]

HardwareArray[5][6] = Array[7][0]
HardwareArray[6][6] = Array[7][1]
HardwareArray[4][6] = Array[7][2]
HardwareArray[7][6] = Array[7][3]
HardwareArray[4][7] = Array[7][4]
HardwareArray[7][7] = Array[7][5]
HardwareArray[5][7] = Array[7][6]
HardwareArray[6][7] = Array[7][7]
```

Listing A.2: Python code to identify MIPs with and without coincidence layer

```
##############################
# setup custom mappings      #
##############################

A = [26, 55, 5, 38, 47, 44, 63, 14, 23, 20, 29]
B = [37, 53, 1, 46, 45, 36, 62, 12, 31, 22, 21]
C = [33, 59, 3, 40, 43, 11, 60, 8, 17, 30, 52]
D = [24, 51, 7, 48, 39, 34, 56, 4, 15, 18, 27]
E = [28, 49, 0, 32, 41, 42, 58, 10, 25, 16, 19]

trigids = [A[0], B[0], C[0], D[0], E[0]]
chApix = {}
chBpix = {}
chCpix = {}
chDpix = {}
chEpix = {}

for i in range(1, 11):
    chApix[A[i]] = i
    chBpix[B[i]] = i
    chCpix[C[i]] = i
    chDpix[D[i]] = i
    chEpix[E[i]] = i


pixels = [[(1,  6), (2,  6), (3,  6), (4,  6), (5,  6)],
          [(1,  7), (2,  7), (3,  7), (4,  7), (5,  7)],
          [(1,  8), (2,  8), (3,  8), (4,  8), (5,  8)],
          [(1,  9), (2,  9), (3,  9), (4,  9), (5,  9)],
          [(1, 10), (2, 10), (3, 10), (4, 10), (5, 10)]]

pixmap = {}

for i in range(len(pixels)):
    for j in range(len(pixels[0])):
        t1, t2 = pixels[i][j]
        pixmap[(t1, t2)] = (i, j)
        pixmap[(t2, t1)] = (i, j)

##############################
# set rules for analysis     #
##############################
```

```
COINCTIME = 1.5          # ns
UNCERTAINTY = 0.025      # m

def not_coincidence(tstamp1, tstamp2):
    return abs(tstamp1 - tstamp2) <= COINCTIME

def not_coincidence_trajectory(event):
    ts1_1, ts1_2 = event.first.toa
    ts2_1, ts2_2 = event.second.toa

    return any([not_coincidence(ts1_1, ts2_1),
                not_coincidence(ts1_1, ts2_2),
                not_coincidence(ts1_2, ts2_1),
                not_coincidence(ts1_2, ts2_2)])
##############################
# parsing of events          #
##############################

a, j = 0, 0
COINCTIME = 1.5

filtered_listA = []
filtered_listB = []
filtered_listC = []
filtered_listD = []
filtered_listE = []

filtered_list = [
    filtered_listA, filtered_listB, filtered_listC, filtered_listD,
    filtered_listE
]

count_ch = []
number_of_rejections = 0


def not_coincidence(tstamp1, tstamp2):
    return abs(tstamp1 - tstamp2) <= COINCTIME


def cubeside(ch1, ch2):
    if ch1 in chApix and ch2 in chApix:
        return chApix[ch1], chApix[ch2], 'A'

    elif ch1 in chBpix and ch2 in chBpix:
```

```
        return chBpix[ch1], chBpix[ch2], 'B'

    elif ch1 in chCpix and ch2 in chCpix:
        return chCpix[ch1], chCpix[ch2], 'C'

    elif ch1 in chDpix and ch2 in chDpix:
        return chDpix[ch1], chDpix[ch2], 'D'

    elif ch1 in chEpix and ch2 in chEpix:
        return chEpix[ch1], chEpix[ch2], 'E'

    else:
        return 0, 0, 'N'


eventsA = []
eventsB = []
eventsC = []
eventsD = []
eventsE = []

#events = [eventsA = [], eventsB = [],
#           eventsC = [], eventsD = [], eventsE = []]
events = [eventsA, eventsB, eventsC, eventsD, eventsE]

for i in range(len(data['Tstamp_us']) - 1):
    if a < j:  # skip already checked timestamps
        a += 1
        continue

    if data['Tstamp_us'][i] == data['Tstamp_us'][i + 1]:
        j = 0
        current_eventA = []
        current_eventB = []
        current_eventC = []
        current_eventD = []
        current_eventE = []
        current_event = [
            current_eventA, current_eventB,
            current_eventC, current_eventD,
            current_eventE
        ]

        while data['Tstamp_us'][i] == data['Tstamp_us'][i +
```

```
                                                        j]:
# length of event
            j += 1

        if j > 1:
            triggered = [(data['ToA_ns'][i], data['Ch'][i])
                         for i in range(i, i + j)]
            trigger_level_tstamps = [
                ts for ts, ch in triggered if ch in trigids
            ]
            possible_pairsA = []
            possible_pairsB = []
            possible_pairsC = []
            possible_pairsD = []
            possible_pairsE = []
            sides = [
                possible_pairsA, possible_pairsB, possible_pairsC,
                possible_pairsD, possible_pairsE
            ]

            for i1, trig1 in enumerate(triggered):  #counts i und i+j
                for trig2 in triggered[i1 + 1:]:
                    ts1, ch1 = trig1
                    ts2, ch2 = trig2

                    if ch1 in trigids or ch2 in trigids:
                        # ignore trigger layers for pair creation
                        continue

                    if not_coincidence(ts1, ts2):
                        px, py, side = cubeside(ch1, ch2)
                        trigger_layer_active=any([not_coincidence(ts1,
                                                   tlts) for tlts in
                                                   trigger_level_tstamps
                                                   ]) \ or any([
                                                   not_coincidence(ts2,
                                                   tlts) for tlts in
                                                   trigger_level_tstamps
                                                   ])

                        if side == 'A':
                            possible_pairsA.append(
                                ((px, py), trigger_layer_active))

                        elif side == 'B':
```

```
                    possible_pairsB.append(
                        ((px, py), trigger_layer_active))

                elif side == 'C':
                    possible_pairsC.append(
                        ((px, py), trigger_layer_active))

                elif side == 'D':
                    possible_pairsD.append(
                        ((px, py), trigger_layer_active))

                elif side == 'E':
                    possible_pairsE.append(
                        ((px, py), trigger_layer_active))

    for k in range(len(sides)):
        for pair, trigger_layer_active in sides[k]:
            if pair in pixmap and k == 0:
                current_eventA.append(
                    (pixmap[pair], trigger_layer_active))

            elif pair in pixmap and k == 1:
                current_eventB.append(
                    (pixmap[pair], trigger_layer_active))

            elif pair in pixmap and k == 2:
                current_eventC.append(
                    (pixmap[pair], trigger_layer_active))

            elif pair in pixmap and k == 3:
                current_eventD.append(
                    (pixmap[pair], trigger_layer_active))

            elif pair in pixmap and k == 4:
                current_eventE.append(
                    (pixmap[pair], trigger_layer_active))

    #count double pixels
    #######################
    reject_current_event = False

    if reject_current_event:
        number_of_rejections += 1

    if len(current_eventA) == 1:
```

```
    eventsA.append(current_eventA)

if len(current_eventB) == 1:
    eventsB.append(current_eventB)

if len(current_eventC) == 1:
    eventsC.append(current_eventC)

if len(current_eventD) == 1:
    eventsD.append(current_eventD)

if len(current_eventE) == 1:
    eventsE.append(current_eventE)

for x in range(len(filtered_list)):
    filtered_list[x].clear()
```

## A.3. Measurments

What follows are additional plots from the meaurements not shown in the text.

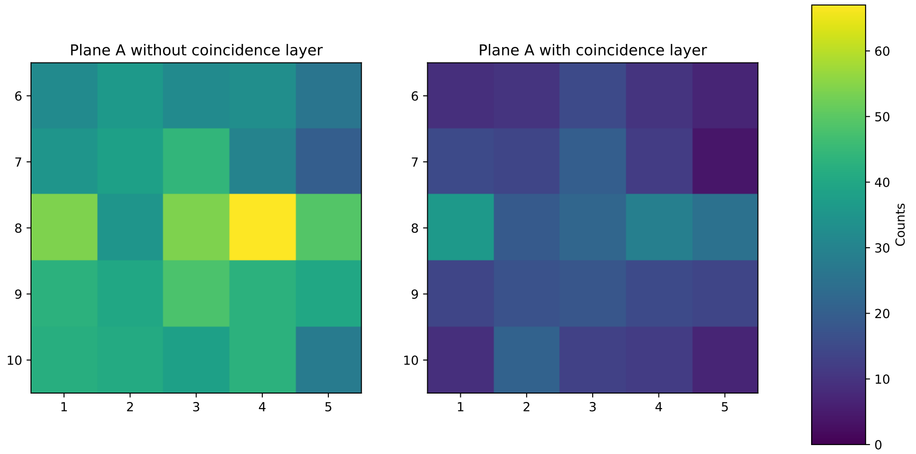

(a) 5min measurement heatmap Side A.

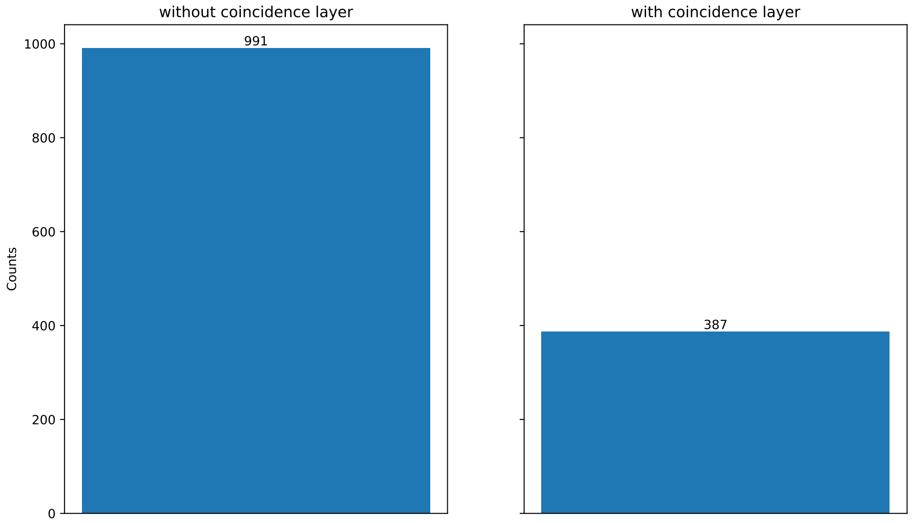

(b) 5min measurement comprehension events with and without coincidence layer of side A.

Figure A.12.: Side A 5min measurement

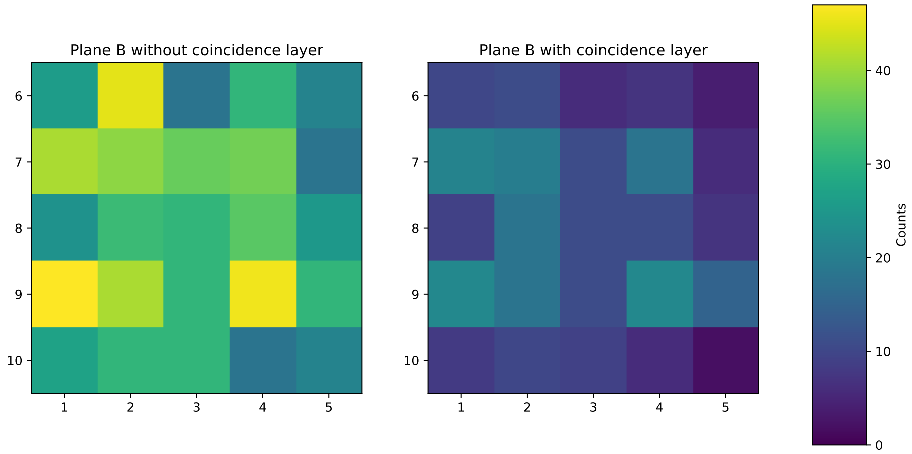

(a) 5min measurement heatmap Side B.

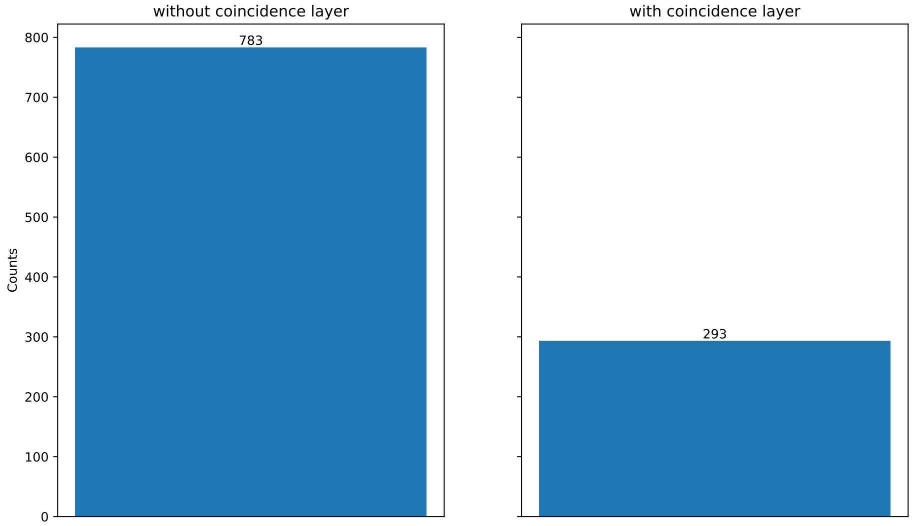

(b) 5min measurement comprehension events with and without coincidence layer of side B.

Figure A.13.: Side B 5min measurement

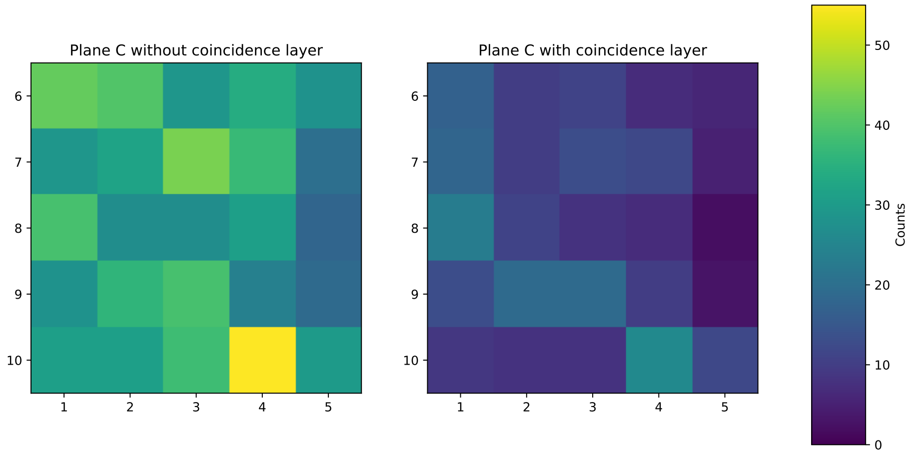

(a) 5min measurement heatmap side C.

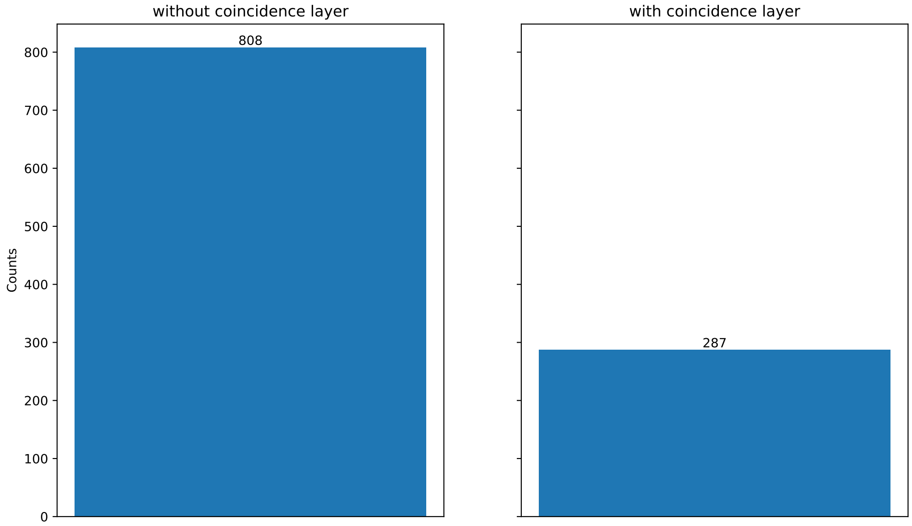

(b) 5min measurement comprehension events with and without coincidence layer of side C.

Figure A.14.: Side C 5min measurement

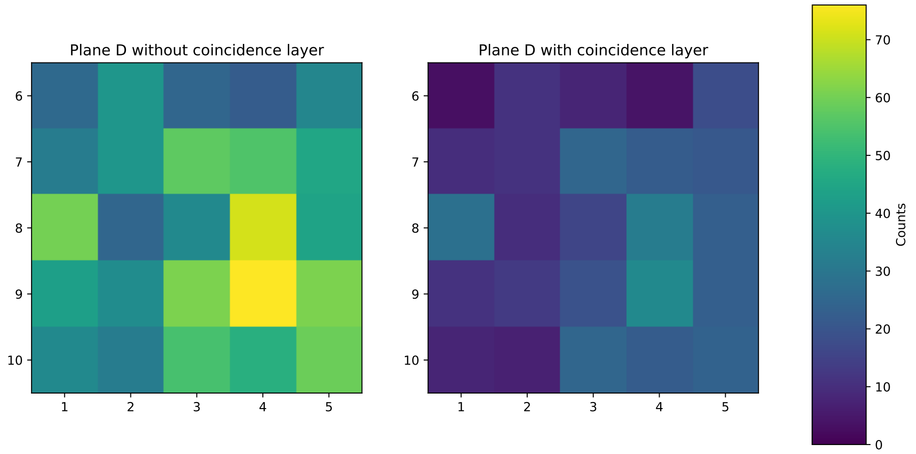

(a) 5min measurement heatmap Side D.

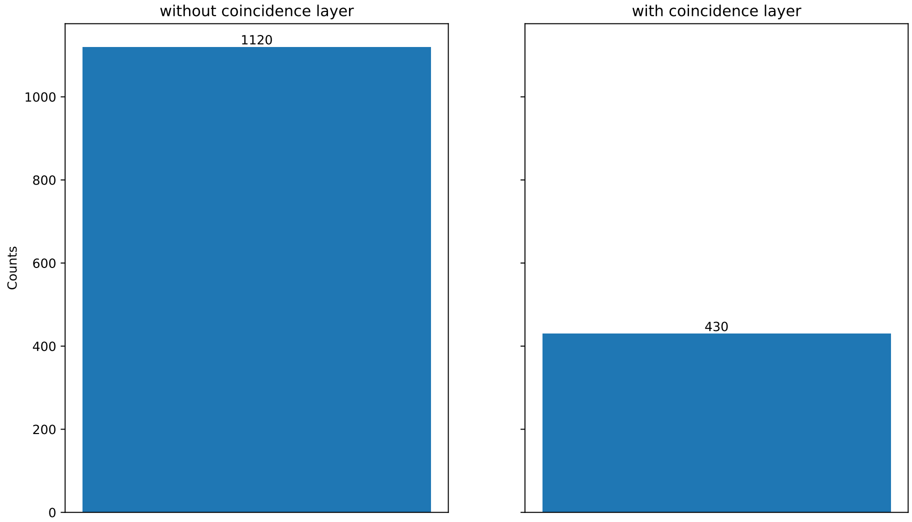

(b) 5min measurement comprehension events with and without coincidence layer of side D.

Figure A.15.: Side D 5min measurement

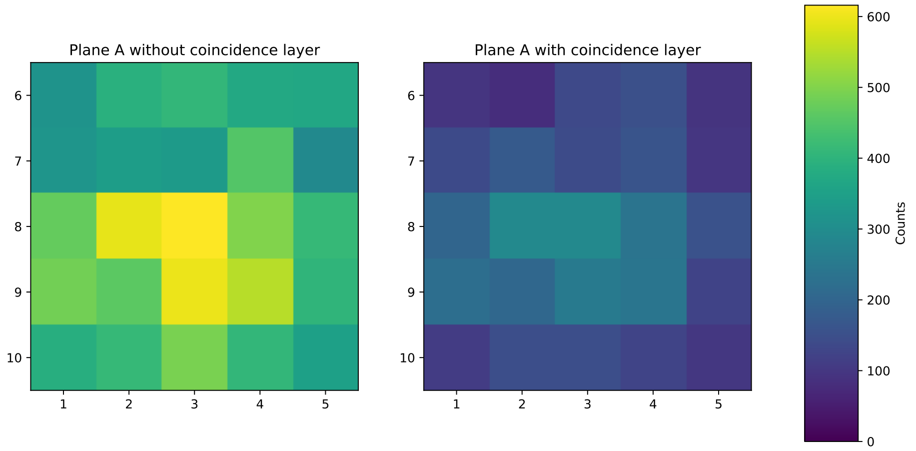

(a) 1 hour measurement heatmap Side A.

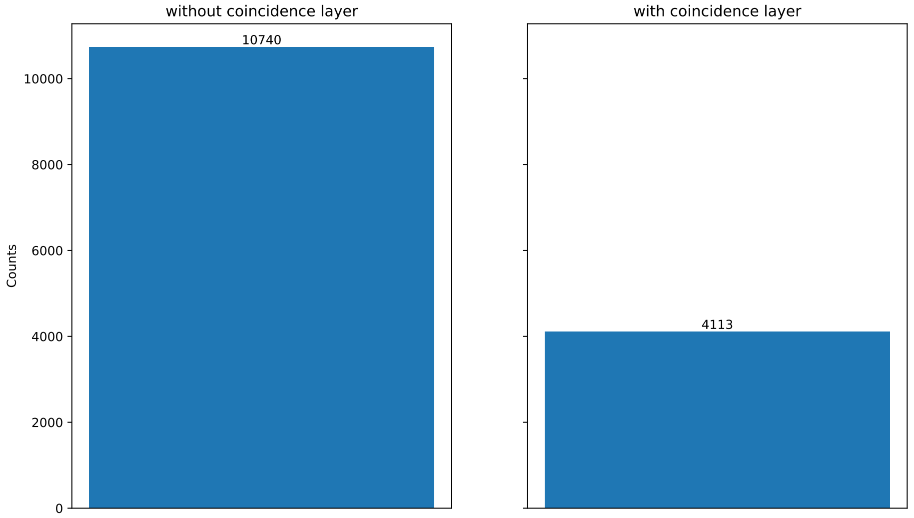

(b) 1 hour measurement comprehension events with and without coincidence layer of side A.

Figure A.16.: Side A 1 hour measurement

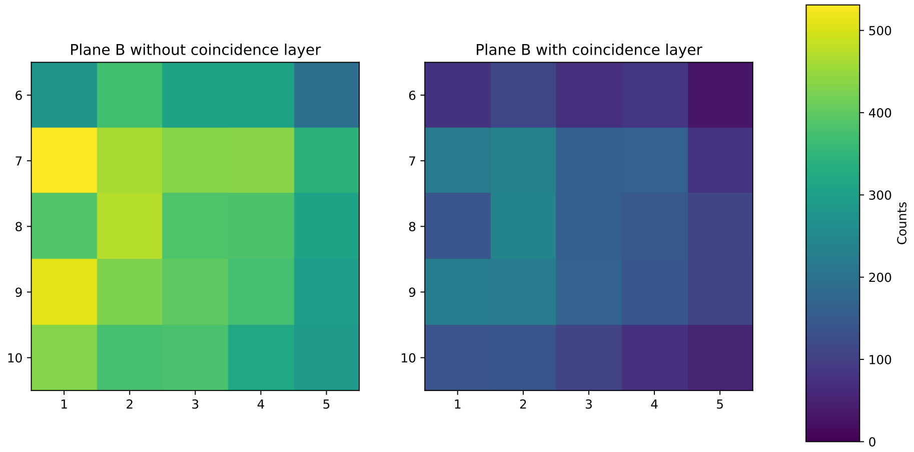

(a) 1 hour measurement heatmap Side B.

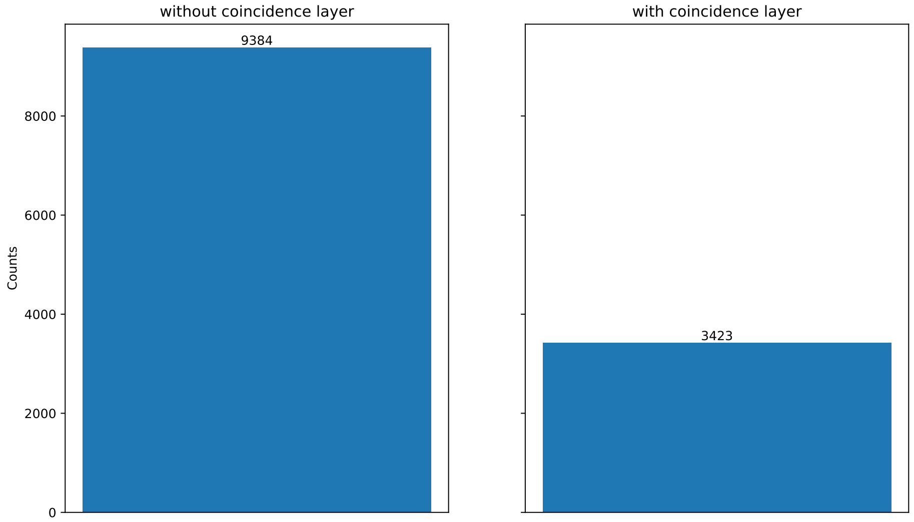

(b) 1 hour measurement comprehension events with and without coincidence layer of side B.

Figure A.17.: Side B 1 hour measurement

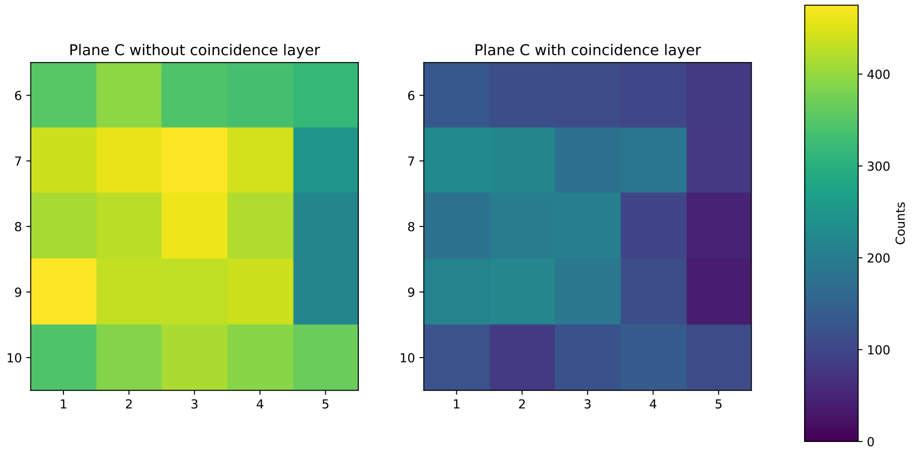

(a) 1 hour measurement heatmap side C.

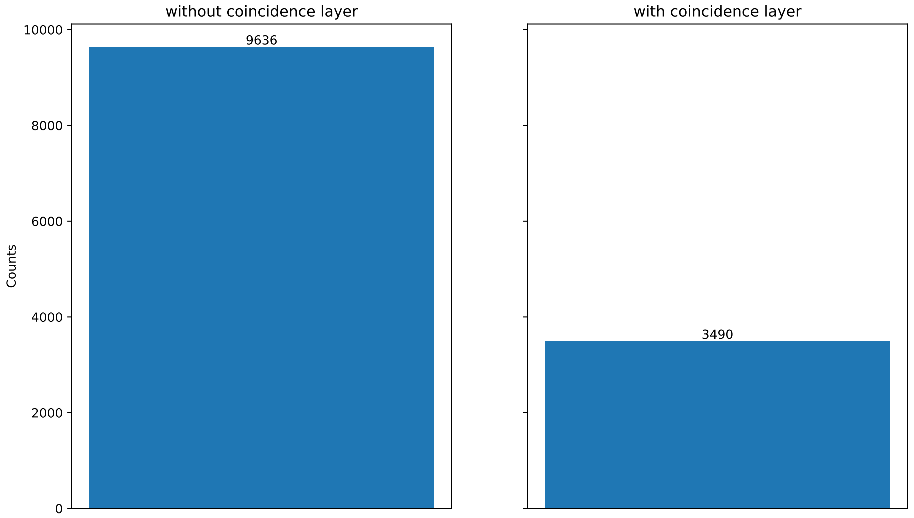

(b) 1 hour measurement comprehension events with and without coincidence layer of side C.

Figure A.18.: Side C 1 hour measurement

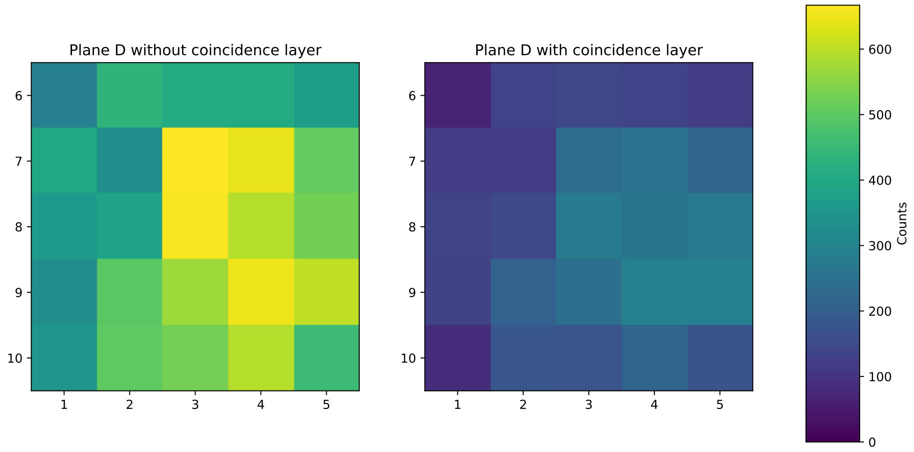

(a) 1 hour measurement heatmap Side D.

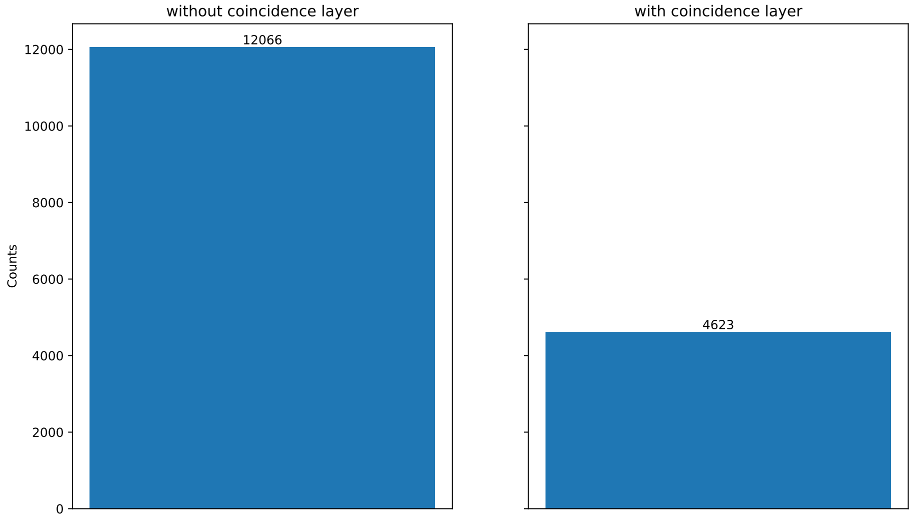

(b) 1 hour measurement comprehension events with and without coincidence layer of side D.

Figure A.19.: Side D 1 hour measurement

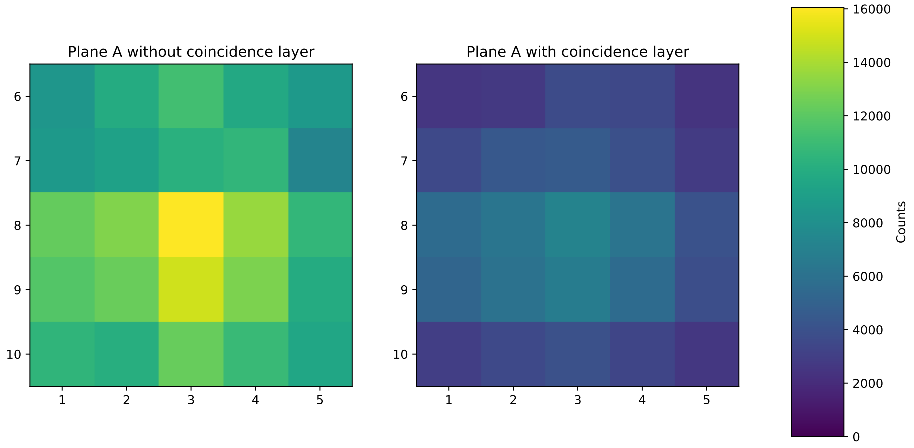

(a) 24 hour measurement heatmap Side A.

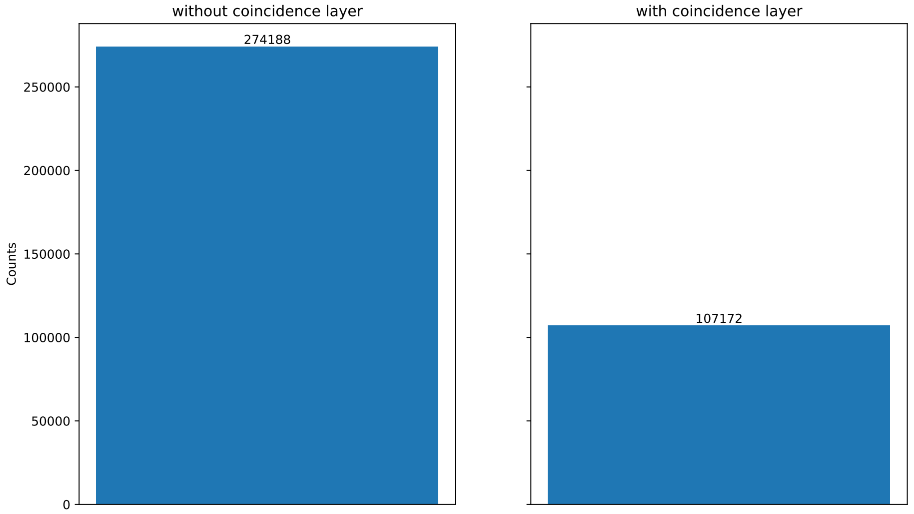

(b) 24 hour measurement comprehension events with and without coincidence layer of side A.

Figure A.20.: Side A 24 hour measurement

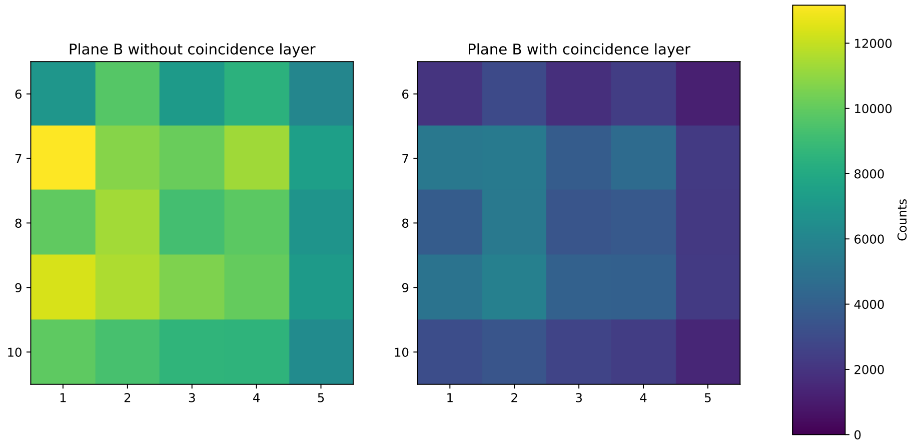

(a) 24 hour measurement heatmap Side B.

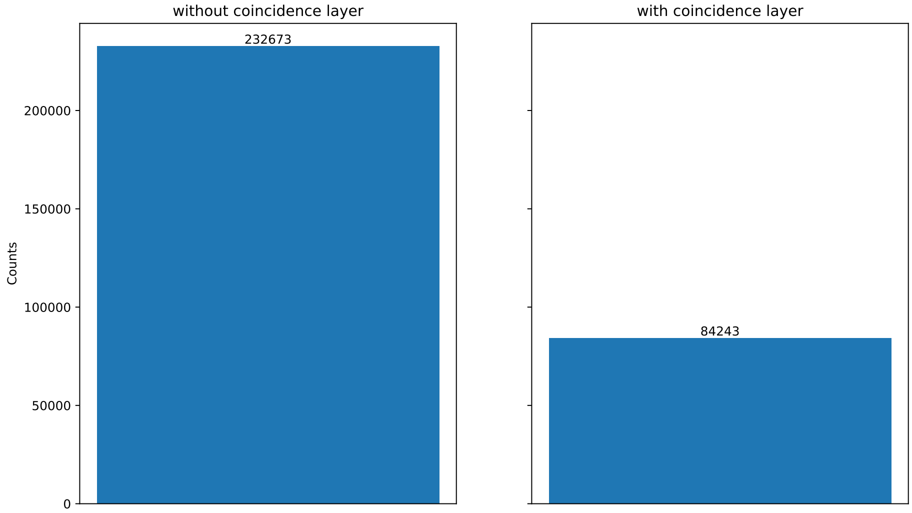

(b) 24 hour measurement comprehension events with and without coincidence layer of side B.

Figure A.21.: Side B 24 hour measurement

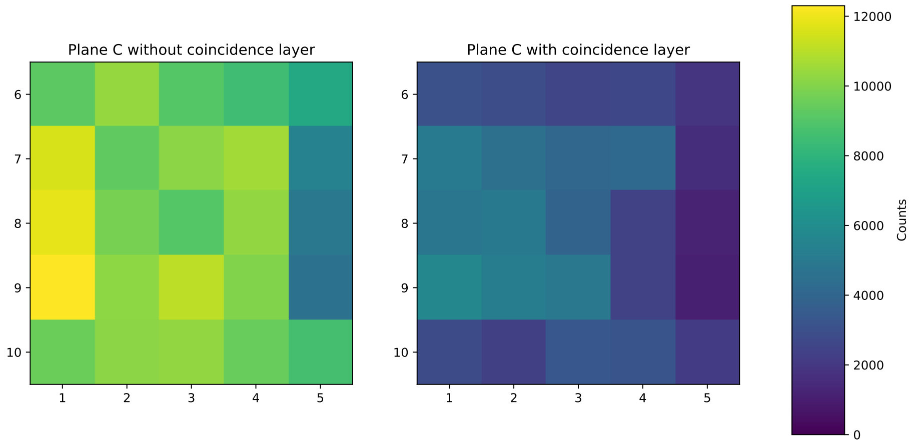

(a) 24 hour measurement heatmap side C.

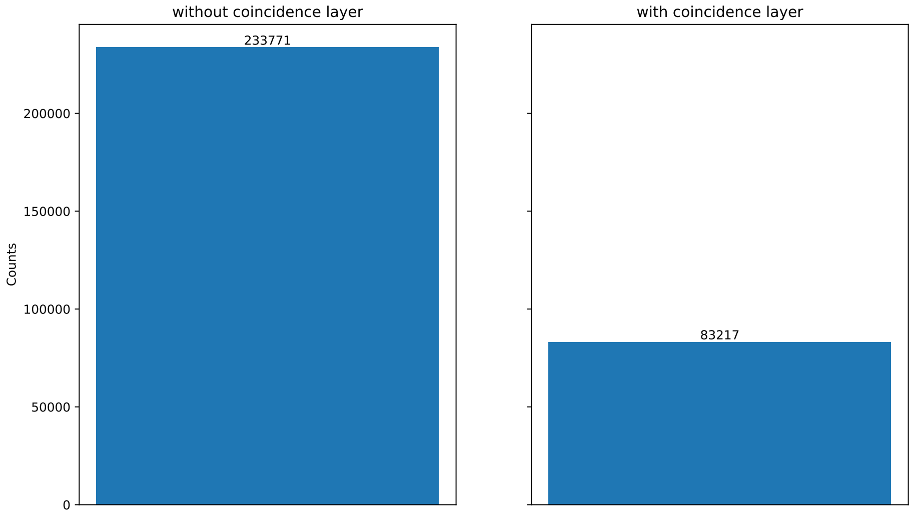

(b) 24 hour measurement comprehension events with and without coincidence layer of side C.

Figure A.22.: Side C 24 hour measurement

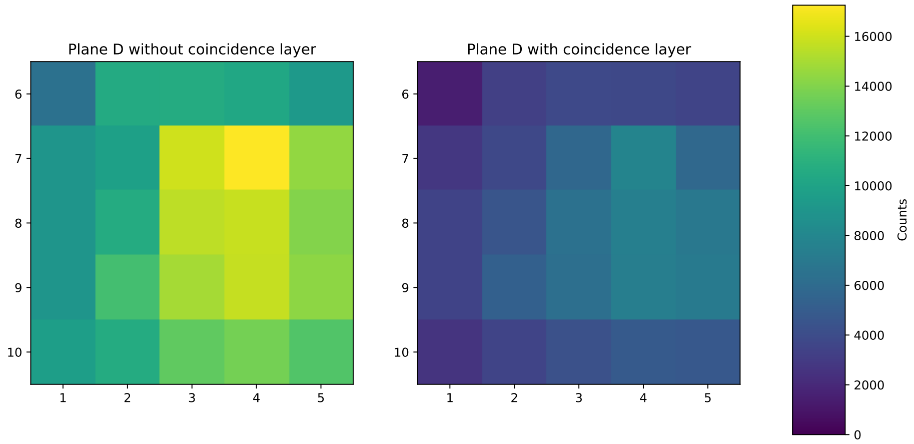

(a) 24 hour measurement heatmap Side D.

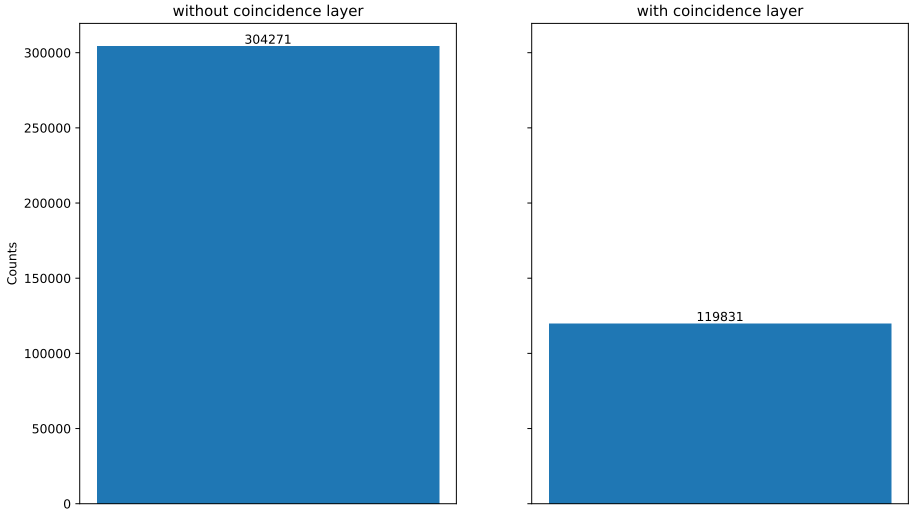

(b) 24 hour measurement comprehension events with and without coincidence layer of side D.

Figure A.23.: Side D 24 hour measurement

# Bibliography

[1] G. Azuelos et al. “Impact of energy and luminosity upgrades at LHC on the physics programme of ATLAS”. In: *Journal of Physics G: Nuclear and Particle Physics* 28.9 (Aug. 2002), pp. 2453–2474. ISSN: 0954-3899. DOI: `10.1088/0954-3899/28/9/309`. URL: `http://dx.doi.org/10.1088/0954-3899/28/9/309`.

[2] S. Coleman and S. L. Glashow. “Cosmic ray and neutrino tests of special relativity”. In: *Physics Letters B* 405.3–4 (July 1997), pp. 249–252. ISSN: 0370-2693. DOI: `10.1016/s0370-2693(97)00638-2`. URL: `http://dx.doi.org/10.1016/S0370-2693(97)00638-2`.

[3] J. Madsen. “Cosmic ray strangelets”. In: *Journal of Physics G: Nuclear and Particle Physics* 31.6 (May 2005), S833–S839. ISSN: 1361-6471. DOI: `10.1088/0954-3899/31/6/025`. URL: `http://dx.doi.org/10.1088/0954-3899/31/6/025`.

[4] J. Alfaro and G. Palma. “Loop quantum gravity and ultrahigh energy cosmic rays”. In: *Physical Review D* 67.8 (Apr. 2003). ISSN: 1089-4918. DOI: `10.1103/physrevd.67.083003`. URL: `http://dx.doi.org/10.1103/PhysRevD.67.083003`.

[5] W. Bietenholz. “Cosmic rays and the search for a Lorentz Invariance Violation”. In: *Physics Reports* 505.5 (Aug. 2011), pp. 145–185. ISSN: 0370-1573. DOI: `10.1016/j.physrep.2011.04.002`. URL: `http://dx.doi.org/10.1016/j.physrep.2011.04.002`.

[6] Y. Wang et al. “A High Spatial Resolution Muon Tomography Prototype System Based on Micromegas Detector”. In: *IEEE Transactions on Nuclear Science* 69.1 (Jan. 2022), pp. 78–85. ISSN: 1558-1578. DOI: `10.1109/tns.2021.3137415`. URL: `http://dx.doi.org/10.1109/TNS.2021.3137415`.

[7] V. Pvevc and V. A. Kudryavtsev. “Muon-induced background in a next-generation dark matter experiment based on liquid xenon”. In: *LOW RADIOACTIVITY TECHNIQUES 2022 (LRT 2022): Proceedings of the 8th International Workshop on Low Radioactivity Techniques* (2022). URL: `https://api.semanticscholar.org/CorpusID:253510975`.

[8] M. Karus. “Development of a Calibration Stand for Photosensors for Extremely High-Energy Cosmic Ray Research”. 51.03.04; LK 01. PhD thesis. Karlsruher Institut für Technologie (KIT), 2016. DOI: `10.5445/IR/1000053731`.

[9] V. F. Hess. *Victor F. Hess Nobel Lecture*. `https://www.nobelprize.org/prizes/physics/1936/hess/lecture/`. Accessed: 1-10-2024.

[10] B. Rossi. “Magnetic Experiments on the Cosmic Rays.” In: *Nature* 128.3225 (Aug. 1931), pp. 300–301. DOI: `10.1038/128300a0`.

[11] P. Auger et al. “Extensive Cosmic-Ray Showers”. In: *Rev. Mod. Phys.* 11 (3-4 June 1939), pp. 288–291. DOI: `10.1103/RevModPhys.11.288`. URL: `https://link.aps.org/doi/10.1103/RevModPhys.11.288`.

[12] G. W. Clark et al. “Cosmic-Ray Air Showers at Sea Level”. In: *Phys. Rev.* 122 (2 Apr. 1961), pp. 637–654. DOI: `10.1103/PhysRev.122.637`. URL: `https://link.aps.org/doi/10.1103/PhysRev.122.637`.

[13] “The Pierre Auger Cosmic Ray Observatory”. In: *Nuclear Instruments and Methods in Physics Research Section A: Accelerators, Spectrometers, Detectors and Associated Equipment* 798 (Oct. 2015), pp. 172–213. ISSN: 0168-9002. DOI: `10.1016/j.nima.2015.06.058`. URL: `http://dx.doi.org/10.1016/j.nima.2015.06.058`.

[14] R. Alves Batista et al. “Open Questions in Cosmic-Ray Research at Ultrahigh Energies”. In: *Frontiers in Astronomy and Space Sciences* 6 (2019). ISSN: 2296-987X. DOI: `10.3389/fspas.2019.00023`. URL: `https://www.frontiersin.org/articles/10.3389/fspas.2019.00023`.

[15] T. K. Gaisser, R. Engel, and E. Resconi. *Cosmic Rays and Particle Physics.* 2016.

[16] J. Blümer, R. Engel, and J. R. Hörandel. “Cosmic rays from the knee to the highest energies”. In: *Progress in Particle and Nuclear Physics* 63.2 (Oct. 2009), pp. 293–338. ISSN: 0146-6410. DOI: `10.1016/j.ppnp.2009.05.002`. URL: `http://dx.doi.org/10.1016/j.ppnp.2009.05.002`.

[17] A. M. Hillas. “The Origin of Ultra-High-Energy Cosmic Rays”. In: *Annual Review of Astronomy and Astrophysics* 22.1 (1984), pp. 425–444. DOI: `10.1146/annurev.aa.22.090184.002233`. eprint: `https://doi.org/10.1146/annurev.aa.22.090184.002233`. URL: `https://doi.org/10.1146/annurev.aa.22.090184.002233`.

[18] W. Apel et al. “The spectrum of high-energy cosmic rays measured with KASCADE-Grande”. In: *Astroparticle Physics* 36.1 (2012), pp. 183–194. ISSN: 0927-6505. DOI: `https://doi.org/10.1016/j.astropartphys.2012.05.023`. URL: `https://www.sciencedirect.com/science/article/pii/S0927650512001284`.

[19] C. Li et al. “Measurement of muonic and electromagnetic components in cosmic ray air showers using LHAASO-KM2A prototype array”. In: *Phys. Rev. D* 98 (4 Aug. 2018), p. 042001. DOI: `10.1103/PhysRevD.98.042001`. URL: `https://link.aps.org/doi/10.1103/PhysRevD.98.042001`.

[20] R. Abbasi et al. “IceTop: The surface component of IceCube”. In: *Nuclear Instruments and Methods in Physics Research Section A: Accelerators, Spectrometers, Detectors and Associated Equipment* 700 (Feb. 2013), pp. 188–220. ISSN: 0168-9002. DOI: `10.1016/j.nima.2012.10.067`. URL: `http://dx.doi.org/10.1016/j.nima.2012.10.067`.

[21] Andeen, Karen and Plum, Matthias. “Latest Cosmic Ray Results from IceTop and IceCube”. In: *EPJ Web Conf.* 210 (2019), p. 03005. DOI: `10.1051/epjconf/201921003005`. URL: `https://doi.org/10.1051/epjconf/201921003005`.

[22] “Evidence for High-Energy Extraterrestrial Neutrinos at the IceCube Detector”. In: *Science* 342.6161 (Nov. 2013). ISSN: 1095-9203. DOI: `10.1126/science.1242856`. URL: `http://dx.doi.org/10.1126/science.1242856`.

[23] P. A. Cherenkov. *The Cherenkov Effect and Its Applications.* Pergamon Press, 1959.

[24] A. Achterberg et al. "First year performance of the Ice Cube neutrino telescope". In: ().

[25] T. Huber et al. "The IceTop Scintillator Upgrade". In: *PoS* ICRC2017 (2017), p. 401. DOI: `10.22323/1.301.0401`.

[26] M. Kauer et al. *The Scintillator Upgrade of IceTop: Performance of the prototype array.* 2019. arXiv: `1908.09860 [astro-ph.HE]`.

[27] T. Avgitas, J. C. Ianigro, and J. Marteau. *Prototype Cherenkov Detector Characterization for Muon Tomography Applications.* 2024. arXiv: `2401.16882 [physics.ins-det]`.

[28] H. K. M. Tanaka et al. "Detecting a mass change inside a volcano by cosmic-ray muon radiography (muography): First results from measurements at Asama volcano, Japan". In: *Geophysical Research Letters* 36.17 (2009). DOI: `https://doi.org/10.1029/2009GL039448`. URL: `https://agupubs.onlinelibrary.wiley.com/doi/abs/10.1029/2009GL039448`.

[29] A. D. Bross et al. *Tomographic Muon Imaging of the Great Pyramid of Giza.* 2022. arXiv: `2202.08184 [physics.ins-det]`.

[30] C. Park et al. "Design and characterization of a Muon tomography system for spent nuclear fuel monitoring". In: *Nuclear Engineering and Technology* 54.2 (2022), pp. 601–607. ISSN: 1738-5733. DOI: `https://doi.org/10.1016/j.net.2021.08.029`. URL: `https://www.sciencedirect.com/science/article/pii/S1738573321005180`.

[31] G. F. Knoll. *Radiation Detection and Measurement.* John Wiley Sons, 2010. ISBN: 978-0-470-13148-0. URL: `https://cds.cern.ch/record/1300754`.

[32] W. R. Leo. *Techniques for Nuclear and Particle Physics Experiments.* Springer-Verlag, 1994. ISBN: 978-3-540-57280-0. URL: `https://cds.cern.ch/record/302344`.

[33] P. K. F. Grieder. *Cosmic Rays at Earth.* Elsevier, 2001. ISBN: 978-0-444-50710-5. DOI: `https://doi.org/10.1016/B978-0-444-50710-5.50018-X`. URL: `https://www.sciencedirect.com/science/article/pii/B978044450710550018X`.

[34] J. Birks. *The Theory and Practice of Scintillation Counting.* Pergamon Press, 1964.

[35] R. Brunetti. "Radiation Measurements in Space Missions". In: *Nuclear Instruments and Methods in Physics Research A* 556 (2005), pp. 522–529.

[36] A. Pla-Dalmau, A. Bross, and V. Rykalin. "Extruding plastic scintillator at Fermilab". In: *2003 IEEE Nuclear Science Symposium. Conference Record (IEEE Cat. No.03CH37515).* Vol. 1. 2003, 102–104 Vol.1. DOI: `10.1109/NSSMIC.2003.1352007`.

[37] *A Technical Guide to Silicon Photomultipliers (MPPC) - Overview.* Accessed: 2024-01-14. 2020. URL: `https://hub.hamamatsu.com`.

[38] S. Gundacker and A. Heering. "The silicon photomultiplier: fundamentals and applications of a modern solid-state photon detector". In: *Phys Med Biol* 65.17 (2020), 17TR01. DOI: `10.1088/1361-6560/ab7b2d`.

[39] Hamamatsu. *MPPC arrays in a chip size package miniaturized through the adoption of TSV structure.* `https://www.hamamatsu.com/content/dam/hamamatsu-photonics/sites/documents/99_SALES_LIBRARY/ssd/s13361-3050_series_kapd1054e.pdf`. Accessed: 1-5-2024.

[40] *MPPC array S13361-3050AE-08.* Hamamatsu Photonics Website. Accessed: [Access Date]. URL: `https://www.hamamatsu.com/us/en/product/optical-sensors/mppc/mppc-array/S13361-3050AE-08.html`.

[41] Kuraray. *Plastic Scintillating Fibers.* Available at `https://www.kuraray.com/uploads/5a717515df6f5/PR0150_psf01.pdf`. Kuraray.

[42] CAEN. *DT5202.* `https://www.caen.it/wp-content/uploads/2021/05/DT5202_w1.jpg`. Accessed: 2024-01-25. 2022.

[43] CAEN SpA. *A5251 - Hamamatsu MPPC Header Adapter for A5202/DT5202.* CAEN - Tools for Discovery. Available: `https://www.caen.it/products/a5251-header-adapter/`. 2023.

[44] J. J. Vaquero and P. Kinahan. “Positron Emission Tomography: Current Challenges and Opportunities for Technology Advances in Clinical and Pre-Clinical Imaging Systems”. In: *Annual Reviews of Biomedical Engineering* 17 (Aug. 2015).

[45] CAEN. *A5202/DT5202.* Available at `https://www.caen.it/products/dt5202/`. CAEN.

[46] CAEN. *Janus.* Available at `https://www.caen.it/products/dt5202/`. CAEN.

[47] M. Börgens. *Schematic view on Shperical Coordinats.* `https://www.boergens.de/manfred/bloggeoastro/blog003_bild05_65.jpg`. Accessed: (2-27-2024).